Searches for the Electromagnetic Signatures of Merging Binary Neutron Stars and Black Holes in the Third Observing Campaign of the Dark Energy Survey Gravitational Wave Search and Discovery Program

by

Alyssa Garcia

A dissertation submitted in partial fulfillment
of the requirements for the degree of
Doctor of Philosophy
(Physics)
in The University of Michigan
2023

Doctoral Committee:

Assistant Professor Marcelle Soares-Santos, Chair
Professor August Evrard
Assistant Professor Kayhan Gultekin
Professor Dragan Huterer
Professor Keith Riles

Alyssa Garcia

argarcia@umich.edu

ORCID: 0000-0001-9578-6322

ACKNOWLEDGEMENTS

Thank you to everyone who made this possible. This was not an easy journey and I could not have made it this far without the unwavering support from everyone who has been with me throughout thes last few years.

Everyone at Brandeis, Jiayi, Prajita, Kevin, Diachi, and Luke I probably wouldn't have passed my classes without you guys, and the weekly socials and nights out were the perfect distraction from the tortures of the first two years of grad school.

To everyone back home, Vicky, Megan, and Celine, thank you for helping me through some of the hardest moments of my life. I wouldn't be here today if it weren't for all of your love and support.

To my Michigan family, Liana, David, Haley, Greg, Chelsea (Poppy, Benjen, and Sadie), Annie, Jenny, and Dane. Thank you all for integrating me into your life and letting me cry in your homes. Survivor nights, wine nights, porch bbqs, afternoons on the river, and becoming karaoke regulars, I don't have the words to express how much I value all of your friendships.

Thank you to Nora, Johnny, and Maria the OG Soares-Santos group members and to everyone at DES. Shout-out to Rob and Brodie for being my conference buddies and for helping me navigate the world of collaborations and professional meetings.

A huge thank you to Ken Herner. Your mentorship and patience with me throughout the years have been fundamental to my growth as a scientist. I don't know how I would have made it through the long nights of observations without you.

Finally, thank you to Marcelle, these years have been a wild ride and I'm grateful to have had you to show me what it looks like to be a total boss. I will remember this journey for the rest of my life.

Additionally thank you to the National Science Foundation Graduate Research Fellowship Program under Grant No. 1744555.

TABLE OF CONTENTS

ACKNOWLEDGEMENTS ii

LIST OF FIGURES vii

LIST OF TABLES ix

ABSTRACT x

CHAPTER

I. Introduction 1

1.1 The Hubble Constant and Gravitational Waves 4
1.2 The Electromagnetic Signatures of Gravitational Wave Events 7
1.3 The Dark Energy Survey and Gravitational Waves 12

II. DESGW Pipeline 15

2.1 Overview 15
2.2 Observing Strategy Optimization 17
2.3 Target of Opportunity Observations 19
2.4 Image Processing 21
2.4.1 Single-epoch processing 22
2.4.2 Image subtraction 24
2.5 Post-processing 26
2.6 Personnel Training and Night to Night Operation Procedures 29
2.7 Summary 30

III. S190510g 32

3.1 LIGO/Virgo Observations 33
3.2 DECam Observations 34
3.3 Pipeline Performance 35
3.4 Candidate identification 36
3.5 Results 37
3.5.1 Candidate Classification 37
3.5.2 Recovered Candidates 40
3.6 Discussion 42
3.6.1 Understanding Search Efficiency 42
3.6.2 Implications for Search Efficiency 43
3.6.3 Implications for Follow Up Strategy 47
3.7 Conclusion 48

IV. GW190814 50

4.1 LIGO/Virgo Observations 51
4.2 DECam Observations 53
4.2.1 Observing strategy 53
4.2.2 Image Processing 54
4.2.3 Host Galaxy Matching 54
4.3 Candidate Selection 55
4.3.1 Level 1 Selection Criteria 56
4.3.2 Level 2 Selection Criteria 58
4.3.3 Level 3 Selection Criteria 59
4.3.4 Final Candidate Assessment 60
4.4 Sensitivity Analysis 63
4.4.1 Simulating the DECam Search 65
4.4.2 Modeling Selection Criteria 68
4.4.3 Sensitivity Results 71
4.5 Discussion 78
4.5.1 Comparisons to Previous Analyses 79
4.5.2 Merger Dynamics 82
4.5.3 Implications for Follow-up Observation Strategy . . 85
4.6 Conclusion 88

V. The Observing Strategy Revisited 91

5.1 Simulation data . . . 92
5.1.1 Simulated O4 BNS events . . . 92
5.1.2 Kilonova physical models . . . 94
5.2 Kilonova lightcurve simulations . . . 95
5.2.1 DECam limiting magnitudes . . . 96
5.2.2 Cadences & observational parameters . . . 98
5.2.3 Simulation data summary . . . 99
5.2.4 Discovery probability . . . 100
5.2.5 Confirmation probability . . . 102
5.3 Optimizations and Kilonova Types . . . 102
5.3.1 Optimizations . . . 103
5.3.2 Bayesian Average Models . . . 104
5.3.3 Strategies and KN models . . . 110
5.4 Exploring the Parameter Space . . . 116
5.4.1 Exposure times . . . 117
5.4.2 Filter Choice and bright/dark nights . . . 120
5.4.3 Impact of the two-detection requirement . . . 122
5.4.4 Other Strategy options . . . 123
5.5 Real observations . . . 126
5.6 Discussion . . . 128
5.6.1 Applicability to NSBH and mass gap events . . . 132
5.6.2 Blanco/DECam and Rubin LSST . . . 134
5.7 Conclusion . . . 136

VI. Conclusion . . . 138

BIBLIOGRAPHY . . . 143

LIST OF FIGURES

Figure

1.1 Illustration of EM emission from BNS mergers. 10
1.2 GW170817 UV, optical and NIR light curves 11
2.1 Overview of search and discovery program. 16
2.2 Final observing plan for three time slots. 20
2.3 Schematic of updated single-epoch pipeline. 23
2.4 Example of the web page that is generated for a single EM candidate produced by the post processing pipeline. 28
3.1 Candidates identified by the DESGW short latency pipeline (green) and exposures used for this analysis (red). 35
3.2 Stamps (search, template, and difference images) for all S190510g candidates found by DESGW, including 11 candidates detected in our short latency search (as reported in GCN 24480) and 7 candidates which were first reported by the GROWTH collaboration. . . 41
3.3 Summary of detectable kilonovae given the observing conditions of May 11th, 2019. 45
3.4 DESGW candidates (red) as compared to where kilonovae and supernovae would be expected to live in color magnitude space given the observing conditions of our observations (i.e., 36 hours after merger, sky brightness, etc.). 46
4.1 Summary of exposures taken and candidates identified by the DESGW pipeline. 52
4.2 Images of objects passing all selection criteria before machine-learning classification. 62
4.3 Photometric classification of candidates using the `PSNID + RFC` approach. 64
4.4 KN efficiency parameterized by M_{ej}, v_{ej}, and X_{lan}. 67

4.5 Light curves (i-band) of objects passing the selection criteria. 74
4.6 Exclusion contours in the ejecta mass (M_{ej}), velocity (v_{ej}), and lanthanide fraction (X_{lan}) parameter space at the 1σ and 2σ levels. . . 83
4.7 The effect of applying selection criteria on follow-up observation sensitivity and KN efficiency. 85
5.1 The distance distribution and 90% credible interval sky localization area of the O4 simulations of BNS mergers used in this study. . . . 93
5.2 The absolute magnitudes vs days after the trigger for the weighted average of three sets of priors in the KN parameter space models considered. 106
5.3 Discovery probability vs luminosity using the *low-TT* observing strategy compared to the *Ref* strategy. 108
5.4 Left: Discovery probability vs time to completion of first pass for a single event at 160 Mpc with sky area of 168 sq-degrees. 113
5.5 Using the *low-TT*model, *Left column*: Detection probability for a given luminosity distance and sky area for *reddish & slow*, *red & faint*, *bright & blue* in (top), (middle), and (bottom), respectively. . 114
5.6 Upper left: discovery probability vs distance for *low-TT* comparing Scenario 1 and Scenario 2, as well as *Reference*, which only uses Scenario 1. 119
5.7 Discovery probability for the different strategies adopted in bright and dark time. 120
5.8 Discovery probability vs distance to event for the *low-TT* observing strategy in the first and second passes compared to the reference strategy for KN described by model with wide priors *bright & blue* (*upper left*), *reddish & slow* (*upper right*), and *red & faint*(*lower*). . 121
5.9 Distribution of confirmation day using the *reddish & slow* model. . . 124
5.10 To illustrate the flexibility of the strategy families; we present the curves constrained with 5% of *Top* strategy, e.g. *low-TT* (5%) and derived strategies. 125

LIST OF TABLES

Table

3.1 Candidates that pass the DESGW pipeline cuts as well as visual inspection from the first stage of analysis. 38
3.2 Candidate host galaxies' information. 39
4.1 Host galaxy properties of the two objects passing all selection criteria prior to final classification. 55
4.2 The selection criteria developed in this analysis and remaining objects after each criterion. 62
4.3 Constraints on counterpart ejecta properties of the candidate NSBH merger GW190814. 77
5.1 Observational conditions (photometric filter, limiting magnitude, and effective exposure time) averaged from DECam follow-ups of previous observations. 97
5.2 DECam $m_{\rm lim}(10\sigma)$, dark time 97
5.3 Observational parameter space Θ explored. 98
5.4 Kilonova Gaussian model priors. 106
5.5 Average telescope time per event in hours required for two detections, discovery and confirmation. 112
5.6 LVC GWTC events (O1-O3) containing neutron stars and with $M_2 < 5M\odot$ and SNR$>$ 8. 133

ABSTRACT

Observations of gravitational waves have inaugurated the field of multi-messenger astrophysics that promises to have a significant impact in cosmology. Identifying the electromagnetic counterparts to gravitational wave events is vital to efficiently using them as cosmological probes. The Dark Energy Survey Gravitational Wave Search and Discovery team has established a program that listens for new event alerts from the gravitational wave observatories LIGO and Virgo, creates observational plans, and quickly produces a list of candidate counterparts from optical images taken with the Dark Energy Camera. In this thesis, I describe the details of the program, present the results of two events that were followed up during the LIGO/Virgo third observing campaign which took place from April 2019 to March 2020, and describe the improved observing strategy developed for the fourth observing campaign.

CHAPTER I

Introduction

Over the last 10-15 years, growing tension between measurements of the Hubble constant, the parameter that tells us how quickly the universe is expanding, has driven many scientists to push their understanding of the cosmos beyond the ΛCDM paradigm. In ΛCDM, the accelerated expansion of the universe is assumed to be driven by the simplest form of dark energy, the cosmological constant (Λ), without any strong physical basis, and dark matter (DM) is assumed to be "cold" (CDM), interacting with regular matter only via gravity. The Hubble constant tension poses a challenge to ΛCDM and may represent the first new observable window into the physics of dark energy. For that reason, novel precision measurements of this parameter have been sought to further advance in this area (*Abdalla et al.*, 2022). On September 14, 2015, the Laser Interferometer Gravitational-wave Observatory (LIGO, *Aasi et al.* 2015) Scientific Collaboration and the Virgo (*Caron et al.*, 1999) Collaboration, jointly referred to as the LIGO/Virgo Collaboration (LVC),[1] made the

[1]In 2021, the Japanese collaboration KAGRA (*Akutsu et al.*, 2021) joined the global network of gravitational wave antennas, changing the acronym to LVK (LIGO-Virgo-KAGRA Collaboration). We will use LVC throughout this thesis as the data we use here was taken prior to 2021.

first detection of a gravitational wave source (*Abbott et al.*, 2016), the binary black hole merger GW150914[2]. This detection opened the door to a new measurement of the Hubble constant through multi-messenger cosmology.

Multi-messenger cosmology uses observations from gravitational wave (GW) sources, the latest 'messenger' to become available to the community, and their associated electromagnetic (EM) counterparts in order to make new measurements of cosmological parameters such as the Hubble constant. GW-EM multi-messenger sources offer measurements that are completely independent of the cosmic distance ladder used for example in Type Ia Supernova measurements and, with about 50 such sources, it has the potential to reach competitive (i.e. percent level) precision within the next decade (*Chen et al.*, 2018). During the first two LVC observing runs, 11 high-significance GW events were detected (*Abbott et al.*, 2019). However, only one event, the binary neutron star merger GW170817 (*Abbott et al.*, 2017a), resulted in the detection of an EM counterpart (*Soares-Santos et al.*, 2017; *Abbott et al.*, 2017b; *Coulter et al.*, 2017; *Cowperthwaite et al.*, 2017; *Evans et al.*, 2017; *Andreoni et al.*, 2017; *Hu et al.*, 2017; *Utsumi et al.*, 2017; *Valenti et al.*, 2017; *Shappee et al.*, 2017; *McCully et al.*, 2017; *Kasliwal et al.*, 2017). From this single event, a new measurement of the Hubble constant was made, resulting in $H_0 = 70.06^{+12.0}_{-8.0}$ km s^{-1} Mpc^{-1} (maximum a posteriori and 68% credible interval) (*Abbott et al.*, 2017), proving how powerful this kind of multi-messenger cosmology can be and driving new excitement for the future of multi-messenger cosmology.

[2]The convention in this field is to name the events using the GW prefix followed by the date of its observation and an alphabetic suffix if there are multiple events on the same day. The LVC initially labels its candidates with the prefix 'S' (for 'super candidate event'). They update the prefix to GW afterwards, if the candidate meets their candidate selection criteria.

In the Fall of 2017, I joined the Dark Energy Survey (DES, *Dark Energy Survey Collaboration et al.* 2016) and its GW search and discovery team (DESGW) as they were gearing up for the LVC's third observing run (O3) which took place from April 2019 to March 2020. While the first detection of an electromagnetic counterpart had already been made, there was no guarantee the next observation would be as 'easy'. In fact, despite impressive improvements to the LVC instruments, sky localizations of these events were still expected to be on the order of hundreds to thousands of square degrees, making coverage of the entire predicted sky area to sufficient depth in a single night challenging. Additionally, remaining unknowns regarding the merger rate of binary systems containing neutron stars and characteristics of the resulting light curves add an extra layer of difficulty when trying to distinguish them from other transients. Overcoming those challenges and maximizing the probability of a new discovery akin to GW170817 became the focus of my doctoral research.

In this thesis, after introducing background information relevant to this work (Sections 1.1–1.3), I detail the search and discovery program methods (Chapter II) followed by results of two searches performed in O3. Those searches include a first-of-its-kind analysis that established the framework for observational limits on kilonova light curve physical parameters (Chapter III) and an analysis that applies that framework to GW190814, the coalescence of a 23 solar mass black hole with a 2.6 solar mass compact object (Chapter IV). I then describe the improved search strategy that we developed for the fourth observing run (O4, which started in May 2023) in light of all of the lessons learned during O3 (Chapter V). Finally, I briefly summarize and discuss prospects for new multi-messenger discoveries (Chapter VI).

1.1 The Hubble Constant and Gravitational Waves

The Hubble constant, H_0, is a fundamental parameter in cosmology that quantifies the rate at which the universe is currently expanding. An H_0 measurement can be determined from a cosmological model using measurements from the early universe, or from more direct local universe probes. Determining the Hubble constant accurately is crucial for understanding the nature of dark energy and the expansion history of the universe as the value of H_0 could inform models of dark energy in such a way that could explain the universe's early expansion and potentially hint at beyond–ΛCDM physics. To study this, we begin by investigating the Hubble law, which can be simplified to $H_0 = v/d$ (ignoring peculiar velocities for the moment), where v is the recessional velocity, and d is the distance. While v can be obtained given an object's redshift, the luminosity distance often presents more of a challenge.

While thousands of estimates of H_0 have been made since 1980, one-third of those measurements have been made in the last five years (*Riess et al.*, 2022). In particular, there are two estimates of H_0 that, in recent years, have been made with precision on the order of a single percent. The first such estimate uses the Cosmic Microwave Background (CMB). In this case, we can think of an H_0 measurement being derived from calculating the sound horizon size (r_s) using the baryon and matter density. Then, to determine the angular diameter distance, $D_A = r_s/\theta_s$, one infers θ_s from the spacing between the acoustic peaks. Finally, using D_A and assuming the ΛCDM model, the H_0 measurement can be made (*Hu and Wang*, 2023). In practice, this is typically done by use of the spatial spectrum of the CMB where H_0 is then derived from a global analysis.

In 2014, the Planck Collaboration made an H_0 measurement using this method, yielding $H_0 = 67.2 \pm 1.2$ (*Planck Collaboration et al.*, 2014). Just four years later, the Planck Collaboration has improved on their precision dramatically, resulting in $H_0 = 67.4 \pm 0.5$ kms^{-1}Mpc^{-1} (*Planck Collaboration et al.*, 2020). Other experiments that utilize the CMB include the Atacama Cosmology Telescope ($H_0 = 67.6 \pm 1.1$ kms^{-1}Mpc^{-1}) (ACT, *Aiola et al.* (2020)) and the South Pole Telescope ($H_0 = 68.8 \pm 1.5$ kms^{-1}Mpc^{-1}) (SPTPol, *Dutcher et al.* (2021)); all with results consistent with Planck.

When examining the late universe, an H_0 measurement involves building a distance-redshift relation and using a local 'distance ladder' to calibrate the different types of distance indicators. In particular, stars such as Type Ia supernovae (SN) and Cepheid variables are used for this since they are considered to be 'standard candles' (Ia SNe due to their consistent peak luminosity (*Leavitt and Pickering*, 1912) and Cepheids due to their tight period-luminosity relation (*Riess et al.*, 2019; *Eddington*, 1917)). Cepheids within SN Ia hosts are the basis of the 'cosmic distance ladder', or the successive set of calibrations from various objects with known properties. The Supernova and H0 for the Equation of State of Dark Energy Collaboration (SH0ES) used these probes to achieve their first measurement of $H_0 = 74.2 \pm 3.6$ km s^{-1} Mpc^{-1} in 2009 (*Riess et al.*, 2009). Over ten years later, SH0ES has updated this measurement to $H_0 = 73.04 \pm 1.04$ km s^{-1} Mpc^{-1} (*Riess et al.*, 2022). Throughout the years it took to achieve this milestone, other methods of measuring a local universe H_0 were made with varying results. However, it is now clear that there is an inconsistency between CMB-based measurements and all other measurements that rely on

stars and galaxies. This discrepancy between early-universe and late-universe measurements may be due to a significant issue with systematics (such as uncertainties or errors in calibrations, selection effects, or host galaxy relations to name a few (*Scolnic et al.*, 2014)). It may also be the first indication that ΛCDM (which is the basis of assumption for the CMB-based measurements) is failing to provide an adequate description of our universe.

Gravitational waves provide a new local universe measurement that bypasses the systematic errors that come with the cosmic distance ladder. Gravitational waves are ripples in space-time caused by the coalescence of some of the densest objects in our universe: binary black hole (BBH), binary neutron star (BNS), and black hole neutron star (BHNS) mergers. The idea of gravitational waves was first introduced by Oliver Heaviside in 1893 (*Heaviside*, 1893), then further established by Albert Einstein in 1916 as a consequence of general relativity (*Einstein*, 1916). Einstein derived the linearized field equations for weak gravitational fields and demonstrated that they possess wave-like solutions, which we now refer to as gravitational waves. Importantly, these ripples embed vital information about the luminosity distance to its source, its orientations, its position on the sky, and information about the source's masses and spins.

To understand how distance information is embedded in gravitational wave signals, we can examine the strongest harmonic of the waveform's two polarizations:

$$h_+ = \frac{2M_z^{5/3}[\pi f(t)]^{2/3}}{D_L}[1 + (\hat{L} \cdot \hat{n})^2]\cos(\Phi(t)) \tag{1.1}$$

$$h_\times = \frac{2M_z^{5/3}[\pi f(t)]^{2/3}(\hat{L}\cdot\hat{n})}{D_L}\sin(\Phi(t)) \tag{1.2}$$

Here, M_z is the chirp mass defined as $M_z = (1+z)(m_1 m_2)^{3/5}/(m_1+m_2)^{1/5}$, $f(t)$ is the frequency given by $f(t) = (1/2\pi)d\Phi/dt$, $\Phi(t)$ is the phase, the unit vector $\hat{n}$ points from the center of the reference frame (in this case the center of the solar system's barycenter) to the location of the system on the sky while $\hat{L}$ points in the direction of the systems angular momentum (and thus provides the orientation of the system), and, finally, D_L is the luminosity distance (*Holz and Hughes* (2005)).

The ability to derive the luminosity distance from these waveforms has led them to be deemed 'standard sirens'. With the GW standard siren information in hand, the missing piece for achieving a measurement of H_0 is the redshift to the source. If EM emission can be observed associated with the siren, we can readily measure its redshift. The GW interferometers are sensitive to stellar mass binary black hole mergers, binary neutron star mergers, and black hole neutron star mergers. Of these, BNS mergers provide the most likely sources for EM emission due to the presence of matter.

1.2 The Electromagnetic Signatures of Gravitational Wave Events

The first theory proposing EM emission from a BNS merger was proposed by Eichler et al. in 1989 (*Eichler et al.*, 1989). In their paper, they explored the idea that the merger of two neutron stars could produce a significant amount of energy in the form of electromagnetic radiation. This paper suggested that during the

merger process, neutron-rich material would be ejected and undergo rapid neutron capture (r-process) nucleosynthesis, leading to the creation of heavy elements. The radioactive decay of the newly synthesized elements was then thought to produce a burst of high-energy gamma rays that could be observable from Earth. This was

Eichler et al.'s theory provided an initial framework for understanding the potential electromagnetic emission associated with binary neutron star mergers. In particular *Schutz* (1986) was the first to propose using these sources with gravitational waves in order to measure the Hubble constant. Building on this, many have put forward various models for emissions including in the form of gamma-ray bursts (GRBs) and radio/optical afterglow (*Metzger and Berger*, 2012), and more prominently, an isotropic emission powered by the radioactive decay of rapid neutron capture (r-process) elements in the merger ejecta known as a kilonova (KN) (*Tanaka and Hotokezaka*, 2013; *Barnes and Kasen*, 2013). Additionally, many teams have studied neutron star mergers that result in electromagnetic counterparts over the decades, e.g. *Li and Paczyński* (1998); *Piran* (2004); *Metzger et al.* (2010). While initially proposed as EM models for BNS mergers, KN from NSBH mergers are also possible, as long as some of the neutron star material gets ejected from the merging system, which was first predicted by *Lattimer and Schramm* (1974). As no counterpart has been detected from such a system, the likelihood of these events is largely unknown.

DESGW assumes a KN source model for mergers involving at least one neutron star (BNS and NSBH). As neutron stars approach the merging point, tidal tails grow into the equipotential surface and then mostly flow back into the main remnant.

Some few percent of matter in the tails are dynamically ejected at speeds ≈ 0.1c. The ejected material undergoes r-process nucleosynthesis as the few nuclei in the sea of neutrons grow by neutron absorption. In previous LVC runs, the details of our model followed the simulation-based analysis of *Grossman et al.* (2014). Observationally, we modeled the merger event luminosity, L, and temperature, T, and assumed the event is an optically thick blackbody of which we observe a photosphere. All the thermal energy comes from the r-process beta-decay episode and we define an energy deposition rate per unit mass, ϵ, so that $L \approx m\epsilon$. At early times ($t < t_{peak}$) L scales as $L \propto t^2$ and at late times ($t > t_{peak}$) as $L \propto t^{-1/3}$. The time to peak brightness t_p is $\sim m^{-1/2}$. We assume that the photosphere is a blackbody with $T = \left(\frac{L}{\sigma\left(2\sqrt{\pi}vt\right)^2}\right)^{0.25}$, where vt comes from the radius of the photosphere. The flux through any filter is then:

$$f = 4.4 \times 10^{22} \int B_\lambda \mathrm{d}\lambda \; L_{40} T_{1000}^{-4} d_{100}^{-2}$$

where B_λ is the Plank distribution, L_{40} is the luminosity in units of 10^{40} ergs/sec, T_{1000} is the temperature in units of 1000 K, and d_{100} is the distance in units of 100 Mpc.

We can break up the model into sub-components, each of which has a different opacity: iron (blue), with ($\kappa \approx 0.1$), and lanthanide[3] (red), with ($\kappa \approx 10$), motivated by the two types of emission. We use the same energetics as described above; one swaps out the B_λ for a computed SED as one computes the flux through a filter. There is a range of uncertainties in the peak absolute magnitudes. For a given time

[3]Lanthanides describe the group of elements with atomic numbers 58-71 and are metals who's 4f sublevels are filled.

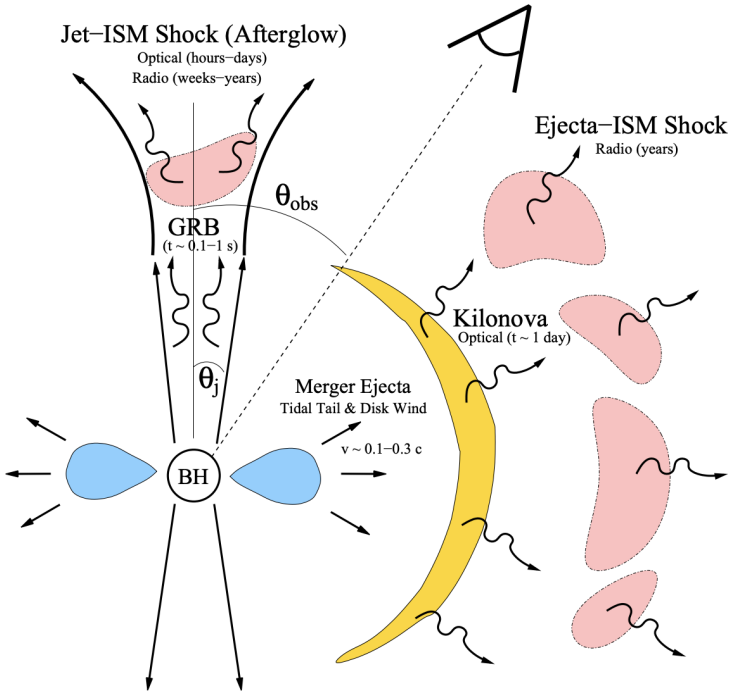

Figure 1.1 Illustration of EM emission from BNS mergers (*Metzger and Berger*, 2012).

we calculate the model's absolute magnitude, M which has a model uncertainty dispersion of σ_M.

We can infer that the dual blue and red components of the light curve combined with the timescales at which the red and blue components rose/fell, indicate the presence of two separate emitting regions, with two distinct sources of ejecta, as suggested by *Kasen et al.* (2015), among others. Figure 1.1 shows a cartoon of a potential model for emission.

DESGW has used the *Kasen et al.* (2017) model for our searches. In this model, the key parameters of the models are the ejected mass, ejecta velocity, and composition of the ejected matter or lanthanide fraction. This model uses two distinct

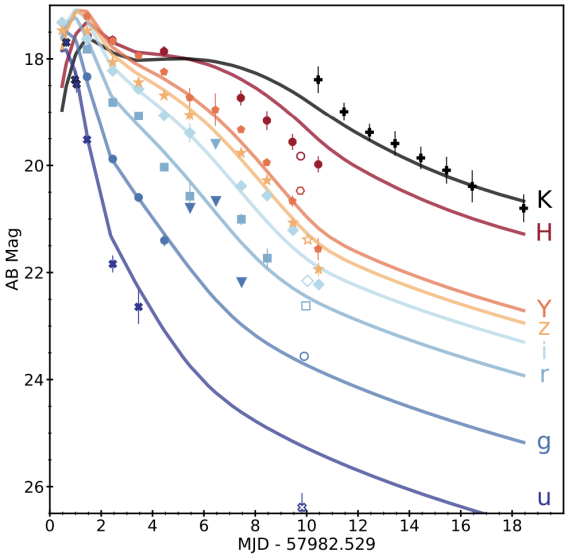

Figure 1.2 GW170817 UV, optical and NIR light curves (*Cowperthwaite et al.*, 2017).

mechanisms for mass ejection. The first being the mass ejected at the time of merger, during which tidal forces disrupt the matter from the surface of the stars and are propelled into the polar regions by shock heating. The second mechanism involves the matter remaining just after merger in an accretion disk to be blown away in winds. The results of this method produce a KN light curve that can be broken down into 'blue' and 'red' components. These components of the ejecta represent the light and heavy r-process, respectively. Figure 1.2 shows that, for the first ever confirmed EM counterpart to a GW event, GW170817, the observed light curve was initially dominated by the blue component (for the first ~ 5 days) and then switched to red component dominant. Note that we do not assume that the new KN will have the same light curves as GW170817. We allow the three key parameters, namely ejected mass, velocity, and lanthanide fraction to vary and use the corresponding

light curve predictions of the Kasen et al. model.

1.3 The Dark Energy Survey and Gravitational Waves

The Dark Energy Survey (DES) (*The Dark Energy Survey Collaboration*, 2005) is a cosmological survey aimed at understanding the nature of dark energy, the unknown force that is thought to be responsible for the accelerated expansion of the universe. The instrumental and observational strategy for achieving this is by using complementary methods such as probing the growth of large-scale structures in the universe and exploring various astrophysical phenomena such as supernovae, galaxy clusters, and weak gravitational lensing (*Abbott et al.*, 2018). DES uses data from a 570-megapixel camera, the Dark Energy Camera (DECam, *Flaugher et al.*, 2015), which has a 3 $\deg^2$ field-of-view, where each image is called a 'hex' (due to DECam's roughly hexagonal focal plane), and is mounted on the Blanco 4-meter telescope located at the Cerro Telolo Inter-American Observatory in Chile. It observed a wide-field survey covering ~ 5000 $\deg^2$ of the southern sky in *grizY* bands, known as the DES footprint, as well as $27\deg^2$ deep supernova survey in *griz* bands. Observations for the DES nominal survey began in 2013 and finished in 2019. However, the DESGW project continues to use DECam to this day. DESGW has been granted DECam time via telescope proposals to the National Optical-Infrared Astronomy Research Laboratory (NoirLab).

The results from the DES survey highlight new constraints on cosmological parameters that DES is particularly sensitive to, like the matter density of the universe, Ω_m, and amplitude of density fluctuations, S_8. These results show a preference for

lower S_8 as compared to early-Universe CMB measurements of the same parameters (*Abbott et al.*, 2018, 2021). This discrepancy may be another hint, separate but complementary to the H_0 tension, of new physics beyond the ΛCDM model (*Abbott et al.*, 2022).

While the survey has since completed, DECam remains one of the most powerful instruments in the southern hemisphere for wide area optical imaging. To this day DECam is used by scientists both from DES and otherwise, to make groundbreaking observations. In addition to DESGW, DES members still take advantage of DECam's capabilities to image supernovae and characterize their light curves. Supernova cosmology is a cornerstone of DES cosmology results and as such, the team has a robust image processing pipeline. This pipeline was reworked in 2014 when DES launched the DESGW project. During the LVC's third observing run, this team was primarily comprised of roughly 10 members of DES.

DESGW uses DECam to perform the most comprehensive searches for electromagnetic counterparts to gravitational wave events aiming to use them as standard sirens for cosmology. In the emerging field of multi-messenger cosmology, current H_0 measurements lack the precision to be considered relevant for the early/late-universe tension. However, this early work is seminal to enabling those precision measurements in the near future.

The mode of operations for following up a GW event differs from that of a typical survey. Currently, there is no way to know when a gravitational wave event will occur, and as such telescope time for these events are achieved using Target of Opportunity (ToO) telescope time. These are open calls for proposals and thus a

very competitive process. DESGW, as well as other teams, such as the Global Relay of Observatories Watching Transients Happen (GROWTH; *Goldstein et al.* 2019; *Andreoni et al.* 2019b) collaboration have been granted time on DECam to follow up GW events. Data from all competing groups are shared with zero proprietary time with the community. This ensures the timeliness of results and maximizes the impact of the program overall.

With limited telescope time that interrupts other scientists' projects, choosing which events to observe and determining the most efficient image sequence are crucial and challenging tasks. That challenge is compounded by the fact that, just as the astronomical community was learning how to best observe these events, the LVC has also been improving their short-latency event alerts. For example, candidate events often have their classification and sky localization dramatically changed within hours of their first notification. The DESGW program must be nimble and flexible to adequately handle this changing landscape on an event by event basis.

CHAPTER II

DESGW Pipeline[1]

2.1 Overview

Figure 2.1 provides an overview of the DESGW program. The reception of a GCN[2] notice from LVC is the starting point of a multi-step DESGW process. First, we calculate the possible coverage of the event with DECam for the night and discuss whether to proceed with observations. If the decision is to observe, we then move to the observation and data preparation phase. The observing team is briefed and provided with the observing plan. Based on our observing plan, we also make an initial determination of possible templates (images that will serve as reference later in the difference imaging processing step) and pre-process them before the beginning of the night, if there is time. The next phase is data reduction. DESGW aims to process and analyze a given night's observations within 24 hours or less so that we

[1]This chapter is adapted from *Herner et al.* (2020a) which details the pipeline from runs O1 and O2, and *Herner et al.* (2020b) which details updates made for O3.

[2]The Gamma-ray Coordinates Network (GCN) notices are the channel used by the community to send and receive notices of transients.

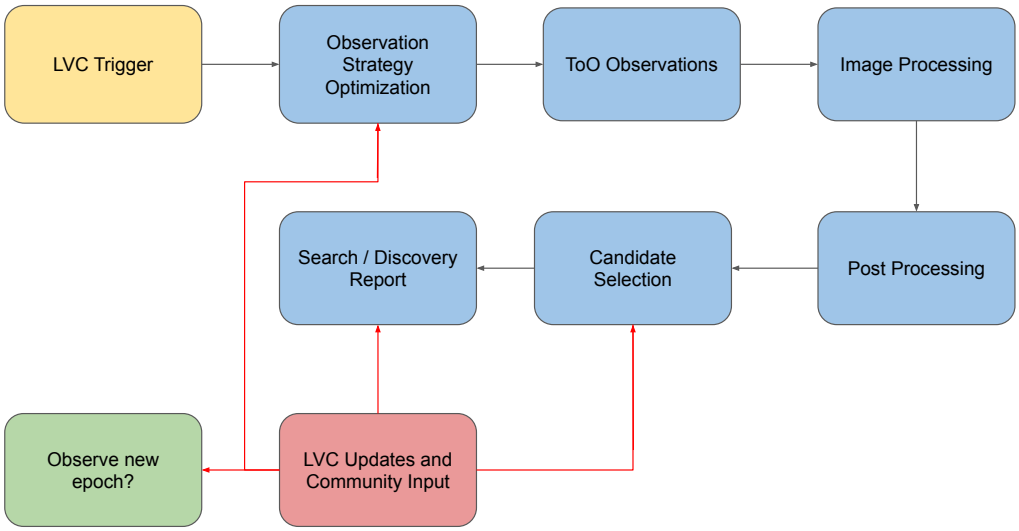

Figure 2.1 Overview of the DESGW search and discovery program.

can report electromagnetic counterpart candidates to other telescopes for follow-up (spectroscopic classification and multi-band photometry for light curve construction). We rapidly provision the required computing resources using a mixture of resources at Fermilab and other campus and laboratory sites via the Open Science Grid (OSG; *Pordes et al.* 2007), relying on its high throughput. As new search images arrive at Fermilab from CTIO, image processing jobs are sent to all available resources. The results are copied to a local disk at Fermilab and summary data recorded in a database for post-processing and candidate selection. Once candidates are selected, a GCN notice with time of observation, coordinates, filters, magnitude limit, and potential host galaxy information (if available), is sent out. Community input is vital for efficient observations. Considering where other teams have searched

and ruled out often plays a pivotal role in determining the observing strategy for any following nights.

2.2 Observing Strategy Optimization

Our system listens to the LIGO/Virgo alert stream through a Python code that uses the GCN VOEvent client to receive and parse the VOEvent, a specific XML format for describing astronomical transients. The alerts then come through via text, email, or Slack message displaying basic information about the sky location, localization area, false alarm rate (FAR), and event type. Using this information, preparations for initial observation maps are started. The observing scripts are generated by calculating event counterpart visibility probability maps summed inside an all-sky DECam hex layout and choosing the highest-probability hexes for the highest priority observations.

We wish to calculate maps of

$$p(\alpha, \delta) = \int p(x|\alpha, \delta) p(y|\alpha, \delta) p(d|m, t, \alpha, \delta) dm \,. \tag{2.1}$$

where

– $p(x|\alpha, \delta)$ is the LVC spatial localization map probability per pixel (x). LVC triggers include localization maps (*Singer et al.*, 2016c) in HEALPix format (*Górski et al.*, 2005). The first of these maps provides the spatial localization probability per pixel, the second provides distance, the third provides a Gaussian variance estimate on the distance, and the fourth contains a normalization

plane. We take the first map to be $p(x|\alpha, \delta)$. Maps derived from this one have the same resolution as we choose to read this map.

– $p(y|\alpha, \delta)$ is our ability to recognize the detection given source crowding and is related to a false positive rate. Our model is that the recognition probability is taken to be $p(y|\alpha, \delta) = 0.0$ at or above 610 stars/deg^2 (roughly that of the Galactic anticenter) and $p(y|\alpha, \delta) = 1.0$ at or below 10 stars/deg^2 (roughly that of the south Galactic pole), linear in density between.

– $p(d|m, t, \alpha, \delta)$ is the DECam detection probability of a source of magnitude m at time t per pixel. This uses the limiting magnitude map, the source model and the LVC event distance map.

– the time dependence of m enters via the source model.

As described in Section 1.2, our model uses three physical parameters, the ejecta mass, ejecta velocity, and lanthanide fraction, in combination with the two components for distinct emissions. While the kilonova produced by GW170817 was informative, a single light curve alone is not enough to definitively describe what a typical emission would look like. To this end, during O3, we included information from a machine-learning based photometric classification algorithm called `KN-Classify`. `KN-Classify` uses an "individualized training set approach", in which the training set is simulated immediately following observations and incorporates the exact seeing, sky-brightness, exposure times, optical filters, and time-spacing of exposures into the simulated photometric data used for training. Using models from the Photometric LSST Astronomical Time-Series Classification Challenge (PLAsTiCC) *The*

PLAsTiCC team et al. (2018), `KN-Classify` simulates time-series photometric observations of a variety of astrophysical sources as they would appear in DECam data using the Supernova Analysis software package, `SNANA` (*Kessler et al.*, 2009, 2019a). The addition of a robust classifier informs the DESGW team about how various observing conditions may affect observational plans. This classifier provided the building blocks for the updated observing strategy software tool to calculate the likelihood of being able to see a KN in DECam images given a particular LVC candidate, as detailed in Chapter V.

2.3 Target of Opportunity Observations

Once we have calculated maps of $p(\alpha, \delta)$ we can construct the observing plan. Each observation during O3 is of a hex (so named because the DECam focal plane is roughly hexagonal). An observation may be a single 90s i-band exposure, as in BBH sources, or a triplet of 90s each in an i, z, z band sequence, as in events containing NS. The aim is different in each case. We expand on this idea moving forward into O4, allowing for variable exposure times depending on the sky localization probability. This is described in more detail in Chapter V.

To construct the plan we create slots of time that contain integer numbers of hexes with a total duration of around a half hour; each slot has the full map-making performed. For NS events there are six hexes per slot (three roughly 90s observations per hex), while for BH and bursts, there are 18 hexes per slot (one 90s observation per hex). The detection probability maps are then "hexelated": the probabilities are summed inside a fixed pattern of camera pointings. For the night, the hex with the

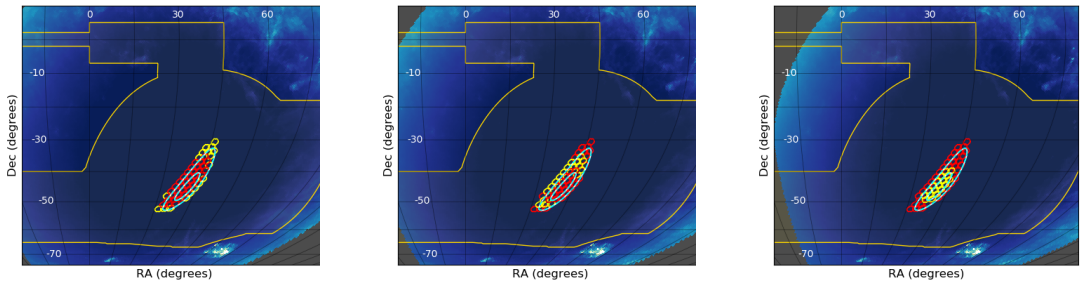

Figure 2.2 Final observing plan for three time slots. The red hexagons are all scheduled observations across all slots, while the yellow hexagons are those performed within the given time slot. The solid white lines are the 50% and 90% LVC probability contours, and the yellow line represents the nominal DES footprint. The example shown here is for GW170814, a binary black hole merger.

greatest probability is found and assigned to be observed in a time slot. The time slot is chosen to maximize the observability of the hex in question (and probability of actual detection of the transient if it happens to be located in those exposures). That hex is then removed from consideration (removing all probabilities for that hex at different time slots in the night), and we repeat the procedure with the next-highest probability hex until all slots are full. We use a mean overhead time of 30s between hexes to account for the time it takes to move the telescope from one position to another. Now we have a time series that makes full use of observing probabilities, aiming to ensure we observe as many high-probability hexes as possible on a given night, and following an optimal sequence, as shown in Figure 2.2. We convert this list to a JSON file with the appropriate content to drive DECam and the Blanco telescope. The same JSON files, modified for a later time, are used during the subsequent observing nights.

This method for creating an observing plan was successfully used for the first three LVC observing runs, resulting in one confirmed counterpart. With the improvements

to the LIGO and Virgo instruments, as well as the expected addition of the Japanese instrument, KAGRA (*Akutsu et al.*, 2021) later in the season, the expected sky localization areas during O4 to be much smaller, e.g. on the order of 100 square degrees or less. This improvement allows for updating the observational planning method, such that, instead of prioritizing when an area of the sky will be visible, e.g. breaking the sky map into time slots, we can first prioritize the area of the sky that is most likely to contain the source. Then using a nearest neighbor approach, we can observe the remainder of the area. While this method is readily available, due to problems during the improvements, Virgo has been unable to join at the beginning of O4. The lack of a third detector resulted in O4 sky localization areas similar to what was observed during O1 and O2 so far.

2.4 Image Processing

We build on the existing DES image processing pipelines. For image preparation, we use the DES single-epoch (SE) processing pipeline (*Morganson et al.*, 2018). We use a modified version of the DES supernova processing pipeline (`DiffImg`), described in *Kessler et al.* (2015), to perform image differencing. This pipeline has a strong track record of discovering rare classes of transient and rapidly fading objects such as in *Pan et al.* (2017) and *Pursiainen et al.* (2018). We give a description of both pipelines here, focusing on the modifications made specifically for DESGW and updates done for the third and fourth observing runs.

2.4.1 Single-epoch processing

The first stage of image processing each night is the SE pipeline, which consists of an image correction stage and an object cataloging stage known as FirstCut which includes astrometric calibrations.

SE begins with a stage to make the raw images science-ready. This stage includes crosstalk corrections, pixel corrections, and bad pixel masking (*Bernstein et al.*, 2018). The pixel corrections include bias subtraction, pixel non-linearity correction, a conversion from DN (digital number) to electrons, a "brighter-fatter" correction, and finally flat fielding. This stage creates a catalog of the brighter objects in each image with `SExtractor` (*Bertin*, 2011), to be used in the astrometric calibration.

The astrometry stage uses `SCAMP` (*Bertin*, 2006) with the aforementioned catalog of bright objects, generated by `SExtractor` during image correction, to calculate an astrometric solution using an initial guess of third-order polynomial World Coordinate System (WCS; *Greisen and Calabretta* 2002) distortion terms for each of the 62 CCDs in the DECam array to produce a solution to place CCD pixel positions into a TPV (tangent plan projection) WCS. For the O3 run, the point source catalog was updated from 2MASS (*Skrutskie et al.*, 2006) to the GAIA-DR2 catalog (*Gaia Collaboration et al.* (2018), *Lindegren et al.* (2018)) to solve for the focal plan solution. This allows for both reduction of DES astrometric uncertainties to below $0.03''$ per coordinate (dominated by DES uncertainties) and for us to calculate an astrometric solution CCD by CCD rather than over the whole image. Demonstrated in Figure 2.3, a major improvement to the speed of this step involved running the formerly sequential steps, i.e. waiting for the entire image to finish one step before moving on

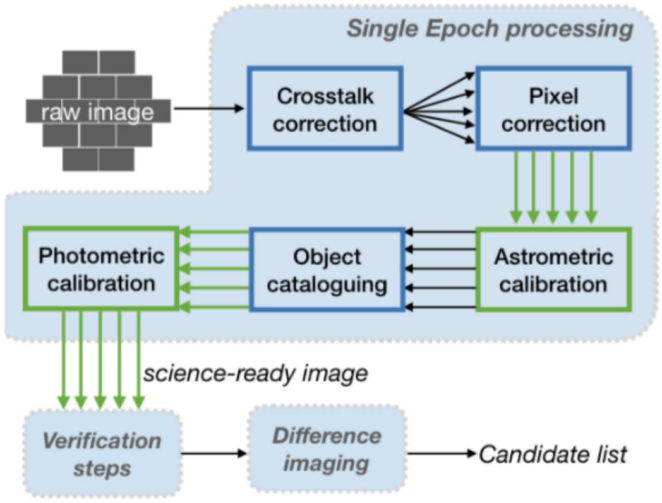

Figure 2.3 Schematic view of the updated single-epoch pipeline. The green arrows indicate steps that were previously performed on the full image before moving to the next step and have since been updated to be run in parallel per CCD. Figure published in *Herner et al.* (2020b)

to the next, is now a per-CCD calculation that can run in parallel.

The FirstCut processing calculates an astrometric solution with `SCAMP`, performs bleed trail masking, fits and subtracts the sky background, divides out the star flat, masks cosmic rays and satellite trails, measures and models the point spread function (PSF), performs object detection and measurement using `SExtractor`, and performs image quality measurements.

To catalog all objects from single-epoch images we run `SExtractor` using PSF modeling and model-fitting photometry. A PSF model is derived for each CCD image using the `PSFEx` package (*Bertin*, 2011). We model PSF variations within each CCD as a N^{th} degree polynomial expansion in CCD coordinates. For our application, we adopt a 26×26 pixel kernel and follow variations to 3^{rd} order.

In `SExtractor` (version 2.14.2) we use this PSF model to carry out PSF corrected model fitting photometry over each image. The code proceeds by fitting a PSF model and a galaxy model to every source in the image. The two-dimensional modeling uses a weighted χ^2 that captures the goodness of fit between the observed flux distribution and the model and iterates to minimize the χ^2. The resulting model parameters are stored and "asymptotic" magnitude estimates are extracted by integrating the model flux.

The advantages of model fitting photometry on single-epoch images that have not been remapped are manifold. First, pixel to pixel noise correlations are not present in the data and do not have to be corrected for estimating measurement uncertainties. Second, unbiased PSF and galaxy model fitting photometry is available across the image, allowing one to make a more precise correction to aperture magnitudes than those often used to extract galaxy and stellar photometry.

2.4.2 Image subtraction

To identify GW EM counterpart candidates within search images we use the aforementioned `DiffImg` software, originally developed for supernova searches in DES. Using a feature of `SCAMP`, we calculate a joint astrometric solution on both the search and template image(s) using the GAIA-DR2 catalog. We perform the image subtraction via the `HOTPANTS` package (*Becker*, 2015). In our case, we perform a separate subtraction between the search image and each template, and then combine the difference images, rather than do a single subtraction on one combined template. While this approach is clearly slower than doing a single subtraction, it

avoids potentially large PSF variations that could arise when combining templates taken in potentially very different observing conditions.

The `DiffImg` software, also sometimes known as the `DiffImg` "pipeline", can accept as templates images that only partially overlap with search images, images that may have a relative rotation with respect to the search images and images from DECam that were not taken on DES time (we only use such images if they have been publicly released). These are our main modifications of the pipeline relative to the DES supernova use case, where the search and template images are always exactly aligned (within telescope pointing errors) with one of a small set of fixed pointings that comprise the supernova survey area. After obtaining template images we apply the SE process to them as described in 2.4.1, so they are ready in the case of an LVC event trigger. If the counterpart lies outside the DES footprint and no overlapping template image exists, template images of the appropriate area of the sky must be taken at a later time, after we expect any counterpart to have faded.

`DiffImg` identifies candidate objects by running `SExtractor` on the difference images. Objects detected are filtered through a set of selection criteria listed in Table 1 of *Herner et al.* (2020a). Since the combined difference image includes correlated search image pixels summed over each template, the standard `SExtractor` flux uncertainties are not valid. We developed a special algorithm to properly account for correlations when determining the flux uncertainties. Surviving objects are referred to as "detections". These detections then filter through a machine learning code, `autoScan` (*Goldstein et al.*, 2015), which takes as input the template, search, and difference images and considers such items as the ratio of PSF flux to aperture flux

on the template image and the magnitude difference between the detection and the nearest catalog source. `autoScan` returns a number between 0, an obvious artifact, and 1, a high-quality detection.

2.5 Post-processing

The outputs of `DiffImg` are the inputs to our post-processing pipeline, which matches detections of the same objects across different exposures and applies quality assurance requirements. It also analyzes fakes injected into the images to assess the performance of `DiffImg`. This is in preparation for the final sample selection step.

Post-processing takes as input the collection of "raw" candidates from `DiffImg`, defined as when two or more detections have measured positions matching to within 1 arcsec. The two detections can be in the same band or different bands, or on the same night or different nights. All raw candidates are saved, which includes moving objects such as asteroids. Requiring detections on separate nights, or with a minimum time separation on the same night, helps to reject moving objects.

At this point, we also apply a minimum machine learning score requirement, typically 0.7, based on the `autoScan` score obtained during `DiffImg`. The threshold of 0.7 was chosen based on by eye examination of images to ensure we initially focus on images that are of good quality. It is a choice to apply the `autoScan` requirement in post-processing rather than earlier in the process as it facilitates other detection completeness studies with looser requirements.

"Science candidates" are those raw candidates that pass the machine learning score requirement. For each science candidate, we perform forced PSF photometry at

the positions of the science candidates in all difference images that cover the location. Forced photometry provides flux measurements in all observations, regardless of the S/N.

At this stage, the science candidates still contain backgrounds, the leading examples of which are supernovae, asteroids, and M dwarf flare stars. To mitigate spurious detections we take advantage of third party resources such as the Transient Name Server (TNS), which is used to identify any known transients such as supernovae and variable stars. To eliminate objects such as asteroids, we require that any candidate must have two detections that are separated by at least 30 minutes. We additionally record any new objects found in our images to these public catalogs as well as publish findings via GCN.

Additionally, all science candidates undergo a host matching process that identifies nearby galaxies and ranks them by probability of being the candidate's host galaxy. This matching uses a galaxy catalog consisting of data from the SDSS DR13 (*Albareti et al.*, 2017), DES Y3Q2 (*Abbott et al.*, 2018), and 2MASS photoz (*Bilicki et al.*, 2014) catalogs.

As one of the updates for the O3 run, we created a web page to not only monitor the status of the image processing but displays the relevant candidate information. During each epoch of observation, as the candidate information is completed, it is then compiled into a table such as the one in Figure 2.4. Here, the location, timestamp, magnitude, machine learning score, host galaxy information, as well as some processing-specific flags are displayed. Additionally, we begin the creation of a light curve and compile the stamps (the images of the source on the night of the

observation, the template image from before the event, and the difference between the two images) associated with each observation. An example of the web page is shown in Fig 2.4.

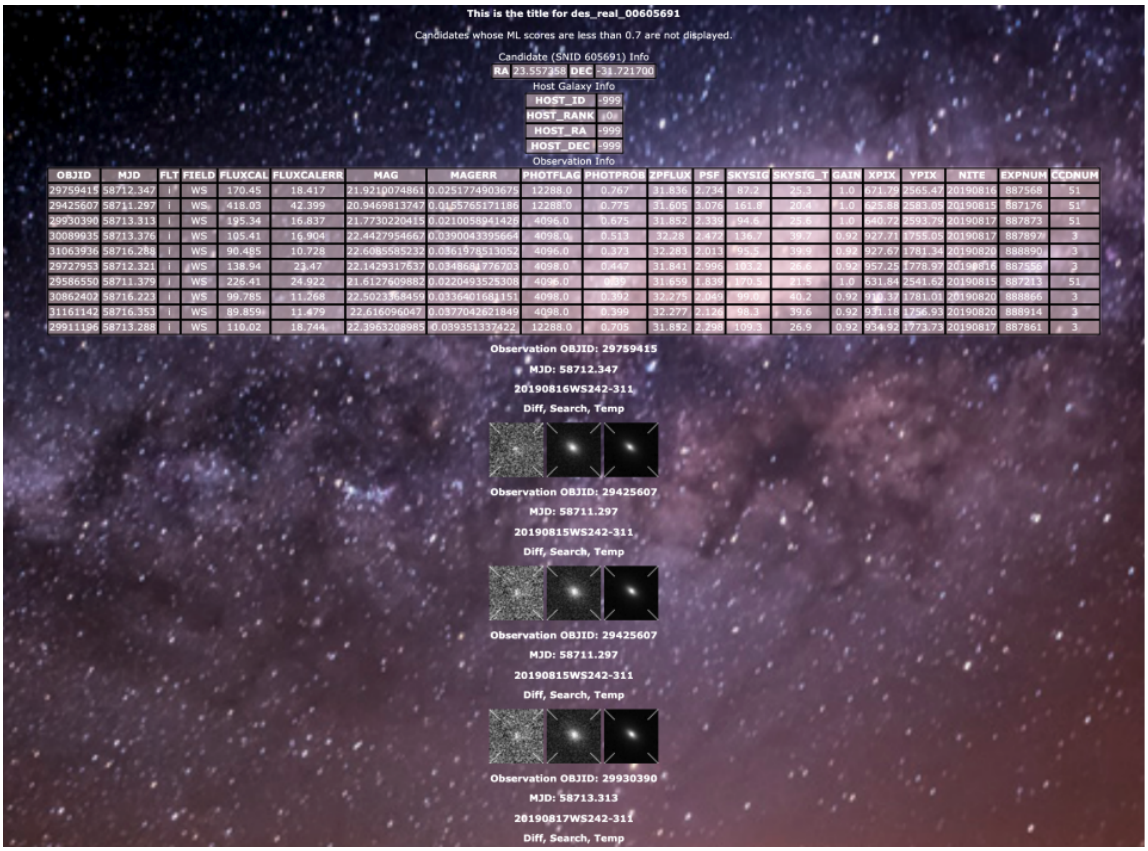

Figure 2.4 Example of the web page that is generated for a single EM candidate produced by the post processing pipeline. The page provides information on the potential host galaxy information if available, the time, sky location, magnitude, and observing condition information for each observation of the candidate.

Every piece of information displayed on the candidate web page was necessary for the final step of the search and discovery pipeline. This step of this process involves hands on expertise from DES scientists. Due to the new and evolving nature of the

field, we felt that having a final look over each candidate that pass preliminary cuts was a crucial step to both understanding what these objects may look like and to mitigate publishing candidates that would be wasteful for other teams to follow up. During O3, this page was crucial for both creating the final candidate list, as well as bettering our understanding of what cuts can be standardized and automated in the future.

2.6 Personnel Training and Night to Night Operation Procedures

As the number of triggers increased from O2 to O3, increasing the workforce of the search and discover team became vital. The creation of the on-call detail became an important aspect of the search and discovery program. To act as an on-call member included signing up for an 8 hour time slot, in which the member is responsible for having some means of receiving an LVC alert and determining if the event is worth triggering. As an international collaboration, DES members from around the world volunteered during times that were most convenient in their timezone. Each on-call member additionally needed training on the basic functions of each step of the image processing pipeline. To this end, we created both written and video training sessions that are currently available within DES's internal documentation.

Determining which events were worth following up was and remains unique to each event. The information available from the LVC is limited to a sky localization, distance distribution, classification likelihood, and false alarm rate. Due to the novelty of these events, and evolving nature of the LVC information output (on the

scale of hours to days), creating hard limits on which events to move forward with is not an option. For example, the candidate event S190510g was initially classified by the DESGW team as potentially viable. The 98% probability of originating from a BNS system and 2% probability of being non-astrophysical (e.g. signal created from ground noise) in nature as well as the small sky area (31deg^2 for the 50% confidence region) was compelling. The DESGW team took pause with the false alarm rate of 1 per 37 years and ultimately let the GROWTH collaboration take the call for triggering follow up. Roughly a day after the initial trigger, the LVC updated the event parameters to downgrade the event to 58% probability of being non-astrophysical in nature.

The nature of this follow up program involves interrupting another scientist's work to proceed with imaging. As such, teams are awarded a limited number of hours to interrupt per season. Proving the responsibility of the team to not interrupt for events with a low likelihood of detection plays a vital role in determining how much risk to take. In particular, as the LVC season proceeds, the amount of observing time allotted becomes increasingly precious. For this reason, the on-call schedule of DESGW scientists who are trusted to make the call to follow up will remain in place for O4.

2.7 Summary

The results from O1, O2, and O3 demonstrate that our infrastructure can quickly get on sky following a ToO trigger, rapidly process new images, and carry out image differencing analysis in a timely manner. The infrastructure is not limited to

GW event follow-up, however. It is straightforward to apply the same techniques to a wide variety of astrophysical transient searches, including searches for Trans-Neptunian Objects, the hypothetical Planet Nine and has been successfully used for searches of optical signatures from high-energy neutrino events detected by the IceCube experiment (*Morgan et al.*, 2019).

The DESGW program has completed a series of improvements to the computing infrastructure for follow up observation preparation and to the imaging pipeline itself between each of the LVC observing seasons. O3 ran from April 2019 to March 2020 and saw follow up of an additional 4 GW candidate events. Of those 4 events, two originated from BBH mergers, and the other two are described in this thesis. The infrastructure also performs well in a variety of time-domain astronomy programs. DESGW has excellent potential for discovering additional EM counterparts to future GW events and is eagerly awaiting additional LIGO-Virgo-KAGRA triggers during the fourth observing season.

CHAPTER III

S190510g[1]

In this Chapter, we present our search for the electromagnetic counterpart of the LIGO/Virgo event S190510g, a binary neutron star merger candidate of moderate significance. While this event was later classified as likely non-astrophysical in nature, our short latency search and discovery pipeline identified 11 counterpart candidates, all of which appear consistent with supernovae following offline analysis and spectroscopy by other instruments. Later reprocessing of the images enabled the recovery of six more candidates. Additionally, we implement our candidate selection procedure on simulated kilonovae and supernovae under DECam observing conditions (e.g., seeing and exposure time) with the intent of quantifying our search efficiency and making informed decisions on observing strategy for future similar events. This search was the first to employ a comprehensive simulation-based efficiency study. We find that using our follow-up strategy, there would need to be 19 events similar to S190510g for us to have a 99% chance of detecting an optical counterpart, assuming a GW170817-like kilonova. We further conclude that optimization

[1]This chapter is published as *Garcia et al.* (2020)

of observing plans, which should include preference for deeper images over multiple color information, could result in up to a factor of 1.5 reduction in the total number of follow-ups needed for a discovery.

3.1 LIGO/Virgo Observations

All three LVC detectors (LIGO Livingston, LIGO Hanford, and Virgo) recorded the event, S190510g, with a 98% initial probability of being a binary neutron star (BNS) event, a 2% probability of having a non-astrophysical origin, and a false alarm rate of 1 per 37 years. The 50% (90%) confidence regions spanned 575 $\deg^2$ (3462 $\deg^2$) in the initial LVC bayestar localization map. At 10:08:19 UTC on May 10, the LVC released an updated map from the `LaLInference` pipeline (*Veitch et al.*, 2015), decreasing the 50% and 90% confidence regions to 31 $\deg^2$ and 1166 $\deg^2$ respectively, and refined the distance estimate to 227$\pm$92 Mpc, or $z = 0.05\pm0.02$ (using flat ΛCDM cosmology with $H_0 = 70$ km/s/Mpc and $\Omega_m = 0.3$) (*LIGO Scientific Collaboration and VIRGO Collaboration*, 2019b). On May 10, 20:43:51 UTC the classification of the nature of the event was updated to 85% BNS and 15% non-astrophysical. Finally at 20:18:44 UTC on May 11, the LVC updated this probability to being non-astrophysical origin at 58% and of a BNS to 42% as well as updating the false alarm rate to 1 in 3.6 years.

3.2 DECam Observations

DECam was used for two nights to conduct target-of-opportunity imaging of the LIGO/Virgo GW compact binary merger candidate S190510g (*LIGO Scientific Collaboration and VIRGO Collaboration*, 2019a). Since the initial classification of S190510g was a BNS merger with high probability, the GROWTH (Global Relay of Observatories Watching Transients Happen *Goldstein et al.* 2019; *Andreoni et al.* 2019b) collaboration chose to trigger DECam (NOAO proposal 2019A-0205). All exposures from this proposal were immediately made public (*Andreoni et al.*, 2019a). GROWTH initiated EM follow up on May 10th at 06:00:25.488 UTC. The observing plan on this evening was based on the original LVC bayestar probability map. The updated LVC `LALInference` map disfavored most of the region observed on the first night. As a result GROWTH prepared a new observing plan for the second night (*Andreoni et al.*, 2019a). This plan consisted of observing for ∼1.5 hrs beginning at 22:51:57 UTC on May 10. 80 exposures total were taken in the g, r, and z bands for 40 seconds each. Each filter visited roughly same area of the sky, approximately 30 minutes apart, in order to eliminate moving objects. The 10σ depths for each band are $m_z = 20.58$ mag, $m_r = 21.72$ mag, and $m_g = 21.67$ mag, where the average seeing was 1.33 arcsec, the average airmass was 1.71, and the average attenuation due to cloud was 4%. These observations covered $\sim 65\%$ of the probability region, as shown in Figure 3.1. Plans to follow up this event for a third night were retracted due to the updated classification probability of this event. Our analysis uses only the exposures from the second night of observations as to include only the high probability region from the `LALInference` LVC map.

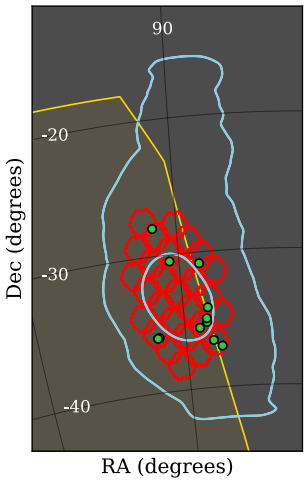

Figure 3.1 Candidates identified by the DESGW short latency pipeline (green) and exposures used for this analysis (red). Blue contours show 90% and 50% localization probability in one of the three regions identified by the LVC. The DES footprint is shown in yellow. Our exposures (red) cover ∼84 deg^2 total and contain ∼65% of the total probability.

3.3 Pipeline Performance

Using the search and discovery pipeline described in Chapter II, roughly 26% of the image processing jobs took between $0 - 30^{\rm min}$ to complete, 23% took $0.5 - 1^{\rm hr}$, 22% took $1 - 1.5^{\rm hr}$, 14% took $1.5 - 2^{\rm hr}$, while the rest took $> 2^{\rm hr}$ to complete. The image processing section of our pipeline runs on a parallelized CCD per CCD basis. This means that for the 80 exposures used for this analysis, there were ∼5000 jobs total. Post processing also runs on a CCD per CCD basis after image processing has finished. This step takes ∼20 min to finish when running with all exposures. We note that this turnaround time is significantly longer than the GROWTH team reported in (*Andreoni et al.*, 2019a). This is likely due to a combination of having, on

average, more template images and applying a more complete correction set in the single epoch stage, such as correcting for the brighter-fatter effect (*Bernstein et al.*, 2017).

3.4 Candidate identification

In total, there were 1165 candidates identified after post-processing. The final candidate list was published in GCN 24480 at 12:24 pm May 11 UTC (*Soares-Santos*, 2019). The primary cuts for our candidates require no `SExtractor` errors in image processing, such as masking of objects overlapping the transient or inability to measure the flux, and an `autoscan` score of at least 0.9 out of 1.0. This cut found 96 candidates (20 with `autoscan` score > 0.95), while the final 11 were selected via visual inspection. The key properties we looked for when performing visual inspection are a host galaxy in the template image, a non-noisy template image, and no regions of over or under-subtraction. We also took into consideration the possibility that the candidate could be an AGN since we are unable to resolve objects that are close to the center of the host galaxy and therefore disfavored stamps where the candidate is not distinguishable from the host galaxy. Further, we note that no candidate from our pipeline is fully dismissed until there is secondary follow-up or enough evidence to definitively categorize the object. For a single night of observations, our goal is to rapidly identify objects that are the most obvious candidates, then refine our search criteria as we observe more epochs.

Additionally, we matched candidates to hosts and used DES data to measure the properties of the host, such as photometric redshift, absolute magnitude, stellar

mass, and star formation rate, as well as the separation of the candidate and the host at the redshift of the nearest potential host galaxy. Photometric redshifts have been computed using Directional Neighborhood Fitting (DNF; *De Vicente et al.* 2016), while the galaxy properties have been computed using the Bayesian Model Averaging method as described in *Palmese et al.* (2020). The coordinates and other information about each of our candidates can be found in Table 3.1, and information about their host galaxies are listed in Table 3.2.

3.5 Results

3.5.1 Candidate Classification

The first stage of analysis, performed as exposures became available, presented 11 candidates (of which 6 were also detected by GROWTH) that were produced via the DESGW Search and Discovery Pipeline discussed in Chapter II. Follow up from other observatories is crucial for determining if a candidate is the GW counterpart through rejection of false positives. The Korea Microlensing Telescope Network (KMTNet) followed up five of our candidates, desgw-190510a, desgw-190510c, desgw-190510i, desgw-190510j, and desgw-190510k (GCN 24493 and 24529; *Im et al.* 2019a,b), at the KMTNet South Africa (SAAO), Chile (CTIO), and Australia (SSO) stations showing that each of these candidates did not have significant fading over $\sim$1 day, but did show very slow or no fading, therefore deeming these candidates likely supernovae. Additionally, desgw-190510c was observed by Swift-XRT (GCN 24541; *Evans et al.*

Table 3.1 Candidates that pass the DESGW pipeline cuts as well as visual inspection from the first stage of analysis. If the candidate matches a candidate from the GROWTH team's candidate list, the GROWTH name is stated. If additional follow up conducted by other telescopes verified the candidate as SN the classification is listed. Those labeled only "SN" did not have sufficient information for specific classification.

DES (GROWTH) Name	mag g	mag r	mag z	RA (deg)	DEC (deg)	`autoscan` Score	Classification
desgw-190510a	22.53 ± 0.19	20.93 ± 0.04	20.77 ± 0.10	91.526744	-35.541616	0.950	SN
desgw-190510b	21.19 ± 0.05	21.13 ± 0.05		93.704382	-36.980727	0.950	
desgw-190510c (DG19fqqk)	21.72 ± 0.1	20.37 ± 0.02	20.35 ± 0.06	92.851468	-36.517324	0.970	SN II
desgw-190510d (DG19nanl)	20.36 ± 0.03	19.92 ± 0.2	20.77 ± 0.11	87.311398	-35.955853	0.970	
desgw-190510e (DG19etsk)	20.56 ± 0.03	20.66 ± 0.03	20.82 ± 0.09	89.100926	-30.473987	0.970	
desgw-190510f	22.16 ± 0.13	21.30 ± 0.05		92.294458	-34.884684	0.970	
desgw-190510g	22.48 ± 0.17	21.92 ± 0.09		92.468923	-34.08657	0.963	
desgw-190510h	21.23 ± 0.08	20.29 ± 0.03	20.56 ± 0.07	87.762354	-27.956502	0.960	SN
desgw-190510i (DG19yhhm)		20.15 ± 0.02	20.47 ± 0.08	91.936973	-30.824747	0.915	SN
desgw-190510j (DG19zaxn)	20.65 ± 0.04	20.83 ± 0.04		92.307977	-35.149829	0.900	SN
desgw-190510k (DG19lcnl)	20.15 ± 0.03		19.53 ± 0.03	87.146843	-35.994357	0.920	SN

Table 3.2 Candidate host galaxies' information. Redshifts listed are mean photometric redshifts with one sigma errors. All photometric data, star formation rates (SFR), stellar mass ($M_\star$), and magnitudes are computed using DES Year 3 data. Additionally, the separation ("Sep") between candidate and host galaxy is calculated using the redshift of the galaxy. Galaxies are ranked based on their position in the sky and redshift, using the information provided in the skymap. Log indicates a logarithm in base 10.

Name	Host Gal. Name	Sep [kpc]	z	Log($M_\star$) Log([$M_\odot$])	Log(SFR) Log([$M_\odot$/yr])	M_i	Rank
desgw-190510a	2MASS J06060625-3532351	32.1	0.106 ± 0.004	$11.069^{+0.19}_{-0.05}$	-0.190	-23.043	3
desgw-190510b							
desgw-190510c	DES J061124.4562-363104.494	97.7	0.202 ± 0.098	$9.028^{+0.055}_{-0.060}$	-0.462	-20.071	9
desgw-190510d	WISEA J054914.81-355724.3	5.0	0.130 ± 0.021	$9.388^{+0.14}_{-0.09}$	-0.502	-19.33	4
desgw-190510e	WISEA J055624.41-302817.8	24.6	0.163 ± 0.005	$10.829^{+0.05}_{-0.12}$	-0.390	-21.796	8
desgw-190510f	2MASS J06091226-3452506	68.9	0.168 ± 0.003	$11.200^{+0.034}_{-0.034}$	-0.156	-22.685	7
desgw-190510g	DES J060952.4784-340540.704	218.3	0.575 ± 0.174	$9.517^{+0.17}_{-0.14}$	0.259	-20.557	10
desgw-190510h	2MASS J05510277-2757201	4.3	0.049 ± 0.002	$10.004^{+0.034}_{-0.052}$	-1.388	-20.917	1
desgw-190510i	WISEA J060745.00-304928.7	55.7	0.193 ± 0.019	$10.341^{+0.052}_{-0.041}$	0.387	-21.539	6
desgw-190510j	WISEA J060914.02-350858.5	3.1	0.134 ± 0.014	$9.69^{+0.14}_{-0.13}$	-0.461	-19.927	5
desgw-190510k	2MASS J05483537-3559390	1.9	0.067 ± 0.002	$9.829^{+0.09}_{-0.20}$	-0.272	-20.627	2

2019), showing no XRT source found, as well as with Magellan (GCN 24511; *Gomez et al.* 2019), which found a broad feature consistent with H-α at a redshift of 0.06 and suggests a good match to a Type II SN approximately one week after peak brightness. Finally, desgw-190510h was initially detected by ATLAS on March 13, 2019 and later classified as a Type Ia SN at redshift 0.07 roughly a few days after maximum light by the Spectral Classification of Astronomical Transients (SCAT) survey and desgw190510-b was recorded by Gaia on Jan 30, 2019 and reported as a "blue hostless transient". This transient can also be seen in previous DES images dating about 2.5 years ago, though with not enough information to classify it with certainty, thus we provide no host information in Table 3.2. This leaves only 4 candidates, desgw-190510d, e, f, and g, that were not classified by secondary follow-up, and thus still potential counterpart candidates.

The remaining information about each candidate that can be used to determine if a candidate is viable can be found in Table 3.2. The table reports photometric redshift, star formation rate, stellar mass, and absolute magnitude of the hosts, computed using DES Year 3 data (*Abbott et al.*, 2018). Furthermore, galaxies are ranked based on their probability of association, which can be computed using the skymap information, the galaxies' position and redshift (*Singer et al.*, 2016b), assuming a flat ΛCDM cosmology with $H_0 = 70$ km s^{-1} Mpc^{-1} and $\Omega_m = 0.3$.

3.5.2 Recovered Candidates

Using the same exposures, the GROWTH collaboration reported a list of 13 candidates (GCN 24467; *Andreoni et al.* 2019). Seven of the GROWTH candidates were

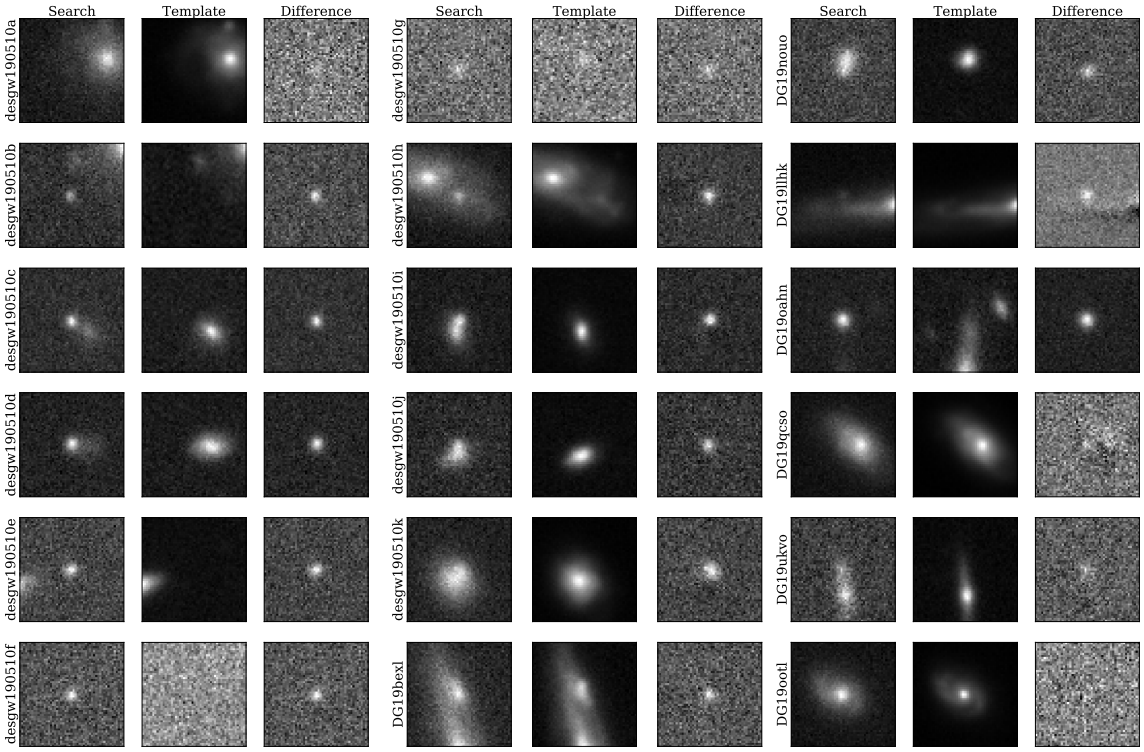

Figure 3.2 Stamps (search, template, and difference images) for all S190510g candidates found by DESGW, including 11 candidates detected in our short latency search (as reported in GCN 24480) and 7 candidates which were first reported by the GROWTH collaboration. Six of the GROWTH candidates were later found by our pipeline, while DG19ootl was not.

not listed in the initial DESGW candidate list reported in GCN 24480. Candidates DG19bexl and DG19nouo were found in the final stages by our automated pipeline; DG19bexl did not pass the `autoScan` score cut (≥ 0.9) and DG19nouo was rejected due to visual inspection. Candidates DS19qcso and DG19llhk both had a detection in a single exposure, where two were required to be picked up as a candidate. The overlapping search exposures for these candidates failed in the `HOTPANTS` step of our pipeline. Reprocessing of these exposures with an updated (current) version of the

DESGW pipeline did identify these candidates. Similarly, candidates DG19ukvo and DG19oahn were not found in our initial processing of the event due to `HOTPANTS` errors in all exposures. DG19oahn was later found in reprocessing, while DG19ukvo continued to have processing failures in 2 out of the 3 exposures. The fraction of missing candidates is consistent with the overall failure rate of 28% for all jobs that were submitted on that night, where $\sim$ 15% of total jobs failed due to issues in `HOTPANTS`. These failures are largely due to the observing conditions described in Section 4.2. Finally, candidate DG19ootl was never found in our pipeline. The templates used for this exposure were taken from not yet publicly available DES images and thus did not show any source in the difference image. Candidates, including those initially detected only by GROWTH, are shown in Figure 3.2.

3.6 Discussion

3.6.1 Understanding Search Efficiency

To better understand our search efficiency, we performed an offline analysis using SuperNova ANAlysis software suite (SNANA) (*Kessler et al.*, 2009). These simulations produce SN & KN light curves as they would be observed during our observations. Each KN simulation randomly assigns an ejecta mass, ejecta velocity, and lanthanide fraction based on the Kasen KN model (*Kasen et al.*, 2017), as well as host galaxy extinction between 0 and 3 mag (*Cardelli et al.*, 1989). The SN simulations use the SALT2 model for SN Ia (*Guy et al.*, 2010) and templates for the core collapse SN (SN CC) are taken from *Kessler et al.* (2010) and *Jones et al.* (2018).

Additionally, we note that these light curves are modeled assuming face-on emission of the observed component or spherically symmetric emission. While studies have shown the importance of viewing angle dependence on KN brightness (*Kawaguchi et al.*, 2020a; *Dhawan et al.*, 2020; *Korobkin et al.*, 2020), this approach was selected for simplicity.

Using these simulations, we computed the detection efficiency for each KN model given our observing conditions, the results of which are shown in Figure 3.3. The KN simulations used for this analysis produce events that use a distance distribution consistent with that reported by the LVC as well as being located within the 65% probability area that was surveyed. The efficiency of each model represents the fraction of light curves that are detected to be brighter than our five-sigma limiting magnitude at the time of DECam observations.

Next, we used these simulations to examine the color magnitude space for both KN and SN (Figure 3.4). For this analysis, we use both KN and SN simulations. Here we require the detected object to be brighter than our five-sigma limiting magnitude. Additionally, we require the object's host-galaxy photometric redshift to be consistent with the LVC luminosity distance posterior at the 3σ confidence level. Additionally, the simulated SNe were distributed in redshift according to the measured volumetric rates of SNe-Ia and SNe-CC.

3.6.2 Implications for Search Efficiency

Figure 3.3 shows the likelihood that we would have been able to detect a KN produced by this event given the observing conditions and depth of observations.

Here we show all possible sets of KN parameters and note that a GW170817-like KN follows a two component model, red and blue, where the blue component is dominant at early times (i.e. up to ~ 2.5 days after merger (*Kasen et al.*, 2017)) in the light curve evolution. Assuming S190510g is a GW170817-like KN viewed from the same orientation located within our exposures, our simulations show that we would have a 99% chance of detecting the counterpart KN. However, a wide range of KN models would have been outside of our sensitivity range and thus unobservable.

While we have the ability to detect such a source, it is challenging to determine a candidate to be KN or SN with a single night of observations in the absence of spectroscopic information. To demonstrate the difficulty of this task we examined the color magnitude space of the simulated KN and SN events. All KN simulations are shown as the blue contours (indicating 50% and 90% density of simulations) in the left panel of Figure 3.4, with the parameters for the blue component of GW170817 (ejecta velocity = 0.3c, lanthanide fraction = 10^{-4}, ejecta mass =$0.025M\odot$, and assuming spherically symmetric emission) highlighted as orange contours. Meanwhile, the color magnitude distribution of SN simulations is shown by the green contour on the right panel of Figure 3.4. All DESGW S190510g candidates from this event (depicted as red crosses in Figure 3.4) fall within the possible 90% color-magnitude regions of SN events. For a KN roughly one day after burst, and given only this color-magnitude information, each of these candidates could be either an SN or KN.

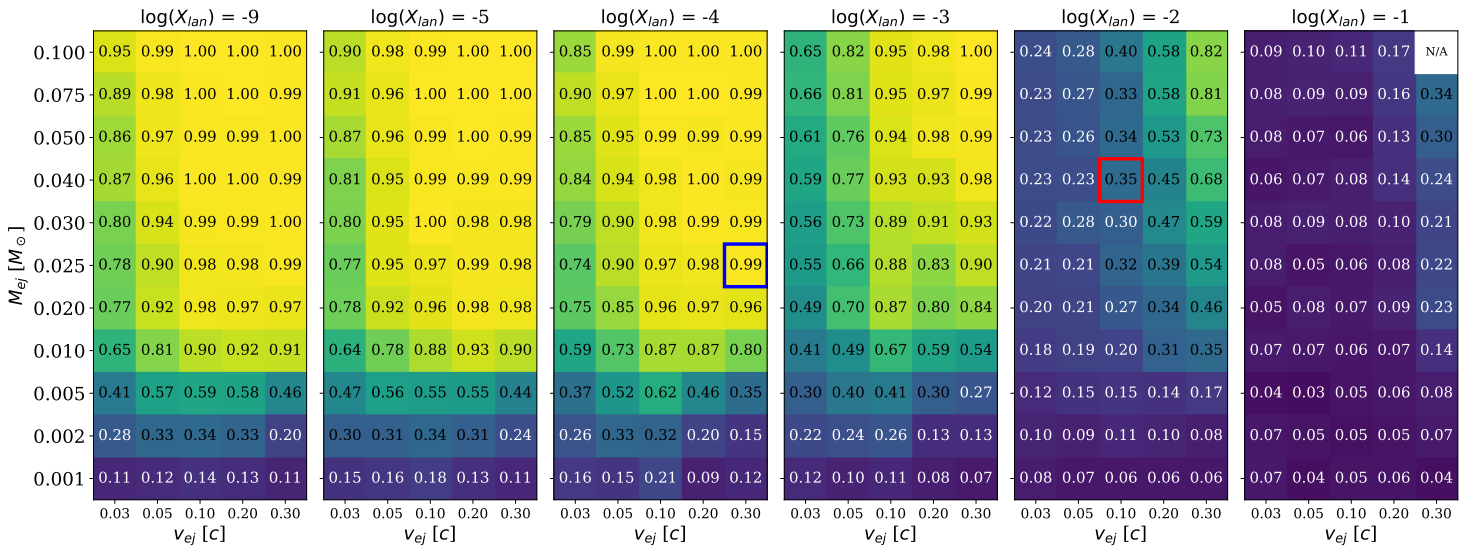

Figure 3.3 Summary of detectable kilonovae given the observing conditions of May 11th, 2019. Simulations are set within the LVC distance range of S190510g. Parameters determining the components of the KN, ejecta mass ($M_{\rm ej}$), ejecta velocity ($v_{\rm ej}$), and the log of lanthanide ($\log {\rm X}_{\rm lan}$) fraction, are taken from (*Kasen et al.*, 2017). The coloring and labeling in each box denote how likely we would be able to detect a KN with the given parameters assuming the event is within our observations. The box labeled "N/A" is a combination of parameters not available in the *Kasen et al.* 2017 parameters. Additionally, we highlight the set of parameters that were identified as the likely red and blue component of GW170817 as red and blue boxes.

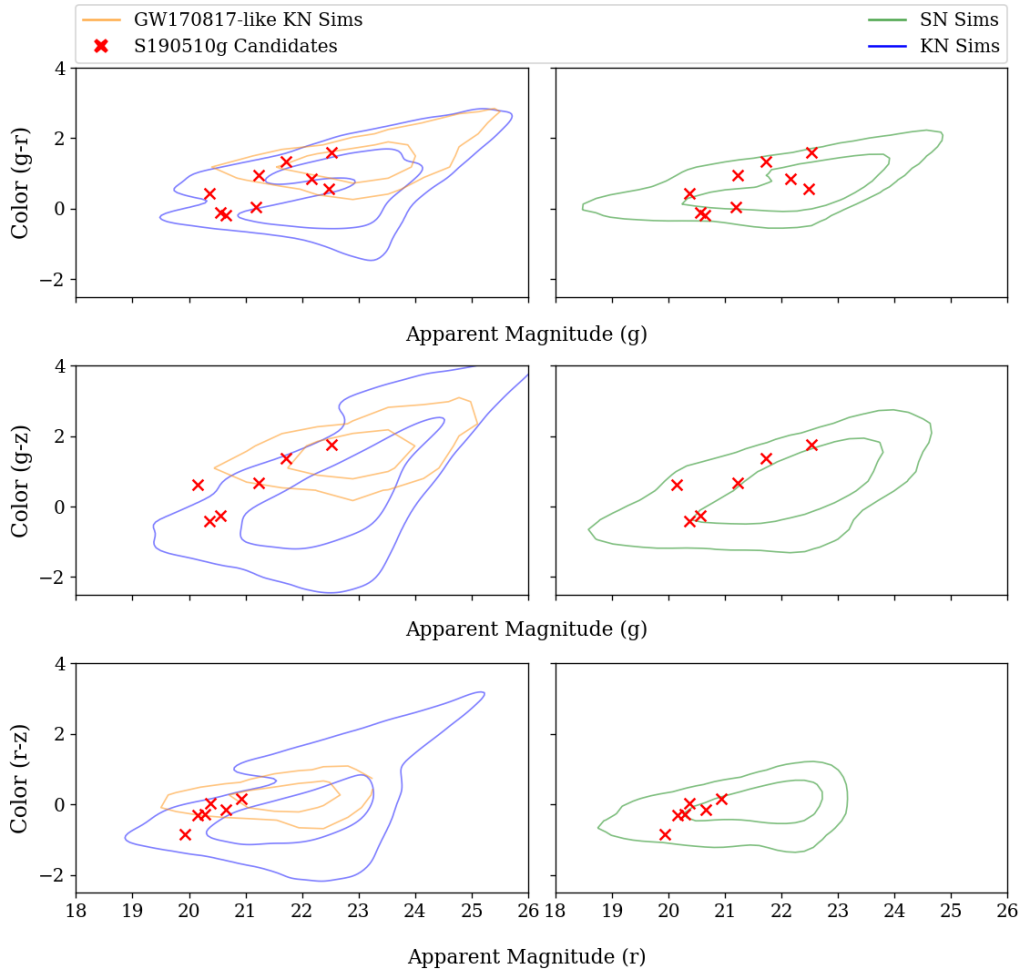

Figure 3.4 DESGW candidates (red) as compared to where kilonovae and supernovae would be expected to live in color magnitude space given the observing conditions of our observations (i.e., 36 hours after merger, sky brightness, etc.). All simulations run using SNANA (*Kessler et al.*, 2009). Kilonovae simulations were generated with a burst date consistent with that reported by LVC, and at a distance consistent with the LVC distance distribution (blue contours). The KN parameters, ejecta velocity, mass, and lanthanide fraction are randomly selected from the parameters described by Kasen 2017. Simulations with the same Kasen parameters as the blue component of GW170817 (ejecta velocity = 0.3c, lanthanide fraction = 10^{-4} and ejecta mass $=0.025M\odot$) are shown as orange contours. Supernovae simulations consist of Type Ia and CC SN, and are generated using a peak date ranging 4 months centered around May 10th, with redshift also consistent with S190510g's distance distribution. The contours show 50% and 90% density of simulations.

3.6.3 Implications for Follow Up Strategy

In the first half of the O3 observing run, most of the events that included a neutron star did not have a good localization (i.e. hundreds of deg^2) as well as being far away (>200 Mpc) when compared to GW170817. While it would be ideal to cover 100% of the localization area with multiple filters, limited telescope time and poor localization maps make this very challenging. In the following, we show that prioritizing sufficiently deep images as opposed to covering large areas and/or using multiple filters, will result in a higher chance of detecting counterparts.

To show how many events it would take to have a 50% (99%) chance of detecting one counterpart, we have to consider the cumulative probability inside the LVC localization map that was observed ($\Sigma_{\rm spatial}$), the fraction of DECam that was live during observations ($\epsilon_{\rm camera}$), the probability that the event is astrophysical in nature ($\epsilon_{\rm real}$), and our likelihood of being able to detect a KN at that distance given the observing conditions (i.e. the fraction of simulated light curves that are brighter than our five-sigma depth) ($\epsilon_{\rm efficiency}$)

$$P_i = \Sigma_{\rm spatial} \times \epsilon_{\rm camera} \times \epsilon_{\rm efficiency} \times \epsilon_{\rm real} \tag{3.1}$$

$$P_{\rm one} = 1 - \prod_{i}^{N} (1 - P_i) \tag{3.2}$$

Here, P_i is the probability of being able to detect at least one KN from a single GW event. $P_{\rm one}$ is the cumulative probability of being able to detect a single counterpart given N GW events (*Annis and Soares-Santos*, 2016). For this calculation, we find that if we assume there is a kilonova associated with S190510g that is GW170817-

like, i.e. ($\epsilon_{\text{efficiency}} = 0.993$), we would need to observe 3 (19) identical events with $\Sigma_{\text{spatial}} = 0.65$, $\epsilon_{\text{camera}} = 0.8$, $\epsilon_{\text{real}} = 0.42$, and $\epsilon_{\text{efficiency}} = 0.993$ in order to have 50% (99%) probability of identifying the event using the current strategy. Since there is no way of knowing that the event will have a light curve similar to GW170817, we also calculate this using the average efficiency value of all KN parameters, $\epsilon_{\text{efficiency}} = 0.553$ with all other parameters the same. Here we find that we would need 6 (36) events to reach 50% (99%) likelihood of detecting the counterpart.

We then repeat this calculation assuming the observing strategy uses one filter instead of three. If we conserve the telescope time used and area surveyed per event, we can then increase the exposure time from 40 seconds to 170 seconds. In this scenario, the efficiency for a GW170817-like KN is 0.995, meaning we would again need 3 (19) events to have 50% (99%) likelihood of detection. Using the average efficiency in this scenario though, 0.742, we would only need 4 (27) events to have 50% (99%) likelihood of detecting a counterpart. By increasing the depth of our observations, we become sensitive to more KN models and will thus need to observe fewer total GW events to have a high probability of making a detection.

3.7 Conclusion

We performed a follow up analysis of the GW trigger S190510g, using DECam target of opportunity time data from May 11th, 2019. We demonstrated the DESGW team's ability to quickly process new images in real time, averaging $\sim$ 1hr for image processing to complete. The final DESGW candidate list is summarized in Table 1, with five candidates, desgw-190510a, c, i, j, and k being ruled out due to

secondary follow up efforts by KMTNet, Swift-XRT, and Magellan. Similarly, candidates desgw-190510b and h have been identified based on previous observations as recorded in the Transient Name Server. This leaves 4 candidates from the DESGW candidate list that were not classified by secondary follow-up. Each of these candidates has color information that is consistent with SN as well as KN.

Additionally, we used simulated KN to show the efficiency of detecting a KN counterpart given the observing conditions of the observations to find that we have a 99% chance of being able to detect a KN counterpart assuming the light curve has the same physical parameters as GW170817 using the *Kasen et al.* (2017) model (Fig. 3.3) within our observations. However, this efficiency is not uniform across all KN models. We also used KN and SN simulations to study where in color magnitude space they land. We find that all of our candidates are consistent with both KN and SN using this metric.

To make ourselves more sensitive to all KN models, we suggest prioritizing longer exposure times over multiple filters and covering large portions of the localization area for future observations. Using exposures that are 4 times longer than those used for this follow up, we would only need to observe 4 events (identical to S190510g) to have a 50% chance of detecting a KN counterpart within the 65% probability region observed and with these observing conditions, compared to the 6 events needed using the current strategy.

CHAPTER IV

GW190814[1]

In this Chapter, we present the results of our search for the electromagnetic counterpart of GW190814, a merger of a black hole and a 2.6 solar mass compact object, possibly the first neutron star-black hole event detected by LIGO/Virgo. To quantify the sensitivity of our search, we applied our selection criteria to full light-curve simulations of supernovae and kilonovae as they would appear in the DECam observations. We find that, if a kilonova occurred during this merger, configurations where the ejected matter is greater than 0.07 solar masses with lanthanide abundance less than $10^{-8.56}$ and velocity between 0.18c and 0.21c are disfavored at the 2-sigma level. Furthermore, we estimate that our background reduction methods are capable of associating gravitational wave signals with a detected electromagnetic counterpart at the 4-sigma level in 95% of future follow-up observations.

[1]This chapter is published as *Morgan et al.* (2020)

4.1 LIGO/Virgo Observations

On 2019 August 14, The LIGO/Virgo Collaboration (LVC) reported the observation of gravitational radiation at high statistical significance (*Abbott et al.*, 2020b). The event, named GW190814, occurred when all three detectors (LIGO Hanford Observatory, LIGO Livingston Observatory, and Virgo Observatory) were operating normally, which enabled both high precision localization of the source and more precise waveform parameter estimation. The false alarm probability was calculated at 2.0×10^{-33} Hz, once per 10^{15} Hubble times, suggesting a very high signal-to-noise ratio event (*LVC*, 2019). The source of the GW signal was localized to a 38 (7) sq. degree area at the 90% (50%) confidence level in the southern hemisphere on the night of the merger. The localization area was split into two distinct regions, shown in Figure 4.1, as a result of polarization and timing information from the three-detector detection. Preliminary parameter estimation using the `bayestar` pipeline classified the event as falling into the "Mass-Gap", meaning the detected GW was consistent with at least one of the objects having mass between 3 $M_\odot$ and 5 $M_\odot$. The small localization area and the presence of a low-mass compact object, potentially a massive neutron star, made this event interesting from the perspective of electromagnetic follow-up (*Littenberg et al.*, 2015). The following day, the LVC `LALInference` pipeline localized the source to 23(5) sq. degrees at the 90% (50%) confidence level, refined the classification to an NSBH merger, and estimated the luminosity distance of the event to be 267 ± 52 Mpc. DECam follow-up observations proceeded based on this information, but in June 2020, the LVC released its final parameter estimation values for GW190814: the luminosity distance was revised to 239 ± 43 Mpc; the

90% localization area was reduced to an 18.5 sq. degree section of the original 90% localization area; and the masses of the objects involved in the merger were refined to 23.2 $M_\odot$ and 2.6 $M_\odot$ (*Abbott et al.*, 2020b).

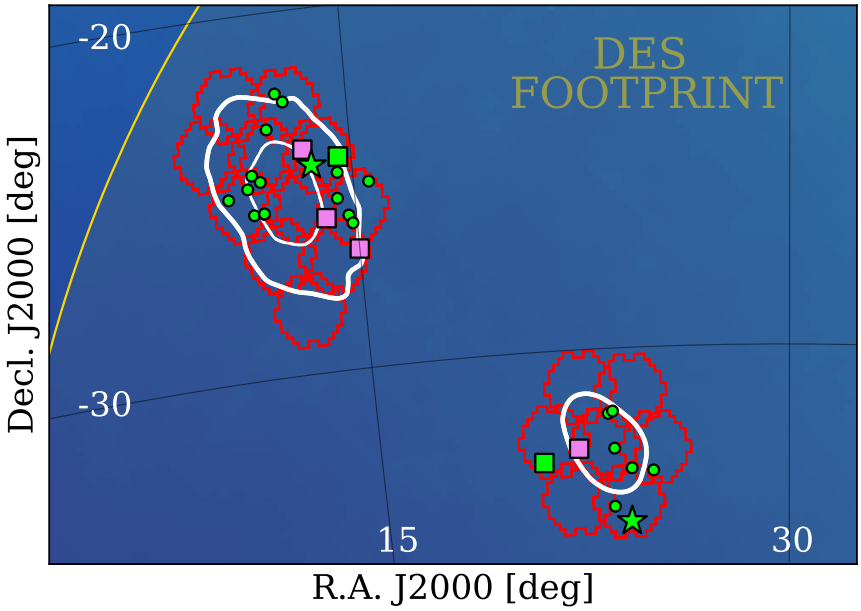

Figure 4.1 Summary of exposures taken and candidates identified by the DESGW pipeline. DECam pointings are shown as orange hexes and represent the area covered on nights 2 - 5. Additional images were taken using a different tiling in order to eliminate chip gaps, those hexes are not shown for simplicity. The white contours are the LVC 90% (bold) and 50% probability region. Finally, the gold line represents the boundary of the DES footprint. Stars represent candidates that pass all selection criteria prior to final ML classification and have not been targeted with spectroscopic instruments. Circles show candidates reported via GCN circulars that were ruled out in this analysis. Squares denote candidates that were spectroscopically confirmed as SNe. Violet coloring indicates a candidate was first reported by a group other than DESGW, while green coloring is used for DESGW candidates.

4.2 DECam Observations

In search of an EM counterpart to GW190814, we triggered Target of Opportunity (ToO) observations with the 4m Victor M. Blanco Telescope located at Cerro Tololo Inter-American Observatory in Chile. The Blanco was equipped with DECam, a 570-mega pixel optical imager (*Flaugher et al.*, 2015). Together, the Blanco and DECam reach a 5σ limiting r-band magnitude of ~ 23.5 mag in a 90 second exposure in a 3 sq. deg field of view (FoV) (*Abbott et al.*, 2018). The combination of deep imaging and a wide FoV makes Blanco/DECam the ideal southern hemisphere instrument for efficiently detecting explosive optical transients localized to tens of square degrees.

4.2.1 Observing strategy

We performed ToO follow-up observations of GW190814 0, 1, 2, 3, 6, and 16 nights following the LVC alert. The early nights were chosen to look for rapidly evolving transients immediately following the merger, and the observations 16 nights after the merger were used to exclude persisting supernovae. The observing conditions for each night are displayed in Table 1 of *Morgan et al.* (2020).

The moon was full on the first night of the observations, so we opted to use the redder i and z bands to minimize the effect of moon brightness on our imaging depth. On the night of the merger, we tiled 99% percent of the 38 sq deg localization region using 60 second exposures in i and 90 second exposures in z. The z exposures were offset by half the width of a DECam CCD to fill in chip gaps. We tiled the area a second time in i to identify moving objects. On the following observing nights, since the LVC had published a smaller localization region, we lengthened

our exposures to 100 seconds in i and 200 seconds in z. Throughout the real-time observations, we coadded images that shared the same night and filter to increase the search depth. The i-band DECam pointings are shown atop the LVC localization probability contours in Figure 4.1. All DECam images were immediately made public and available for download from the National Science Foundation's NOIRLab.

4.2.2 Image Processing

The DECam images were processed by the DES Difference Imaging Pipeline, an updated version of the DES Supernova Program's Pipeline described in *Kessler et al.* (2015), using coadded DES wide-field survey images as templates. The updated pipeline is described in Chapter II.

4.2.3 Host Galaxy Matching

We match each candidate to a host galaxy from the DES Y3 galaxy catalog. After removing contaminants (subtraction artifacts, variable stars, moving objects, etc.) from our sample using criteria 1-5 described in Section 4.3, every candidate is able to be matched to a host in the DES Y3 galaxy catalog. Properties and redshifts of the hosts are reported in Table 4.1. Photometric redshifts have been computed using Directional Neighborhood Fitting (DNF; *De Vicente et al.* 2016), while the galaxy properties have been computed using the method described in *Palmese et al.* (2020). The DNF method is known to be inaccurate at the redshifts relevant in this analysis due to the characteristics of the galaxy sample upon which the algorithm was trained. The inaccuracy manifests in our analysis as underestimated host galaxy photometric

Table 4.1 Host galaxy properties of the two objects passing all selection criteria prior to final classification.

Candidate ID	666914	661188
Host Galaxy	DES J013624.60-344557.72	DES J005431.17-241713.08
Angular Sep. [arcsec]	3.345	4.700
Physical Sep. [kpc]	6.24	9.53
Redshift	0.10 ± 0.02	0.11 ± 0.02
log Mass [$M\odot$]	9.90	10.07
log SFR	-0.0386	0.0438
Absolute Mag (M_i)	-20.70	-20.94

redshift uncertainty. We therefore add a minimum uncertainty of 0.02 for galaxies with host galaxy photometric redshift less than 0.1 following the prescription of *Soares-Santos et al.* (2019e). The galaxies have been ranked from highest to lowest probability per unit volume based on their angular position and redshift as prescribed in *Singer et al.* (2016b), assuming a flat ΛCDM cosmology with $H_0 = 70$ km s^{-1} Mpc^{-1} and $\Omega_m = 0.3$.

4.3 Candidate Selection

After the completion of our image processing pipeline, we found 33571 candidates. The data sample includes astrophysical objects with varying brightness such as SNe, Active Galactic Nuclei (AGN), and other less-common explosive optical transients (*Cowperthwaite and Berger*, 2015), moving objects such as minor planets and asteroids, foreground variable stars in the Milky Way, and image artifacts from poor image subtractions and insufficient masking of bright objects. In the real-time analysis, we developed several selection criteria to look for the likely EM counterpart of

the GW detection. These selection criteria narrowed our sample to a size reasonable for spectroscopic, X-ray, and radio observing teams to follow up. We detail those selection criteria here and evaluate their effectiveness at recovering KNe and rejecting background objects in the following section.

There are 9 selection requirements (criteria) in four levels: (1) subtraction quality requirements to reject image artifacts and moving objects, (2) catalog matching to rule out existing objects such as AGN and variable stars, (3) KN-specific requirements to rule out SNe, and (4) final candidate assessment using machine-learning (ML) based photometric classification. Each level progressively targets more specific properties of an expected EM counterpart. The numbers of candidates remaining in our sample after each criterion are displayed in Table 4.2. The remainder of this section elaborates on the implementation and motivation for each selection criterion applied to the data.

4.3.1 Level 1 Selection Criteria

The following selection criteria assure satisfactory detection and image-subtraction quality in all remaining candidates. We introduce two definitions to expedite discussion. A Type-2 detection is a `SExtractor` detection in a single filter that does not contain any image processing errors. These errors include an inability to measure a fitted flux, the R.A. or Decl. of an object not being on a CCD, masking of bright objects overlapping the transient object, the inability to fit the PSF of the object, the inability to make a stamp in the difference image, a large number of pixels with negative flux values, and a 5σ difference between psf flux fitting and aperture flux fit-

ting. A Type-1 detection is a Type-2 detection that has also been given an `autoscan` score of 0.7 or larger.

Criterion 1. We require candidates to have at least one Type-1 detection. This criterion ensures a high-purity sample of real objects with little contamination from image processing artifacts.

Criterion 2. We require a second detection in the light curve of Type-2 or Type-1, and we require this secondary detection to be on a different night from the detection in Criterion 1. By ensuring a second detection that is separated in time from the first detection, we remove all moving objects from our sample. This temporal separation could in principle be shortened to $\sim$ 1 hour, but because we co-added our images from the same night and band, this time separation requirement is effectively a multi-night requirement. In these observations, we find that fast-fading transients such as KNe have a high efficiency of 93% for this multi-night requirement based on the simulations discussed in Section 4.4. We also relax the required `autoscan` score of the second detection since the first Type-1 detection from Criterion 1 has already yielded a high-purity sample.

After the level-1 quality criteria, we are left with 2192 candidates in our sample. This sample is mostly composed of astrophysical objects with observed variable brightness as a result of the quality criteria. There is a large population of artifacts still present at this stage that passed the selection criteria, but these are removed by Criterion 5.

4.3.2 Level 2 Selection Criteria

With the exception of artifacts, we expect the remaining sample to be dominated by three main contaminants at this stage: variable foreground stars, AGN, and bright galactic centers. The latter is a known problem in difference imaging, see *Kessler et al.* (2015) or *Doctor et al.* (2017) for context.

Criterion 3. We require that each object is separated from known foreground objects. This requirement has two components: each object must be separated from objects in a high purity sample of well-measured stars in the DES Y3 Gold catalog by at least $0.5''$, and each object must be separated at least $8'$ from NGC288 and $3'$ from HD4398. The globular cluster NGC288 has a high density of bright stars and HD4398 itself is a very bright star, both of which led to large numbers of subtraction artifacts and variable star detections by our Search and Discovery Pipeline.

Criterion 4. We require that each object is at least $0.2''$ from objects in the DES Y3 Gold catalog that are not flagged as well-measured stars, which were addressed in Criterion 3. This criterion aims to remove AGN and bright galactic centers. Section 4.4.2 gives physical and empirical motivations for expecting KNe to be highly likely to satisfy this requirement.

Criterion 5. We visually inspect images of the 1872 remaining candidates. We remove candidates that have an imaging artifact from a misaligned subtraction or from inadequate masking and we also remove all candidates that contained a point-like light source in the template image at the location of the detected transient. In the application of this criterion in general, the seeing of the observations can limit the efficiency of real transients, since extremely poor seeing could potentially make

a bright host galaxy center appear as a point source. Our average seeing in these observations, shown by the PSF FWHM column in Table 1 of *Morgan et al.* (2020), is less than $1.3''$ on more than half of the nights. We therefore expect this behavior to be rare in our data.

After the level-2 catalog criteria, we are left with 116 candidates in our sample. We expect that at this stage our data are almost entirely constituted by real astrophysical transients.

4.3.3 Level 3 Selection Criteria

The following selection criteria are designed to remove supernovae by assuring the distance of the candidates is consistent with the LVC distance posterior distribution, requiring the light curves of the candidates are fading, and triggering spectroscopic follow-up observations.

Criterion 6. We require each object to have a host galaxy photometric redshift consistent with the mean and standard deviation of the LVC distance posterior at the 3σ confidence level. All objects were able to be matched with a host-galaxy at this stage, so the criterion can be straightforwardly applied. The criterion is satisfied when

$$\frac{|z_{\rm LVC} - z_{\rm DES}|}{\sqrt{\sigma^2_{z,\rm LVC} + \sigma^2_{z,\rm DES}}} < 3, \tag{4.1}$$

where $z_{\rm LVC} = 0.06$ is the redshift of GW190814, $z_{\rm DES}$ is the redshift of a candidate's host galaxy, $\sigma_{z,\rm LVC} = 0.005$ is the uncertainty on the redshift of GW190814, and

$\sigma_{z,\mathrm{DES}}$ is the uncertainty on the redshift of a candidate's host galaxy. To implement this criterion, we use the assumed cosmology in this analysis. In the case of an available spectroscopic redshift of the host galaxy, we utilize the spectroscopic information instead. Since supernovae could be detectable out to large redshifts in these observations, we seek to remove contaminants in galaxies too distant to be associated with the GW signal.

Criterion 7. If an object is detected on the final night of observations (16 nights post-merger) we require that it be fainter than 22.5 mag in at least one band. If an object is not detected on the 16th night, it passes this criterion. This criterion removes rising and flat light curves from our candidate list.

Criterion 8. We trigger spectroscopic follow-up observations from the Southern Astrophysical Research (SOAR; *Sebring et al.*, 2003) telescope on as many of the 8 remaining candidates as possible. We also incorporate real-time spectroscopic classifications from other instruments during the follow-up based on circulars posted to the GCN. The spectroscopic instruments were triggered in real-time, as opposed to after the selection criteria had been refined in the offline analysis, so there is no perfect overlap between the targeted objects and the remaining candidates presented in this work. All targeted candidates were spectroscopically confirmed as SNe.

4.3.4 Final Candidate Assessment

After the previous eight criteria have been enforced, we have two remaining candidates as shown in Figure 4.2. As described in the Appendix of *Morgan et al.* (2020), we apply light-curve-based ML classification to determine the probability that any of

these objects are potentially a KN. Briefly, we fit a large set of simulated SNe (both SNe-Ia and SNe-CC) and KNe (from the *Kasen et al.* (2017) models) light curves that pass Criteria 1 through 7 with a Bayesian SN template fitting tool `PSNID` (*Sako et al.*, 2011), select the template features and goodness of fit metrics with the largest difference in mean value for SN and KN samples, and build a random forest classifier (*Breiman*, 2001) using those best-fit parameters as features. This `PSNID+RFC` approach shows a significant improvement in classification power when using the KN false positive rate and KN true positive rate as diagnostics. A similar version of this method is described in *Morgan et al.* (2019). Figure 4.3 shows the performance of this machine learning approach and the resulting probabilities of each remaining candidate being a KN. DESGW-666914 has a 0.92 probability of being an SN and DESGW-661188 has a 0.86 probability of being a SN from our `PSNID+RFC` approach, both of which are classified as SNe based on our choice of operating threshold. Six additional candidates that made it to this stage and were later spectroscopically typed as SNe were correctly classified as SNe by our `PSNID + RFC` approach.

Table 4.2 shows the number of candidates remaining after each criterion, namely:

0 DES Difference Imaging Pipeline

1 Single Type-1 Detection

2 Two Type-2 Detections on Different Nights

3 Separated from Foreground Objects

4 Separation $> 0.2''$ from DES Y3 GOLD Catalog Galaxy Centers

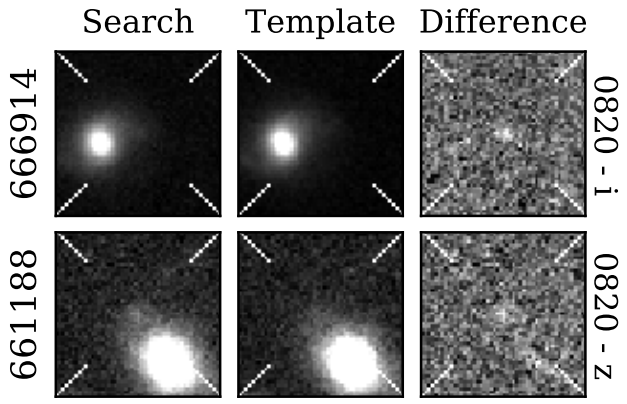

Figure 4.2 Images of objects passing all selection criteria before machine-learning classification. For each object, the set of images for the night with the least noisy difference image is displayed. All images are centered on the detected transient. The DESGW ID of the object is listed on the left axis label, while the "MMDD" date and filter used are shown on the right axis label. Each image has dimensions 13.4″ × 13.4″.

Table 4.2 The selection criteria developed in this analysis and remaining objects after each criterion. The candidates column refers to objects found by the DES Difference Imaging Pipeline and the latter two columns show the expected number of SNe present in the candidate sample at each level computed as described in Section 4.4.1. The SNe simulations were realized 500 times so statistical uncertainty is negligible. The horizontal dividers reflect the "levels" of selection criteria described in the text.

No.	Candidates	Sim. SNe-Ia	Sim. SNe-CC
0	33571	768.3	1191.1
1	2563	200.6	86.33
2	2192	118.8	48.29
3	2021	117.8	47.9
4	1872	96.7	42.0
5	116	85.2	38.1
6	9	4.7	6.5
7	8	2.6	4.8
8	2	0.8	1.4

5 Visual Inspection of Stamps

6 Redshift Consistent with LVC within 3 Standard Deviations

7 Fainter than 22.5 mag on Night 16

8 Not Eliminated by Spectroscopic Observations

9 Machine Learning Photometric Classification

After all selection criteria have been applied and the remaining candidates have been photometrically classified, zero candidates remain. We therefore use our data to set upper limits on KN properties given a non-detection and to inform future follow-up observations.

4.4 Sensitivity Analysis

To evaluate the selection criteria applied during the real-time observations, we model our search and selection methodology on simulated SNe and KNe using the SuperNova ANAlysis software suite (`SNANA`; *Kessler et al.*, 2009). The SNe and KNe models employed here are the same models used in the Photometric LSST Astronomical Time-series Classification Challenge (PLAsTiCC; *Kessler et al.*, 2019). The SNe templates are derived from observations while the KNe templates are generated from theoretical models. `SNANA` incorporates the cadence, the measured zeropoints, and noise level in the search and template images from our observations into the simulated fluxes and uncertainties to produce realistic light curves. This simulation process enables the application of our real-time selection criteria to simulations and

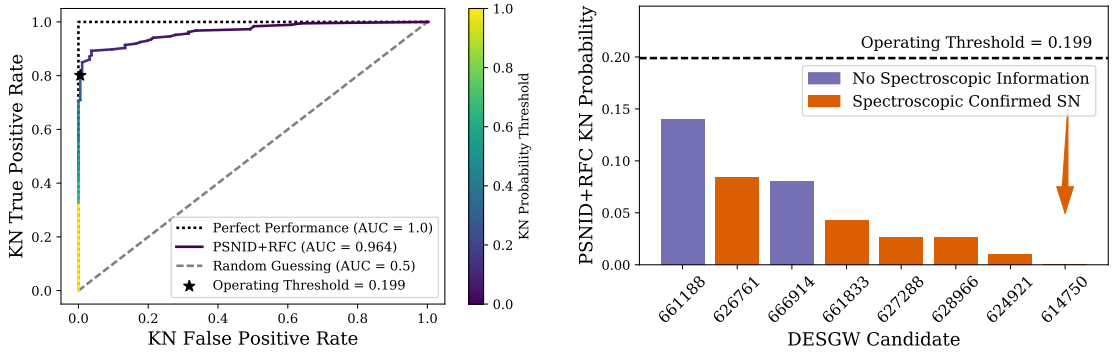

Figure 4.3 Photometric classification of candidates using the `PSNID + RFC` approach. *Left:* Receiver Operating Characteristic Curves showing classification power of the `PSNID + RFC` approach. The threshold at which we chose to operate the classifier is denoted by a black star, the location of which shows the false positive rate and true positive rate of our ML approach. *Right:* Calibrated probabilities of candidates passing Criterion 7.

DECam candidates for a better understanding of what objects and how many of them would be expected to pass our selection criteria. In the remainder of this section, we describe the `SNANA` simulations for the GW190814 observations, detail the modeling of the selection criteria in the context of the simulations, and present the results of our sensitivity analysis: detection efficiencies for 329 different KN models, expected numbers of SNe to pass our selection criteria, the mean light curves of objects passing our selection criteria, upper limits on physical properties of potential EM counterparts to the GW190814 merger, and statistical forecasting of our discovery potential in follow-up observations of future events.

4.4.1 Simulating the DECam Search

`SNANA` enables the simulation of light curves of SNe, KNe, and other transients as they would be measured by DECam during observations. This process uses a measured or theoretical time-evolving spectrum for the transient object and then accounts for cosmological redshift, Milky Way dust extinction, and the measured observing conditions of the DECam observations such as sky brightness, zeropoints, the point-spread-function of the imager, and CCD noise in the camera. The corrected time-evolving spectra are then multiplied by the transmission of the DECam filters and light curves are sampled at epochs matching the cadence of the observations.

The KN models used in the simulations are from spectral energy distributions derived in *Kasen et al.* (2017) and parameterize the optical light from a KN by the mass ejected in the explosion, the abundance of lanthanide elements in the ejecta, and the velocity of the ejecta (hereafter M_{ej}, X_{lan}, and v_{ej}). These models were chosen because they characterize the optical behavior based on physical properties of the NS ejecta, rather than having a dependence on the geometry or dynamics of the merger itself. While other models for KNe and models specific to NSBH mergers exist (*Barbieri et al.*, 2019; *Bulla*, 2019; *Hotokezaka and Nakar*, 2020, among multiple others), we find this simple, agnostic, three-component model based on observable properties of NS ejecta to apply well to GW190814. In the simplicity of this approach, we make the assumption of either spherically symmetric emission or that the particular component being considered is directed toward Earth. We use 329 total models, which discretize the parameter space in the ranges $0.001\ M_{\odot} \leq M_{ej} \leq 0.1\ M_{\odot}$, $0.03c \leq v_{ej} \leq 0.3c$, and $1 \times 10^{-9} \leq X_{lan} \leq 1 \times 10^{-2}$. The

simulated KNe are uniformly drawn from this population of models, though the grid which discretizes the parameter space is non-uniform as shown in Figure 4.4. This non-uniform grid is not believed to have an effect on the physical constraints insofar as the interpolation of model efficiencies between points in the grid is smooth and monotonic. As a proxy for the observer-frame explosion time of the simulated KNe, we fix the time the KNe fluxes reach 1 percent of their peak flux to the time of the LVC GW alert and note that this approximation is justified by the rapid rise times of the KNe. The simulated KNe are also distributed in redshift according to a polynomial fit of the LVC distance posterior and the cosmology used in this analysis. The redshift distribution is constructed independent of spatial information on the sky. This approximation is based on the small localization area of GW190814, however for future events with larger localization areas, the volume-rendered luminosity distance distribution should be utilized.

Because our selection criteria effectively remove all moving objects, known foreground variable stars, and AGN, the most likely remaining contaminants in our data are SNe. We therefore use SN simulations to understand the types of SNe passing our selection criteria, as well as the number expected to be present in our final candidate sample. We simulate type-Ia SNe (SNe-Ia) using templates from (*Guy et al.*, 2010) and measured volumetric rates from (*Dilday et al.*, 2008). We also simulate core-collapse SNe (SNe-CC) using templates from *Kessler et al.* (2010) and volumetric rates from *Li et al.* (2011). The SNe-CC population includes type-Ib, type-Ic, type-Ibc, type-IIP, type-IIN, and type-IIL SNe, and we weight the different sub-types according to their measured volumetric rates. Unlike the KN sample, we allow the

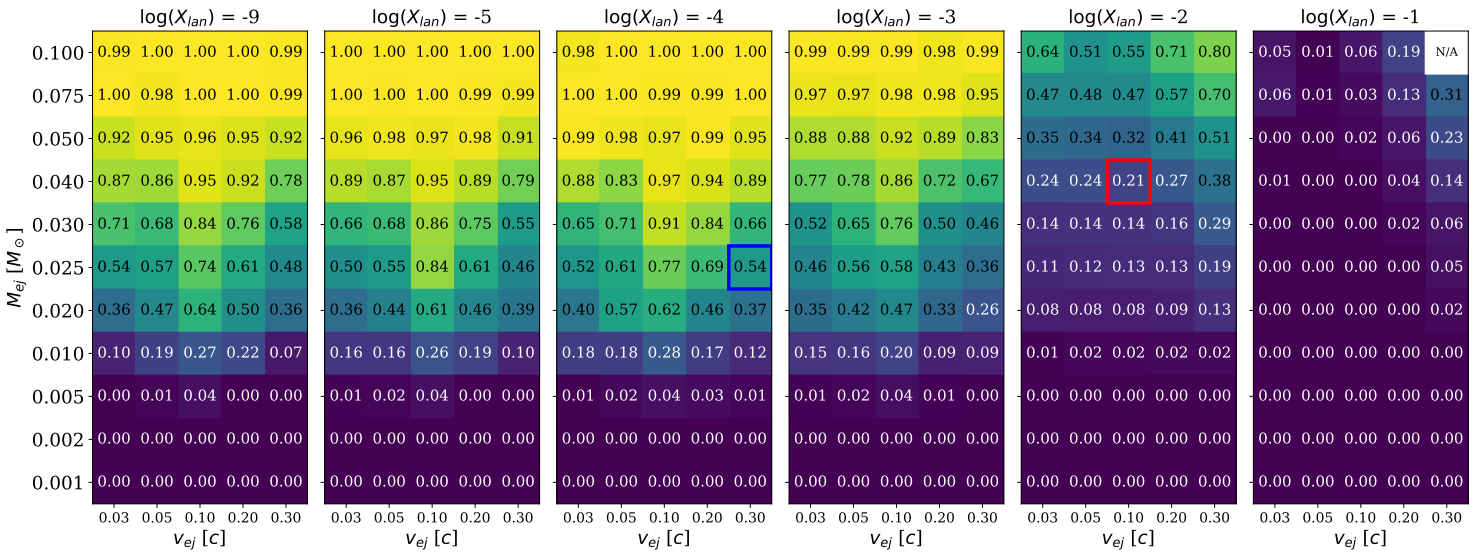

Figure 4.4 KN efficiency parameterized by M_{ej}, v_{ej}, and X_{lan}. The blue and red boxes correspond to the blue and red components of the best-fit model for a GW170817-like KN at the distance of GW190814. The top row shows the efficiencies of KN light curves in our observations after Criterion 1. The parameter combination marked "N/A" is excluded because it is believed to be not well-motivated physically (*Kasen et al.*, 2017). Heatmaps of the efficiency after all non-ML selection criteria have been applied and after ML classification can be found in Figure 4 of *Morgan et al.* (2020).

SNe to have a random observer-frame explosion time that would make them bright enough to observe with DECam during our observing window. This explosion time range is implemented by requiring the date of peak flux to be greater than 60 days prior to the LVC GW alert and less than 30 days after it since the explosion time itself is not well-measured.

4.4.2 Modeling Selection Criteria

`SNANA` produces catalog-level photometric fluxes for transient objects by correcting model spectral energy distributions and multiplying them with the DECam filters, and this approach bypasses several image processing and catalog matching steps that we apply to the real DECam data. We therefore take additional steps to impute information necessary for modeling the selection criteria in this analysis on the simulated light curves.

In our real-time analysis, we applied selection requirements on the `autoscan` score and `SExtractor` detection flag. Both of these programs run at the image level, so their information is not present in `SNANA`-simulated light curves. We adopt the empirical approach from *Doctor et al.* (2017) to determine realistic values for `autoscan` and `SExtractor` quantities in the simulations. This process involves inserting simulated point source objects of known brightness (hereafter "fakes") into the real DECam images, and applying our image processing pipeline to the images to record the `autoscan` score and `SExtractor` detection flag. From the processed fake objects, we extract the probability mass functions (pmfs) for the `autoscan` score and `SExtractor` detection flag at discrete levels of signal-to-noise ratio ranging from

0.5 to 50.0. Each filter is treated independently when extracting the pmfs. In the process of generating simulations, based on the signal-to-noise ratio of each observation, values for the `autoscan` score and `SExtractor` detection flag are drawn from the corresponding empirically-derived pmf. We also introduce a reduced correlation coefficient of 0.1 to the drawn `autoscan` scores for observations of the same object, determined so that the simulations accurately reflect the fake data.

Level 2 of our selection criteria rules out known objects by matching to the DES Y3 Gold Catalog. When matching to DES stars, globular clusters NGC288, and the star HD4398, we estimate the sky area masked by our criteria using a Monte-Carlo sampling of position space. We find that a $0.5''$ radius around DES stars masks 0.11 percent of the sky area covered in our follow-up observations, and an $8'$ radius around NGC288 and a $3'$ radius around HD4398 each mask 0.01 percent. In the simulations, we use these percentages of the sky masked by these selection criteria as the probability for a simulated object to be removed by the criterion.

We take a slightly different approach to modeling the criterion of removing known galactic centers from our sample since these objects are not in the foreground of our observations. Here we model the transient-galaxy separation empirically and impute that separation into the simulations. We extract a probability distribution function of SN-host galaxy center separation in units of physical distance from the DES 3-year spectroscopic SNe sample (*DES Collaboration*, 2018). This sample is dominated by SN-Ia for cosmological analyses, which makes it more applicable to KN-host galaxy separation than a balanced SNe sample: the progenitors of SN-Ia are thought to be white dwarf stars in binary systems (*Woosley and Weaver*, 1986; *Hillebrandt and*

Niemeyer, 2000; *Maoz et al.*, 2014), meaning to first order they would be similar in age and hence host separation to other binary systems of stellar remnants (*Bloom et al.*, 2006; *Prochaska et al.*, 2006). We believe this assumption to be conservative, given that supernova (or sometimes called "prenatal") kicks during the evolution of binary massive star systems into BNS or NSBH systems are expected to cause an increase in the separation from the host-galaxy center (*Stairs et al.*, 2006). We therefore apply the same transient-galaxy separation pdf to both the KNe and SNe simulations. In the application of the selection criterion, we draw a separation from the pdf and remove the object if the separation is less than $0.2''$. When testing this criterion on the DES 3-year SNe sample, we estimate 97% of transients will be recovered while effectively removing all time-varying galactic centers.

Our real-time candidate reduction also relied on visual inspection of the images to remove artifacts and point-like light sources without a host galaxy. We assume near perfect efficiency in the simulations with one exception stemming from the fact that this criterion has a dependence on the seeing of the observations. A bright galaxy center in poor seeing conditions can hide real transients in the image or appear like a point source itself, resulting in it being removed from the sample. For the simulations, if the imputed host separation is less than half of the seeing, we reject the simulated object.

The final pieces of additional information that were necessary to add to the `SNANA` simulations were photometric redshifts and photometric redshift errors. Here we take the i-band galaxy magnitudes of all galaxies in the DES Y3 Gold catalog also in the LVC 90% containment region to empirically determine the i-band magnitude pdf in

several redshift bins. Using the true simulated redshift of our SNe and KNe, we select the corresponding host galaxy i-band magnitude pdf and draw a random value. With a chosen i-band host magnitude, we determine the expected value of the photometric redshift error from the validation of the Gold catalog. We define a Gaussian distribution centered on the true simulated redshift with a standard deviation of the photometric redshift error. We account for known underestimations of low redshift galaxies' photometric redshift uncertainty using the same treatment discussed in Section 4.2.3. Thus, after drawing a photometric redshift from this distribution, each simulated transient will have a photometric redshift and photometric redshift error to match the candidates in our observations.

We model spectroscopic targeting and classification by implementing the ratio of the number of objects targeted by spectroscopic instruments to the number of candidates remaining at that stage in the follow-up as the probability of an SN being rejected.

4.4.3 Sensitivity Results

Here we present the results of applying our real-time selection criteria to `SNANA`-simulated SNe and KNe light curves. We stress that this approach of representing the expected signal and background samples by applying selection criteria to the light curves provides our best understanding of the characteristics of the objects present in the final candidate sample. We use our simulated light curves to quantify the expected number of remaining SNe in the final candidate sample, to determine the detection efficiencies of all available KN models, to understand the light curves of

objects passing our selection criteria, to place upper limits on the physical properties of the merger, and to forecast our discovery potential in future follow-up observations. In Section 4.5, we use all these pieces of information to inform a discussion of efficient follow-up strategy and on the dynamics of the merger.

Table 4.2 lists the number of candidates surviving each criterion enforced during our real-time analysis. We also show that the number of candidates remaining after all selection criteria is consistent with the expected background SNe in these follow-up observations. The ML classification of our candidates found no potential KNe remaining in our final sample. Furthermore, because the `PSNID+FRC` classifier performed with a false-positive-rate of 0.01, a remaining candidate would be identified as a KN at the 3σ confidence level. This low false-positive rate of the classifier effectively reduces the SNe background to zero objects, which will prove to be essential for claiming an association between a GW signal and a candidate counterpart in subsequent optical follow-up observations.

A second result of this analysis is the detection efficiency of 329 independent KN models as they would appear in our DECam observations. Figure 4.4 shows the efficiency of each model after Criterion 1 was placed. Criterion 1, which requires a single Type-1 detection, can be thought of as assuring the maximum brightness of the objects is greater than the 5σ limiting magnitude of the observations. Efficiencies after all criteria up to the ML classification and efficiencies after the ML classification occurs can be found in Figure 4 of *Morgan et al.* (2020). The blue and red boxes in the panels identify the best-fit model components of the emission from AT2017gfo (*Drout et al.*, 2017; *Kilpatrick et al.*, 2017), the optical counterpart for GW170817, at

distances consistent with GW190814 and accounting for the environmental conditions of our follow-up observations. We find that low M_{ej} and high X_{lan} yield an optical signature that would be difficult to detect in our DECam observations. At the same time, we note that our selection criteria limit our ability to detect KNe models with low v_{ej} and high M_{ej}. Physically, the light curves of these models fade more slowly than other KN models and are more similar to some SN models, which leads to class confusion at the ML stage.

A third product of this analysis is a prediction of the average light curves of the objects that pass our selection criteria. In Figure 4.5, we overlay the measured i-band magnitudes of our candidates on the average light curves of simulated objects passing the same selection criteria. In the top row, we consider our candidates in the context of SNe. The high redshift SNe pass our selection criteria because their photometric host-galaxy redshift and uncertainty are consistent with the LVC distance posterior at the 3σ level. As shown in Figure 4.5, these high-redshift SNe very closely resemble our candidates in terms of light curve properties: the fading rates of the light curves over the 16 nights and the apparent magnitudes are quite similar. The bottom panel compares our candidates to KN models. Each KN light curve is the average across the full range of X_{lan}, since this parameter was found to have the smallest effect on light curve shape–it does however affect the color, but we only show monochromatic light curves in the figure. This averaging is subject to the non-uniform grid of models and the parameterization of X_{lan} in log space, however, we reiterate that this parameter has the smallest effect on the light curve shapes shown in the figure.

The KN models as a class fade much more quickly than our candidates, which

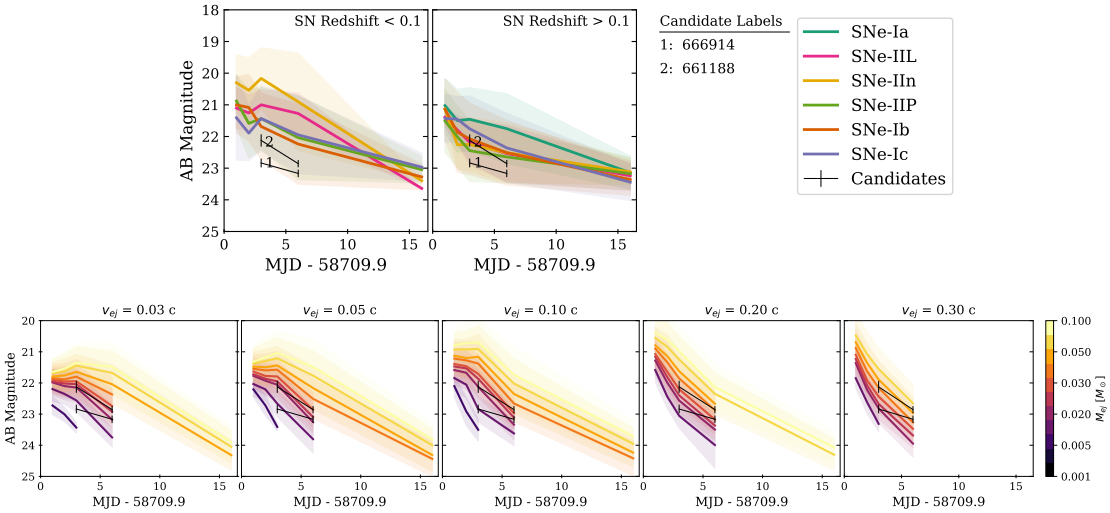

Figure 4.5 Light curves (i-band) of objects passing the selection criteria. All light curves are simulated and averaged to determine the mean light curve and 1σ confidence level contours. For the simulated SNe, $z = 0.1$ is used as the cutoff between low and high redshift. Other classes of SNe did not pass the selection criteria with high enough frequency to be accurately represented in the figure. Simulated KNe light curves averaged over X_{lan} are shown in the bottom panel. Our candidates passing criteria 1-9 are overlaid for qualitative assessment.

results in many of them becoming too faint to detect in our observations 16 nights after the merger. An understanding of the light curves for a potential KN and the expected background is essential for choosing an efficient observing strategy, which we will discuss in Section 4.5. We note again that KN light curves from models with low v_{ej} and high M_{ej} fade the slowest out of all KN models, and at a rate comparable to the faster-fading SN models in the top panel of Figure 4.5. This observation only applies to optical emission in the i and z filters, and we are unable to speculate on the generalization of this behavior to other wavelength ranges. This behavior of this subset of KN models poses the greatest confusion to our ML classifier as a result of

the light curve similarities.

Using the fact that a KN was not detected in these observations, we can translate our KN detection efficiencies and expected background rates into upper limits on merger properties. We estimate the properties of a KN that would go undetected from a Bayesian standpoint:

$$P(\mathrm{KN}_i|n_{\mathrm{cand}}) = \frac{P(n_{\mathrm{cand}}|\mathrm{KN}_i) \times P(\mathrm{KN}_i)}{P(n_{\mathrm{cand}})}. \tag{4.2}$$

In Equation 4.2, KN_i refers to an individual KN model and n_{cand} is the number of candidates detected in the observations. In this analysis, $n_{\mathrm{cand}} = 0$, though we present the generalized formalism. The likelihood in Equation 4.2 can be explicitly written as

$$\begin{aligned} P(n_{\mathrm{cand}}|\mathrm{KN_i}) = \quad & \varepsilon_i \times \mathrm{Poisson}(n_{\mathrm{cand}} - 1|B) \quad + \\ & (1 - \varepsilon_i) \times \mathrm{Poisson}(n_{\mathrm{cand}}|B), \end{aligned} \tag{4.3}$$

where ε_i represents the detection efficiency of KN_i and B represents the expected SN background, both of which are determined after all selection criteria have been applied. The Poisson distribution used in Equation 4.3 has an expectation value of B objects and yields the probability of detecting $n_{\mathrm{cand}} - 1$ or n_{cand} objects. This formulation is motivated by summing the probability that a KN is detected and the remainder of the candidates are a realization of the predicted SN background with the probability that a KN is not detected and all detected candidates are a realization of the predicted SN background. In Equation 4.2, $P(\mathrm{KN_i})$ is the prior distribution of KN models, which we make uninformative by assigning equal probability to each model

in the non-uniform grid. The denominator can be evaluated directly by computing

$$P(n_{\rm cand}) = \sum_{i \in {\rm KNmodels}} P(n_{\rm cand}|{\rm KN_i}) \times {\rm P(KN_i)}, \tag{4.4}$$

which can be interpreted as a probability normalization constant. Thus, the posterior distribution of KN models given the non-detection in this analysis can be estimated by setting $n_{\rm cand} = 0$ and sampling the likelihood space. The results of this sampling are displayed in Figure 4.6.

From these observations and sensitivity analysis, we report our constraints on candidate counterpart ejecta properties in Table 4.3. To determine the likelihood of a physical KN parameter rather than an individual model in our non-uniform model grid, we perform a three-dimensional linear interpolation between the model efficiencies in the space of $\log(X_{lan})$, M_{ej}, and v_{ej}. We note that this linear interpolation is justified by the smoothness of adjacent points in the grid of efficiencies in Figure 4.4. These results are less constraining than what would be obtained using the KN efficiencies and expected backgrounds after Criterion 1, but this is only the case when $n_{\rm cand} = 0$. In this specific case the first term in Equation 4.3 is zero, which leads to a cancellation of the background in Equation 4.2, so the effect of the selection criteria only manifests through reducing KN detection efficiencies. In general, reducing the SN background will produce better constraints.

It is worth noting here that previous analyses have demonstrated that derived constraints can depend on the models employed in the analysis (*Coughlin et al.*, 2019), and furthermore that the discretized grid of model parameters can affect the

Table 4.3 Constraints on counterpart ejecta properties of the candidate NSBH merger GW190814. These constraints are derived by interpolating the grid of efficiencies in Figure 4.4 for each of the *Kasen et al.* (2017) KN models and applying the Bayesian formalism presented in Section 4.4.3. This calculation utilized an uninformative prior by assigning equal probability to each point in the KN ejecta parameter space.

Ejecta Property	1σ Constraint	2σ Constraint
M_{ej}	$< 0.016\ M_{\odot}$	$< 0.07\ M_{\odot}$
v_{ej}	$\notin [0.16c, 0.26c]$	$\notin [0.18c, 0.21c]$
X_{lan}	$> 10^{-5.92}$	$> 10^{-8.56}$

constraints as well (*Dietrich et al.*, 2020). For this specific event, optical light would be emitted by tidally-stripped NS material, which motivated our choice of models focused on the ejecta properties. By not using a model tied to the dynamics of the system, we marginalize over the dependencies on these features of the merger and focus our analysis on directly observable characteristics. To account for the non-uniform spacing of our grid of model parameters, we performed a three-dimensional linear interpolation of the efficiencies in Figure 4.4 when performing the Bayesian analysis. In the Bayesian analysis, we assigned an equal probability to each point in the parameter space of our models. While not all ejecta parameter combinations may be equally likely given the NSBH-nature of GW190814, we believe our uniformed prior is well-motivated given the mass of the lighter object involved in the merger. In the event that the object truly was a 2.6 $M_{\odot}$ NS, we believe all values in the ranges of M_{ej}, v_{ej}, and X_{lan} are physically accessible under the right dynamical conditions.

To show the benefit of selection criteria that reduce the SN background in GW follow-up observations, we perform simulations of follow-up observations at several points in this analysis. After each criterion, we take the expected SN background

and KN detection efficiency for the blue component of a GW170817-like KN, and calculate the significance level at which that KN would be identified as the counterpart. Assuming a nearly complete coverage of the GW alert localization area, we report the fraction of follow-up observations where an association at the 1σ, 2σ, 3σ, and 4σ confidence level would be possible in Figure 4.7 as functions of the remaining SN background. Without placing any selection criteria, less than 3% of DECam follow-up observations can be expected to identify the counterpart at the 3σ confidence level. Conversely, with the selection criteria and ML classification developed in this analysis, approximately 95% of follow-up observations are expected to be able to identify a counterpart in the DECam observations at the 4σ confidence level.

4.5 Discussion

Our optical follow-up observations of the first candidate NSBH merger GW190814, simulations of transients in the localization area, and accompanying sensitivity analysis serve as powerful tools moving the field of multimessenger astronomy forward. In this analysis, we presented several key results: the quantification of the expected background, the development of tailored selection criteria, an understanding of KNe efficiency in the observations, an understanding of the light curves of objects in our final candidate sample, upper limits on KN counterpart properties, and the forecasting of our discovery potential using the methods developed here. In this section, we first compare our results to previous analyses of this merger, and then we utilize our results to inform a discussion of merger dynamics and efficient follow-up strategy.

4.5.1 Comparisons to Previous Analyses

In this subsection, we highlight the differences between our approach and those presented in other analyses and follow-up observations of GW190814. While GROWTH (*Andreoni et al.*, 2020, henceforth G20) analyzed the public DECam observations discussed in this work, multiple teams performed independent observations. *Vieira et al.* (2020) (henceforth V20) observed GW190814 using MegaCam / CHFT. The V20 observations utilized the g, i, and z bands reaching 5σ limiting magnitudes of $\sim$ 23 mag on nights 1, 2, 3, 4, 6, 7, 8, and 20 following the merger. The imaging covered 69% of the total integrated probability area, as the 1 sq. degree FoV of the imager limited the feasible area to cover each night. the Very Large Telescope (*Ackley et al.*, 2020, henceforth E20) utilized several observatories and filters to image the 90% localization area including the Gravitational wave Optical Transient Observer, the Visible and Infrared Survey Telescope for Astronomy, the Very Large Telescope, the Asteroid Terrestrial-impact Last Alert System, and Pan-STARRS1. They reach limiting magnitudes comparable to DECam on a significant fraction of the localization area and distribute a cadence similar to the DECam and MegaCam cadences across their network of observatories. *Gomez et al.* (2019) (henceforth M20) performed a galaxy-targeted search within the 50% localization area on nights 1 and 2 following the merger with the Magellan Baade telescope. They reach a 3σ i-band limiting magnitude of 22.2 mag. Lastly, *Watson et al.* (2020) (henceforth W20) utilized the DDOTI wide-field robotic imager on the first two nights covering the merger. They cover the full localization area to $\sim$ 18 mag in the $w = r + 0.23(g - r)$ band.

The characteristics of the different datasets collected, such as imaging depth, observing cadence, sky area covered, and image quality shaped the analyses performed by the counterpart search teams. W20 was able to detect transients to ~ 18 mag, meaning KN-like optical signatures at the distance of GW190814 would be too faint to detect. For this reason, they are unable to place constraints on counterpart properties that are competitive with the groups employing deeper optical imaging. M20 obtained deep imaging, but only targeted galaxies with the 50% localization area (70% of the galaxy-weighted probability). While they calculate that KN-like counterparts with more than 0.03 $M_{\odot}$ would be too faint to detect in their observations, without covering the full 90% localization area, they cannot place constraints above the 90% confidence level. We, G20, V20, and E20 covered high fractions of the 90% localization area and utilized telescopes and images powerful enough to detect potential counterparts at the distance of GW190814.

No group reports an EM counterpart, and G20, V20, and E20 use their observations to place constraints on the properties of the merger. G20 fixes the distance of the merger to the mean value of 267 Mpc and finds $M_{ej} > 0.05\ M_{\odot}$. They also consider the viewing angle of the merger in their constraints, which enters into our analysis through the line-of-sight component of the ejecta velocity. V20 finds slightly tighter constraints on the ejecta mass of a potential EM counterpart (0.015 $M_{\odot}$), though their analysis fixes v_{ej} to $0.2c$, which we show in this work is disfavored at the 2σ confidence level. We suggest this choice of disfavored ejecta velocity is the cause of the comparatively tighter constraints reported by V20. E20 reports that KN-like counterparts with $M_{ej} > 0.1\ M_{\odot}$ are excluded at the 90% confidence level.

They arrive at this result by using the limiting magnitudes of their observations and the expected magnitudes of KN models (similar to the work of G20 and V20) at the distances distributed according to the luminosity distance posterior of GW190814 from the LVC (similar to this work).

The characteristic distinguishing the work presented here from the analyses of all other groups is the extent of the sensitivity analysis used to understand KN detection efficiencies in the observations. G20 and V20 choose a handful of representative fixed distances for the KN and assess whether the apparent magnitude of a particular model would be brighter than the 5σ magnitude limit in the band of the observations. This approach does not consider the effect of the selection criteria applied to the candidates to rule out all objects on the KN model efficiencies, nor does it accurately marginalize over the LVC distance posterior for the merger. The simulations developed for our work fully incorporate the effects of our real-time selection criteria, the full posterior of luminosity distances, and enable us to place meaningful constraints without fixing any KN parameters. Understanding the effects of the selection criteria placed during a real-time search on the set of detectable counterpart configurations is essential for accurately constraining the physical properties of the potential optical counterpart. The approach demonstrated in this work has been used in *Doctor et al.* (2017), *Morgan et al.* (2019), *De et al.* (2020), *Kasliwal et al.* (2020), and *Garcia et al.* (2020), and has been facilitated by the development of code bases such as `simsurvey` (*Feindt et al.*, 2019). We advise that future analyses employ this approach in GW counterpart searches and population studies.

4.5.2 Merger Dynamics

The optical signature from an NSBH merger is highly dependent on the dynamics of the system and the characteristics of the compact objects involved (*Rosswog*, 2013; *Bauswein et al.*, 2013; *Radice et al.*, 2017, 2018). For a KN-like signature to be emitted, the NS would need to be tidally disrupted to produce light-emitting ejecta. Therefore, the spins and masses of the coalescing bodies, which determine the degree of tidal disruption of the NS, are intimately linked to the optical signature (*Capano et al.*, 2020).

At the 2σ confidence level, we were able to exclude counterparts with $M_{ej} > 0.07\ M_{\odot}$. Thus, only a small fraction of the NS material was ejected. We also exclude counterparts with $X_{lan} < 10^{-8.56}$ at the 2σ level. The constraint on this quantity is $10^{-5.92}$ at the 1σ level, indicating that higher X_{lan} are favored overall, and that in the most probable case, any ejecta produced would have been rich in heavy elements. This richness could result from the small (if any) amount of NS material ejected in the merger, as the majority of the material would be synthesized into heavy elements by the gravitational potential in close proximity to the BH. A final result from this sensitivity analysis that can be used to infer properties of the merger is the non-detection of a KN-like counterpart. Since our KN detection efficiency decreases with M_{ej}, the lack of an observation of a KN in this merger event suggests a small or nonexistent amount of ejected material. The DECam observations are therefore consistent with the NS retaining structural integrity until it passed the radius of the last stable circular orbit.

The physical parameters of the merger most closely tied to the potential tidal

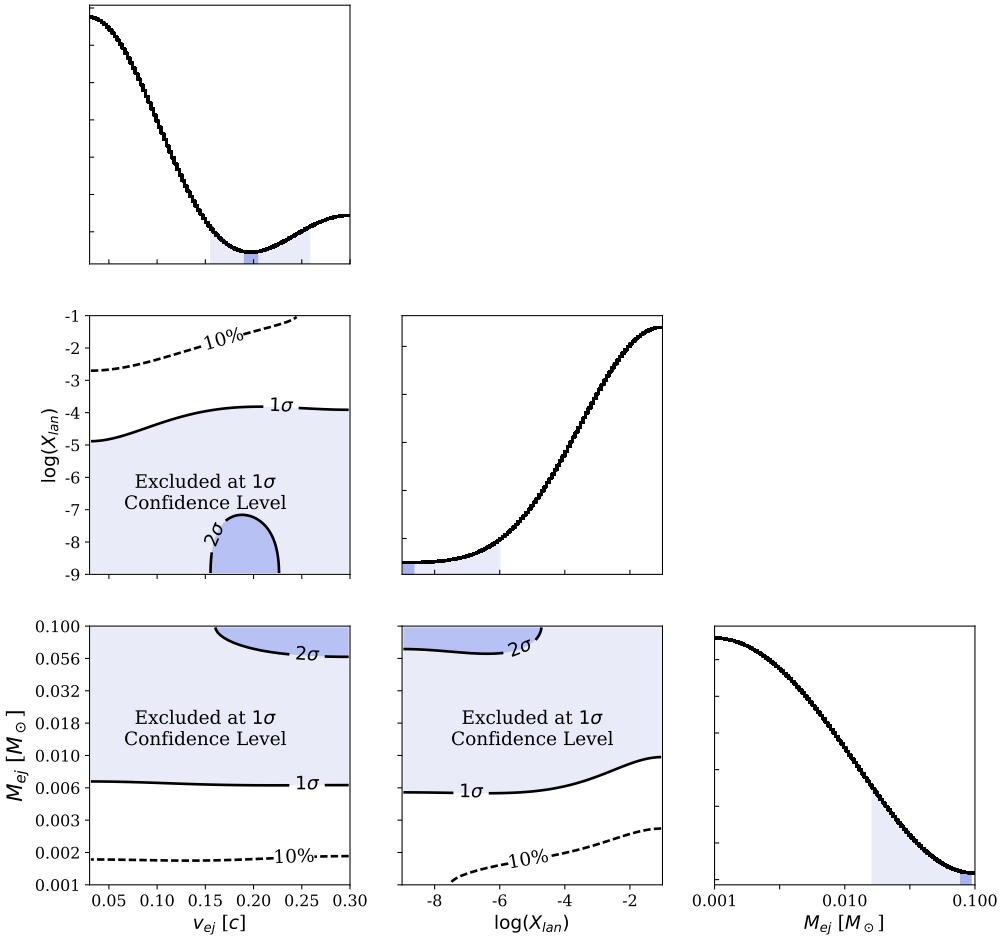

Figure 4.6 Exclusion contours in the ejecta mass (M_{ej}), velocity (v_{ej}), and lanthanide fraction (X_{lan}) parameter space at the 1σ and 2σ levels. The posterior distributions of the three parameters are shown as histograms in the rightmost plot of each row.

disruption of the NS, and hence the optical constraints derived in this analysis, are the mass ratio $q \equiv M_{BH}/M_{NS}$, the magnitude of the final BH spin χ, the radius of the neutron star r_{ns}, and the chirp mass $\mathcal{M}$. The ejected mass increases with decreasing M_{BH}, increasing χ, and r_{ns} (harder EOS). From numerical simulations, the upper limit to disk formation is a mass ratio of $\sim 3-5$ (*Lattimer*, 2019; *Pannarale and Ohme*, 2014; *Foucart et al.*, 2019, 2018). For a fixed BH mass, as the NS mass increases, a larger BH spin is required to produce a massive disk. The reason is that higher black hole spin decreases the last stable circular orbit radius, allowing a higher mass NS, generally more compact, to reach its disruption radius and thus leave the disrupted NS matter remaining in orbit. Holding the NS mass fixed, increasing the BH mass increases the gravitational radii, and higher spins are needed to bring the last circular orbit radius in below the disruption radius. Binaries with low mass ratios and high BH spins maximize the chance of massive disk formation. Based on our observations, the spins, masses, and alignments of the merging bodies disfavor tidal disruption of the NS. In their recently released parameter estimation of the merger, the LVC determined $q = 0.11$, $\chi = 0.28$ of 0.28, and $\mathcal{M} = 6.1\ M_{\odot}$ (*Abbott et al.*, 2020b). This spin and mass ratio would lead to small amounts of tidal disruption of the NS, and would be consistent with the lack of an accretion disk, the lack of an accompanying gamma-ray burst, and the lack of a detection of a KN-like counterpart. Therefore, the constraints on NS ejecta properties derived from the DECam observations in this analysis are consistent with the LVC parameter estimation of the merger dynamics.

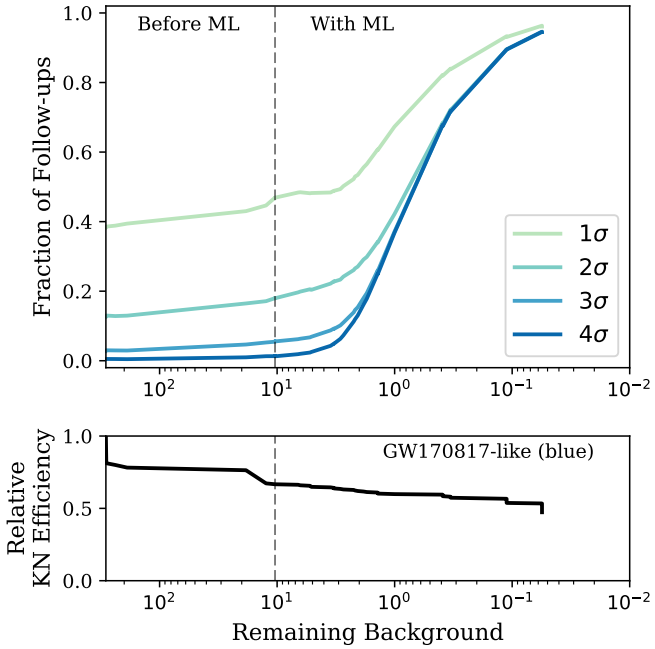

Figure 4.7 The effect of applying selection criteria on follow-up observation sensitivity and KN efficiency. *Top:* The fraction of follow-up observations expected to result in a KN detection of given significance as a function of the remaining background. *Bottom:* Efficiency for the blue component of a GW170817-like KN at the distance of GW190814 as a function of the remaining background.

4.5.3 Implications for Follow-up Observation Strategy

We find two aspects of our observing strategy for this event to be highly efficient and recommend their use in follow-up observations going forward. Namely, our observing cadence and exposure time, and specifically how we tailored them to the conditions of the event, were essential in detecting the large number of candidates published by teams using the public DECam data.

The cadence of our observations was well-suited for the detection of a KN-like optical signal. By triggering DECam immediately after the LVC alert, and by repeating

observations on the next three nights following the merger, we increased our chances of detecting a rapidly changing object. Furthermore, our choice to include epochs on nights 6 and 16 after the merger enabled the characterization of light curves for longer-lived transient objects in that part of the sky. This choice proved to be essential in systematically eliminating fading objects unassociated with the GW signal. While a KN is not expected to be bright at these later epochs, the detection of any potential candidate on these nights can be used as evidence to exclude the object.

In this sensitivity analysis, the availability of light curves spanning a 16 day interval with 6 observing epochs enabled the development of a powerful ML-based photometric classifier. Our `PSNID + RFC` approach was able to effectively eradicate the SN background in these observations, and we expect a similar performance in subsequent follow-up observations with similar cadences. The benefit of devoting resources to background reduction is a key point we seek to make. Figure 4.7 demonstrates how reducing the SN background dramatically increases the probability that optical follow-up observations will associate a candidate with the LVC alert at a statistically significant confidence level. In this figure, we select a single KN model for simplicity and consider its detection efficiency as a function of the remaining SNe background as we apply the selection criteria in this analysis. The "Before ML" section references the real-time selection criteria of this analysis while the "With ML" section varies the `PSNID + RFC` operating threshold to move along the ROC curve of Figure 4.3 towards regions of higher purity. Again, the performance of this classifier and the possibility to reduce the SN background are primarily determined by the cadence chosen by the observing team. Reducing the SNe background using

the techniques of this work leads to the possibility of associating a detected transient with the merger at the 4σ confidence level 95% of the time in identical follow-up observations.

The exposure time of the DECam images was dynamically varied in response to changing observing conditions. On the first two nights, when a potential KN-like counterpart would be expected to be near peak brightness, we opted for a shorter exposure time to tile the area twice quickly. This choice enabled us to rule out moving objects while maintaining enough depth to detect a KN-like object positioned at the estimated distance of GW190814. In subsequent nights, we increased the exposure time such that we would be sensitive to fainter objects since a KN-like object would be expected to fade by ~ 0.5 mag per day (*Kasen et al.*, 2017). While the choice to vary the exposure time introduces non-uniformity in the image quality of the DECam data, it is useful for maximizing the probability of detecting a rapidly-fading transient on each night of observation. Furthermore, we note that this variance of image quality over the course of the observations necessitates the use of detailed simulations of the follow-up observations for quantifying constraints. Our choice of exposure times resulted in the deepest optical observations of the entire 90% localization region on each night DECam was operated compared to all follow-up teams. Thus, the observing strategy described in this work is a useful baseline for future DECam follow-up observations.

The chances of detecting a potential counterpart were greatly improved by SOAR spectra being obtained for the most interesting candidates. While we were able to achieve high accuracy machine-learning-based photometric classification of the ob-

jects in our sample in this work, the success of that approach requires the availability of several nights of photometric observations. In the real-time portion of the observations, the spectroscopic component of the search is essential. The use of SOAR enabled us to confidently exclude $\sim 20\%$ of our most promising candidates on the first few nights of the observations.

We see this spectroscopic efficiency as an aspect of gravitational wave counterpart identification that can be dramatically improved given the resources of the astronomical community, for example with the use of wide–field multi–object spectroscopy (*Palmese et al.*, 2019). In cases where the 90% localization is larger than what one telescope can cover in a single night, the fraction of sky area covered by the astronomical community is another improvable trait of the follow-up strategy. As we look forward to the increased sensitivity in Observing Run 4 and consequent increased alert frequency, synergy among follow-up teams will be integral to the association of gravitational waves with their electromagnetic counterparts. Distributed and coordinated observations among follow-up teams will be essential, and furthermore the sharing of observation metadata to improve sensitivity and forecasting studies will benefit the field as a whole. For further discussion of these topics, see *Coughlin* (2020)

4.6 Conclusion

In response to the first high confidence alert of gravitational radiation from a neutron star–black hole merger GW190814, we triggered the 4m Blanco Telescope / Dark Energy Camera and obtained the deepest coverage of the entire 90% localiza-

tion area. Our observations took place on 6 nights over the first 16 nights following the merger, and each night the Dark Energy Survey Gravitational Wave Search and Discovery Team published candidate counterpart objects to the astronomical community (*Soares-Santos et al.*, 2019a; *Palmese et al.*, 2019; *Herner et al.*, 2019b; *Tucker et al.*, 2019b; *Herner et al.*, 2019c; *Rodriguez et al.*, 2019; *Soares-Santos et al.*, 2019c,d; *Annis et al.*, 2019; *Palmese et al.*, 2019; *Tucker et al.*, 2019a; *Soares-Santos et al.*, 2019b; *Herner et al.*, 2019a; *Wiesner et al.*, 2019a,b; *Cartier et al.*, 2019). The entire localization area was within the Dark Energy Survey footprint, enabling the use of six years of previous images and complete host galaxy catalogs in our search for a counterpart. In an offline analysis following the conclusion of observations, all candidates were excluded based on light curve properties, photometric redshifts of the host galaxies, or a machine-learning classification approach developed specifically for this work. We present the results of the real-time follow-up observations and accompanying sensitivity analysis here. Using detailed simulations of supernovae and kilonovae matched to our observing cadence and conditions, we quantify the expected supernova background, develop selection criteria that effectively remove that background, and calculate kilonova efficiency resulting from the selection criteria. The non-detection of an electromagnetic counterpart in our data implies that a potential counterpart had $M_{ej} < 0.07\ M_{\odot}$, $v_{ej} < 0.18c$ or $v_{ej} > 0.21c$, and $X_{lan} > 10^{-8.56}$ at the 2σ confidence level. These analysis components enabled us to also characterize the typical light curves of supernovae and kilonovae that would appear in our observations, set constraints on the properties of an undetected kilonova, and forecast the sensitivity of follow-up observations like this one going forward. We utilize these re-

sults to inform a discussion of the dynamics of the merger and efficient gravitational wave follow-up strategy.

CHAPTER V

The Observing Strategy Revisited[1]

The third LIGO/Virgo Collaboration (LVC) observing run (O3) resulted in over 60 new events (see the third Gravitational-wave Transient Catalog, *The LIGO Scientific Collaboration et al.* (2021), hereafter GWTC-3). One GW event originated from a BNS merger and two high-confidence events originated from NSBH coalescences (*Abbott et al.*, 2021), but no electromagnetic counterparts were confirmed from any event despite extensive follow-up campaigns (e.g., *Morgan et al.*, 2020; *Garcia et al.*, 2020; *Tucker et al.*, 2022; *Kilpatrick et al.*, 2021; *Oates et al.*, 2021; *Andreoni et al.*, 2019; *Andreoni et al.*, 2019b; *Goldstein et al.*, 2019). One study (*Graham et al.*, 2020) proposed an AGN counterpart to the binary black hole merger GW190521, but the association to the GW event cannot be made with confidence (*Palmese et al.*, 2021).

The fourth GW observing campaign (O4) started in May 2023 and is ongoing at the time of this writing. In O4, the Japanese GW antenna, KAGRA, is joining the LVC to form the LIGO/Virgo/KAGRA (LVK) Collaboration. In O4, the LVK

[1]This Chapter is published as *Bom et al.* (2023), arXiv:2302.04878 (submitted to the Astrophysical Journal)

is expected to achieve a median Luminosity Distance that is two times larger and a factor of ~ 7 detections of BNS events than the previous O3 campaign (see table 2 in *Petrov et al.*, 2022). The expected rates of BNS are uncertain but in the range of 9-88/year (*Abbott et al.*, 2020a; *Petrov et al.*, 2022). It is unlikely that each subsequent KN event will obtain the same amount of follow-up resources as in O3. As GW detectors become more sensitive and able to detect events at larger distances, the optical follow-up of BNS events will become more challenging, including for campaigns using the Dark Energy Camera (DECam, *Flaugher et al.*, 2015) such as those coordinated by the DES Gravitational Wave follow-up group (DESGW). With this challenge in mind, we performed a detailed study to optimize the search strategy for O4.

5.1 Simulation data

5.1.1 Simulated O4 BNS events

We start by producing a set of simulated BNS mergers that are expected to be detectable in the upcoming LVK O4 observing run. The procedure is similar to that in *Petrov et al.* (2022).

GW events are simulated using the `BAYESTAR` software (*Singer and Price*, 2016; *Singer et al.*, 2016a,b), which uses `LALSuite` (*LIGO Scientific Collaboration*, 2018) tools. We assume sensitivity curves for Advanced LIGO, Virgo, and KAGRA as O4 sensitivities discussed in *Abbott et al.* (2020a)[2], though we assume a sensitivity for

[2]The curves are available in `https://dcc.ligo.org/LIGO-T2000012/public` and, `https://dcc.ligo.org/LIGO-T2000012-v1/public`

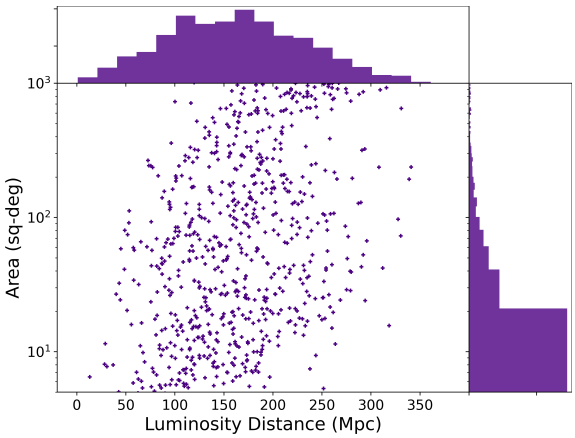

Figure 5.1 The distance distribution and 90% credible interval sky localization area of the O4 simulations of BNS mergers used in this study. The simulated primary masses follow a $\bar{x} = 1.5M_\odot$, $\sigma = 1.1M_\odot$, $x_{\rm min} = 1.1M_\odot$, $x_{\rm max} = 3M_\odot$ Gaussian distribution, and the spins of the events are distributed uniformly between ± 0.05. Simulated detections are limited to events with a network SNR greater than 12. In this work, we use only events with area < 300 degrees^2, which is 611 of the 860 events.

KAGRA of a BNS range of ~ 80 Mpc.[3] All detectors have a duty cycle of 70%, which is consistent with LVK predictions *Abbott et al.* (2018). Assuming a *Planck Collaboration et al.* (2020) cosmology, we create $10,000$ BNS events of the type O4 could theoretically observe, following a uniform in comoving volume distribution. TaylorF2 waveforms (*Buonanno et al.*, 2009) are assumed both for injections and reconstructions. The primary mass distribution of our injections follow the neutron star mass function found in *Abbott et al.* (2021), normally distributed with mean 1.5 $M_\odot$ and standard deviation 1.1 $M_\odot$, truncated to be within $1.1M_\odot \leq M_{\rm NS} \leq 3M_\odot$ in order to stay consistent with the Kasen models' parameter space. The NS spin distribution was uniformly distributed between -0.05 and 0.05. After injecting the

[3]LVK has updated the assumed sensitivity for KAGRA, as seen in v2 of the above table; this makes little difference to our analysis, concerned mostly with distant events

BNS mergers, a matched-filter search retrieves the detected events. We consider as detections those events for which a single–detector signal–to–noise ratio SNR>4 is reached by at least 2 detectors and the overall network SNR is >12, resulting in 860 detected events. The measured SNR is added with Gaussian noise. Finally, we produce `BAYESTAR` skymaps for the detected events. In Figure 5.1 we present the area (90% credible interval) and luminosity distance (integrated over the whole sky) for all of the simulations used in this analysis.

Petrov et al. (2022) argues that the alerts produced by the LVC during O3 are better modeled by dropping the two detector coincident detection requirement and using a minimum SNR for BNS events of >8. These criteria would have the effect of increasing the number of low SN, and therefore large sky area, events in our simulations. Figure 5.1 shows median luminosity distance of ~ 150 Mpc and sky area of ~ 20 sq-degrees, whereas *Petrov et al.* (2022) find 352 ± 10 Mpc and 1820^{+190}_{-170} sq-degrees, a difference from previous work that they attribute to the changing of the SNR requirements. There are 249 from the total of 860 events that have 90% sky area >300 sq-degrees. To change our sample to have a median sky area of ~ 350 sq-degrees we would need an additional ≈ 360 events, all of which would need 90% sky area >350 sq-degrees. Later we will be placing a sky area limit of <300 sq-degrees, so we chose not to consider these additional high-sky-area events here.

5.1.2 Kilonova physical models

We model KN using the time-evolving theoretical Spectra Energy Distributions (SEDs) of KN atmospheres from *Kasen et al.* (2017), hereafter referred to as the

Kasen models. The Kasen models are parameterized by the mass ejected in the explosion, $M_{\rm ej}$, the abundance of lanthanide elements in the ejecta, $X_{\rm lan}$, and the velocity of the ejecta, $v_{\rm ej}$. The models are a set of 329 time-dependent SEDs on a grid of discretized parameters: $0.001\ {\rm M}_\odot \leqslant M_{\rm ej} \leqslant 0.1\ {\rm M}_\odot$, $0.03c \leqslant v_{\rm ej} \leqslant 0.3c$, and $1 \times 10^{-9} \leqslant X_{\rm lan} \leqslant 1 \times 10^{-1}$.

There are other KN models available in the literature (e.g. *Bulla*, 2019; *Darbha and Kasen*, 2020; *Hotokezaka and Nakar*, 2020; *Wollaeger et al.*, 2021; *Gillanders et al.*, 2022). In comparison to these, the Kasen models do not build in the dependence on the geometry of the mergers and the viewing angle (see, e.g., *Stewart et al.* 2022 for a visualization of an asymmetric KN supported by accretion disk simulations), but instead provide atmosphere models to be used in building a geometric model. While the viewing angle is an important parameter for the expected light curve, we argue that the range of light curves built within our framework covers the full parameter space of expected light curves. This is discussed further in 5.3.2.

5.2 Kilonova lightcurve simulations

The lightcurve simulation pipeline is similar to that used in *Morgan et al.* (2020), which constrains the physical KN properties of GW190814. The SuperNova ANAlysis software (SNANA: *Kessler et al.* 2009, 2019b) enables the simulation of light curves of KN as they would be measured by DECam. SNANA produces light curves by simulating fluxes and uncertainties in observations by incorporating information about cadence, image zero points, and noise levels in search and template images. The light curves are in absolute magnitudes and are converted to observed magni-

tudes using a given cosmology. In particular, SNANA chooses a grid of 15 redshifts at $0.003 \leqslant z \leqslant 0.2$, which is used to transform the Kasen model SEDs without evolution. The Kasen model SED is redshifted to a z on our grid. SNANA also takes into consideration the reddening by the dust in the Milky Way (*Kessler et al.*, 2019b; *O'Donnell*, 1994). Later, the SEDs are convolved with DECam transmission curves accounting for atmosphere, telescope, filters, and CCDs. Given a cadence, the light curves are calculated by sampling the magnitude grid.

The 329 Kasen models, α_j, each with a range of time after burst, τ ($0.00 \leqslant \tau \leqslant 16.7$ days), at the SNANA grid of redshifts, z_i ($0.003 \leqslant z \leqslant 0.2$), describe $829,080$ simulated magnitudes, $m_\lambda(\lambda, \tau, \alpha_j, z_i)$, for each of the 4 filters that we use (g, r, i, z).

5.2.1 DECam limiting magnitudes

We define the limiting magnitude as the magnitude at which we can measure a point source, e.g. a star, with 0.1 mag error, which corresponds to signal-to-noise ratio, SNR ~ 10. We then define the limiting magnitude m_0 for a total effective exposure time of 90 sec, i.e. $t_{\rm exp} \times t_{\rm eff} = 90$s, where $t_{\rm eff}$ is a unitless quantity that scales the exposure time to the 'effective' exposure time when taking into account sky conditions (higher $t_{\rm eff}$ being better sky conditions). Then, to scale up for different exposures, we construct:

$$m_{\rm lim} = m_0 + 1.25 \log\left(t_{\rm eff} \times \frac{t_{\rm exp}}{90{\rm s}}\right), \tag{5.1}$$

which reflects S/N going as the square root of time in a sky noise limited observation. We use the m_0 measured in the DES data by *Neilsen et al.* (2016), thus the 90s

Table 5.1 Observational conditions (photometric filter, limiting magnitude, and effective exposure time) averaged from DECam follow-ups of previous observations. Note that the higher the $t_{\rm eff}$ value (which ranges from 0 to 1), the better the observational conditions.

Filter	m_0	$t_{\rm eff}$ (bright time)	$t_{\rm eff}$ (dark time)
g	23.4	0.05	0.7
r	23.1	0.15	0.8
i	22.5	0.45	0.7
z	21.8	0.6	0.6

Table 5.2 DECam $m_{\rm lim}(10\sigma)$, dark time.

	Exposure time (sec)			
Filter	10	100	1200	3600
g	22.0	23.3	24.6	25.2
r	21.8	23.0	24.4	25.0
i	21.1	22.4	23.7	24.3
z	20.3	21.6	22.9	23.5

Note. — $\Delta m_{\rm lim}(10\sigma - 5\sigma) = 0.75$ mags.

normalization factor, and present those values in Table 5.1, and the derived limiting magnitudes in Table 5.2. The $t_{\rm eff}$ is closely related to observational conditions during the night. Therefore, we break observing into nights of bright time and dark time and use $t_{\rm eff}$ from previous target of opportunity programs in DECam, in particular the observations from past GW follow-up events (*Morgan et al.*, 2020, *Garcia et al.*, 2020). Throughout this chapter, we focus on detectability on dark nights unless otherwise stated.

Table 5.3 Observational parameter space Θ explored.

Time after burst (Days)	$0.5, 1.0, 1.5, 2.0, 2.5, 3.0, 3.5, 4.0$
Scenario 1	
Filter	g, r, i, z
2d credible sky area covered	$0.9, 0.85, 0.8, 0.75, 0.7$
Exposure time (sec)	$60, 90, 120, 200, 300, 600, 1200, 3600$
Scenario 2 (with inner & outer region)	
Filter	g, r, i, z
2d credible sky area covered	
Outer: 0.9	Inner: $0.8, 0.7, 0.5, 0.3$
Outer: 0.8	Inner: $0.7, 0.5, 0.3$
Outer: 0.7	Inner: $0.5, 0.4, 0.3$
Outer/inner exposure time pairs (sec)	60/90; 90/120; 120/200; 200/300; 300/600; 300/1200; 600/1200; 600/2400; 1200/2400; 2400/3600; 3600/5400

5.2.2 Cadences & observational parameters

We use of SNANA to find effective search strategies that maximize candidate detection, considering realistic conditions, including the maximum duration of the night, intervals between observations, and sky brightness, while also minimizing telescope time and enabling earlier discovery. This is at base a trade-off of exposure times versus sky area coverage, but with additional complications of filter choice and the time since the event occurred. We limit our telescope time expenditures to 8 hours per night and assume Blanco/DECam has telescope/readout slew time of 30s between the exposures, which is true for slews less than 10 degrees. We test four filters, g, r, i, and z, starting 12 hours after the trigger, and going to 4 days post-merger in half-day increments with several exposure times. These are summarized in Table 5.3.

We define two exposure time scenarios. In Scenario 1 we cover the area of a given GW event with a single set of exposure times and in Scenario 2, we explore the use

of two different exposure times for a single search. The latter is motivated by the need to cover the high probability area sky with deep exposures, while covering the larger low probability localization area outskirts with shorter exposure images. We designate central high probability areas as the "inner region" and the rest of the area inside the localization region as the "outer region". The last section of Table 5.3 presents the combinations considered for the inner region, ranging from 30% to 80% sky probability coverage, for 3 different values of the total (deep+shallow) sky map probability coverage, from 70% to 90%. For instance, a combination of 40% probability for the inner region and 70% total coverage means that the 40% highest probability region is covered with higher exposure time and the $70 - 40 = 30\%$ left over is covered with the shorter exposures. Each of these combinations is considered for all possible deep and shallow exposures presented in Table 5.3. For scenarios where we cover the sky area twice in a single night, we additionally take into consideration the KN variability a few hours after the first search.

5.2.3 Simulation data summary

We simulate a set of GW detections $S = S_1, \ldots, S_n$, where $n = 860$ and S_i is the i^{th} simulation with distance d_i. For each S_i we evaluate each of the parameter sets Θ in the two scenarios. In Scenario 1 there are 8 passes since burst, 4 filters, 8 exposure times, and 5 sky area probability coverages: $8 \cdot 4 \cdot 8 \cdot 5 = 1280$ possible parameter sets. In Scenario 2 there are $8 \cdot 4 \cdot 11 \cdot 10 = 3520$ possible parameter sets to be evaluated. Over both, 4800 observation models are evaluated. Each model is evaluated with the machinery described in Section 5.1, resulting in SNANA kilonova

measured magnitudes. We have done this for each of the 329 Kasen models.

5.2.4 Discovery probability

We define the probability of detection, p_{α_j}, of the KN model α_j for the j^{th} combination of $(M_{\rm ej}, \log(X_{\rm lan}), v_{\rm ej})$, with observed magnitude $m_\lambda = m(\lambda, \tau, \alpha_j, z_i)$ in a given filter λ, for a given exposure time $t_{\rm exp}$ weighted by observing condition $t_{\rm eff}$ for an event at mean redshift, $\bar{z}$, over the SNANA grid of redshifts, z_i:

$$p_{\alpha_j} \propto \sum_i \begin{cases} pr(\alpha_j) \cdot pr(z_i), & \text{if } \mathrm{m}_\lambda < \mathrm{m}_{\rm lim} \\ 0, & \text{if } \mathrm{m}_\lambda \geq \mathrm{m}_{\rm lim} \end{cases} \tag{5.2}$$

where

$$\begin{aligned} p_{\alpha_j} &\equiv p_{\alpha_j}(\text{Detection}|\tau, t_{\rm eff}, \Theta, \bar{z}), \\ \mathrm{m}_\lambda &\equiv \mathrm{mag}_\lambda(\lambda, \tau, \alpha_j, z_i), \\ \mathrm{m}_{\rm lim} &\equiv \mathrm{mag}_{\rm lim}(\lambda, t_{\rm eff}, \Theta), \quad \text{and} \\ pr(z_i) &= \exp\left(-\frac{(z_i - \bar{z})^2}{2\sigma_{\bar{z}}^2}\right), \end{aligned}$$

where τ is time after the GW detection, Θ contains the specific observation strategy characteristics including $t_{\rm exp}$, $\mathrm{m}_{\rm lim}$ is the limiting magnitude of the observation, and $pr(\alpha_j)$ are the model priors. The summation is over all redshifts for a given model, j at a given τ. Eq. 5.2 represents a Gaussian prior for choosing light curve models from the grid of SNANA defined redshifts given the GW distance. Explaining it differently, Eq. 5.2 is, for a given Kasen model, examining whether the resulting

apparent magnitude is less than the limiting model with a Gaussian prior on the redshift, using the GW event mean redshift, $\bar{z}$, and the grid of SNANA redshifts the KN could be at, weighted by the GW event variance in redshift, $\sigma^2_{\bar{z}}$.

In order to obtain the total probability of detecting the transient once, we also need to take into account the explored volume. The GW localization maps present the probability that the event is located at a given sky position, the luminosity distance at that position and its uncertainty. Therefore we define the total probability of detecting an event as

$$P_d = \frac{\int_{\hat{\Omega}} d\Omega \; d_L(\Omega)\, p(\Omega)}{\int_{\hat{\Omega}} d\Omega \; d_L(\Omega)} \times \sum_{j=1}^{329} p_{\alpha_j} \,, \tag{5.3}$$

where

$$P_d \equiv P(\text{discovery}|\hat{\Omega}, \tau, t_{\text{eff}}, \Theta, \bar{z})$$

and $\hat{\Omega}$ is the entire sky area observed in the follow-up, the $d\Omega$ is the voxel, $p(\Omega)$ is the probability in the voxel, and $d_L(d\Omega)$ is the luminosity distance to the voxel. The sum over p_{α_j} includes the priors and thus indicates the model used. The sky coverage and exposure times determine the total telescope time for a given KN detection. We note that we use 3-d spatial localization, rather than 2-d on-sky probabilities, thus the d_L weighting in eq 5.3 and the attendant implication that we can have a higher detection probability than on-sky credible area covered. We can now evaluate P_d for a given set of Θ.

5.2.5 Confirmation probability

In order for an object to be confirmed as a kilonova candidate, we require it be detected twice (in two observing 'epochs'). This requirement can be lifted if, for example, there are sufficient spectroscopic resources available to follow up all of the candidates found after a single epoch. Generally, this is not the case, however. The second detection eliminates spurious detections, including image artifacts, asteroids, and other possible contaminants (*Morgan et al.*, 2020; *Shandonay et al.*, 2022). Another reason to consider the detections independent is that we typically observe while working on post-processing and making target selection for spectroscopy in the data from the previous epoch.

Given that we want to make two detections to positively identify kilonova candidates, we define the probability of confirming the transient with two independent detections as:

$$P_c \equiv P(\text{confirmed}) = P_{d,1} \cdot P_{d,2} \tag{5.4}$$

In this form P(confirmed) has an extra spatial/volume probability term multiplied in. This is irrelevant from an optimization viewpoint and we defined it this way for ease of computation.

5.3 Optimizations and Kilonova Types

After calculating P_c for each O4 event in two observing scenarios each with a grid of observational parameters we can evaluate what works best to optically find the

kilonova. The answer to this depends on the science goal. Our primary science aim is standard siren cosmology, so we set a goal to identify counterparts to every kilonova that the LVK detects as a GW event. In this section we discuss optimizing the strategy given the science goal and then discuss the detailed metric, which involves exploring the meaning of covering the space of Kasen models.

5.3.1 Optimizations

We derive P_c for each of the 1280 parameter combinations of Scenario 1 and for each of the 3520 combinations of Scenario 2, resulting in 4800 total for each simulated merger detection event, S_i. Not all of these combinations have an appreciable P_c much above zero, as most of the predicted magnitudes are below sky noise.

We use P_c as the variable to optimize on. We choose the highest P_c for each sim S_i, look up the set of observational parameters Θ_i for it, and define this the *Top* strategy. Choosing the highest P_c is the simplest optimization, but for our evaluation we need at least two more, *Reference* and *Low Telescope Time*.

1. *Top Strategy* is the Θ_i producing the highest P_c for each S_i, the observational parameters producing the highest probability of confirmation for every O4 simulation.

2. *Low Telescope Time (low-TT)* is the Θ_i combination that uses the lowest telescope time given while retaining a P_c within 10% of the highest confirmation probability strategy, by definition *Top*. For example, if the *Top* strategy finds $P_c = 0.85$, then a *low-TT* strategy will have $P_c \geq 0.75$, usually with a much

reduced telescope time. We will find it interesting to vary the threshold away from 10%.

3. *Reference Strategy* has the 90% probability sky area observed in i and z bands with 90 second exposures on the first two nights after the merger. This strategy models previous DECam searches, in particular the extensive search of *Morgan et al.* (2020), and has been used as the DECam strategy for the predictions of *Chase et al.* (2022).

The *Top* strategy uses as much telescope time as needed to cover the full probability volume. All strategies work within the constraint of requiring two passes over two 8 hour nights.

5.3.2 Bayesian Average Models

Not every Kasen model atmosphere is equally likely to be a good model for a real KN light curve. Most models for GW170817 are 2+ component models, as in *Kilpatrick et al.* (2017); *Villar et al.* (2017); *Coughlin et al.* (2018); *Gillanders et al.* (2022). If the Kasen models define a linear space of KN models, then the Kilpatrick models are in that space; if the Kasen models are eigenmodels of KN, then the models in Kilpatrick et al are defined by the eigenvalues multiplying the eigenmodels. Both the values of the non-zero eigenvalues and the number of non-zero eigenvalues are highly model dependent. Dropping the eigenvector language, it is clear that in the current situation of very few well studied KN, the number of components in models describing KN candidates is uncertain.

One of the most common ways to define detection efficiency in the literature is to set up a grid of KN models, for example over viewing angle, as done for a χ^2 analysis and then to calculate the fraction of models detected given an observation. This makes the detection probability explicitly dependent on non-physical choices of the grid breadth and grid spacing. In our case, the grid would be the 329 Kasen models, even though these models were meant to extend past the range of models likely to describe real KN. In a Bayesian framework, each of these models would come with a prior describing our belief in their applicability.

We will employ the useful idea of a Bayesian model average. We evaluate the entire grid of Kasen models, but instead of a uniform weighting, we place a Bayesian prior, $pr(\alpha)$, on each model. The Bayesian average model detection probability is implicit in eq 5.2, but can be thought of as:

$$\langle P_d \rangle = \sum_{j=1}^{329} P_d \cdot \, pr(\alpha_j) \tag{5.5}$$

where $\sum pr(\alpha_j) = 1$. Here we will use Gaussian priors to produce three Bayesian average models, *bright & blue*, *reddish & slow*, & *red & faint*, as given in Table 5.4. It is useful to guide the intuition to form the Bayesian average model absolute magnitude,

$$M_\lambda(\lambda, \tau) = \sum_{j=1}^{329} M_{\alpha_j}(\lambda, \tau, \alpha_j) \cdot \, pr(\alpha_j)\,, \tag{5.6}$$

of which peak M_i is also given in Table 5.4 and light curves shown in Fig 5.2. This mean quantity, while illuminating, is incomplete as the Bayesian formalism is designed to make the uncertainties explicit- the curves are to thought of as the

median value of a band of light curves weighted by the prior.

Table 5.4 Kilonova Gaussian model priors.

	Blue & Bright		Reddish & Slow		Red & Faint	
	μ	σ	μ	σ	μ	σ
$M_{\rm ej}(M_\odot)$	0.025	0.001	0.025	0.01	0.035	0.15
$\log(X_{lan})$	-5.0	1.0	-5.0	10.0	-2.0	5.0
$v_{\rm ej}$ (c)	0.25	0.01	0.25	0.10	0.15	0.30
Peak $\langle M_i \rangle$	-16.3		-15.7		-14.6	

Note. — Table of means, μ, and standard deviations, σ, of the Gaussian priors on the Kasen models parameter ranges. The Kasen models have parameter ranges of:

$$0.001\ \mathrm{M}_\odot \leqslant M_{\rm ej} \leqslant 0.1\ \mathrm{M}_\odot$$
$$-9 \leqslant \log(X_{\rm lan}) \leqslant -1$$
$$0.03c \leqslant v_{\rm ej} \leqslant 0.3c$$

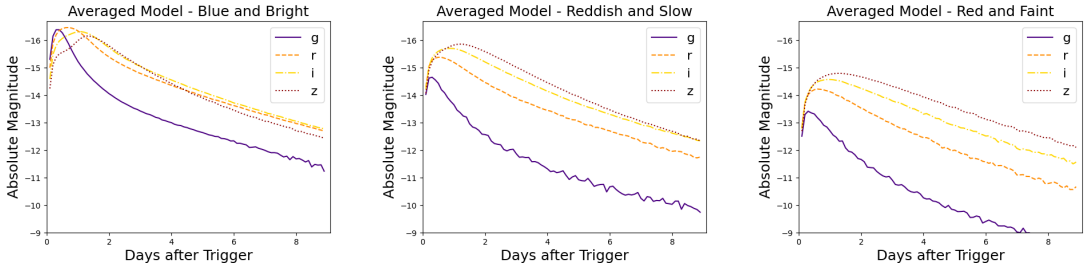

Figure 5.2 The absolute magnitudes vs days after the trigger for the weighted average of three sets of priors in the KN parameter space models considered.

The *bright & blue* model is defined as the means and uncertainties of the blue component model in *Kilpatrick et al.* (2017) interpreted as Gaussian priors. As there are no uncertainties given for the blue model, we assume for $M_{\rm ej}$ a relatively narrow 0.001, and for $v_{\rm ej}$ of 0.01. Where *Kilpatrick et al.* (2017) has the blue model lanthanide fraction evolving from $\log X_{\rm lan} = -4$ to -6 as the opacity falls due to KN atmosphere expansion, we take $\log X_{\rm lan} = -5$ with an uncertainty of 1.0. This model

is, in average, blue and reaches a peak luminosity a half day after trigger in g-band. It is also, in average, the brightest of the three models and 0.8 magnitudes brighter than GW170817's peak $M_{g,r,i,z} \approx -15.5$.

The *reddish & slow* model is defined as in *bright & blue*, except that we take the σ to be ten times the uncertainties there, to reflect our ignorance of the KN population. This results in a prior allowing the entire $\log X_{\rm lan}$ range of the Kasen models to contribute. Such wide priors make our model, in average, to be redder and slower to peak than GW170817, though with the same $\langle M_i \rangle$. Most of our results use this model.

The *red & faint* model is defined as the means and ten times the uncertainties of the red component model in *Kilpatrick et al.* (2017) interpreted as Gaussian priors. The predominantly lanthanide-rich Kasen models contribute. This results in a model that is, on average, redder and fainter than GW170817, with a peak $\langle M_i \rangle$ fainter by 1 magnitude, and a $\langle M_r \rangle$ fainter by 1.4 magnitudes. This model aligns with what is expected by most models for viewing KN in the orbital plane, where the lanthanide-poor material is hidden from view.

We will use our three models in various ways to evaluate the optimized strategies. The *bright & blue* model will be the easiest to detect, as the light curves peak brighter than -16 in g, r, i, z. The *red & faint* model will be the hardest, as the absolute magnitude peaks only brighter than -13 in g, barely -14 for r, approaching -15 for the observationally more difficult i, z. The *reddish & slow* model is intermediate. In this chapter, we often use *bright & blue* to inform the reader's intuition to a low inclination angle KN. We use *red & faint* to show the effect of a faint KN on the

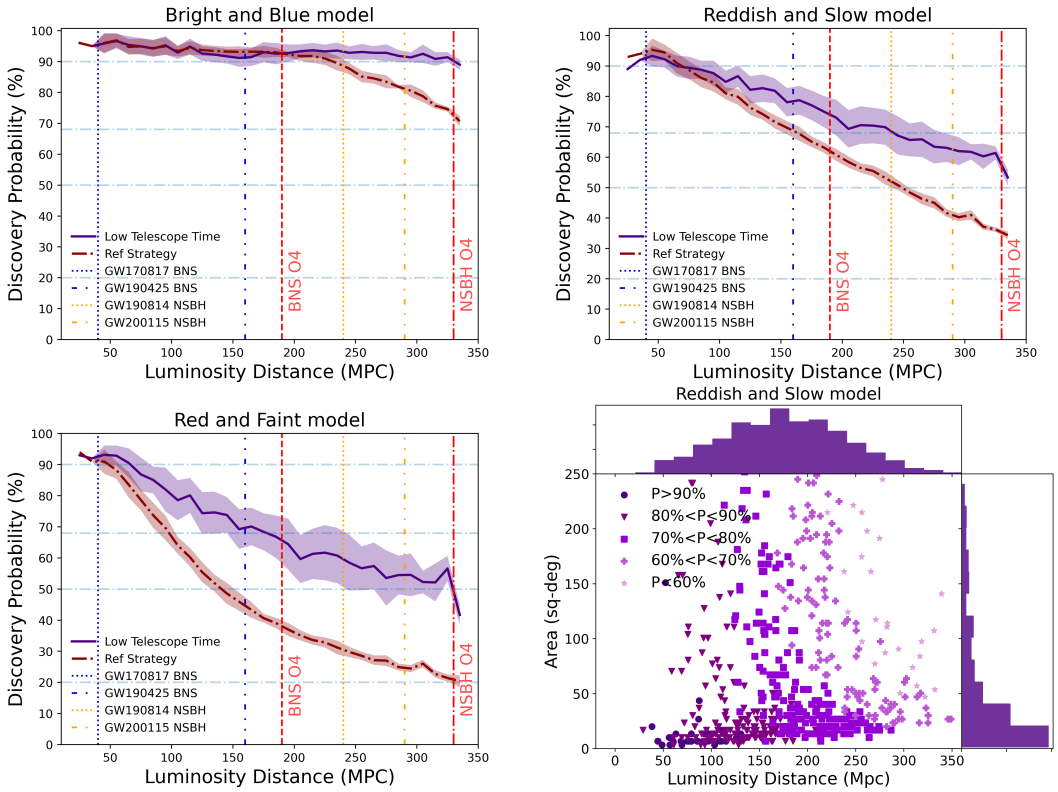

Figure 5.3 Discovery probability vs luminosity distance using the *low-TT* observing strategy compared to the *Ref* strategy. Each plot describes a different KN model where (Upper Left:) *bright & blue*, (Upper Right:) *reddish & slow*, (Bottom Left:) *red & faint*. The shaded region about the median line represents the 68% confidence interval of the scatter among the simulations. We also mark the distance to the upper limit of the LVK O4 projected range as well as noted GW events for reference. Bottom Right: distribution of simulations for the *low-TT* strategy, binned by detection probability in our wide prior model, *reddish & slow*. The marginal histograms are detection probability weighted.

strategies. It can be argued that the *red & faint* represents the most likely KN from a NSBH merger. We often use *reddish & slow* as an intermediate case that shows the behavior of choices in strategy optimization well.

There remains considerable uncertainty in the KN population statistics. While our three models are comparable to those in, e.g., *Zhu et al.* (2023); *Sagués Carracedo et al.* (2021); *Coughlin et al.* (2020); *Petrov et al.* (2022), the population study of *Setzer et al.* (2022) has a two peaked absolute magnitude distribution, at i-band absolute magnitudes of -15 and -12. In that study, GW170817 is a 95^{th} percentile event in luminosity, and the 50^{th} percentile luminosity corresponds to our $\langle M_i \rangle$ for *red & faint*. The *Setzer et al.* (2022) study is for a random distribution of inclination angles and thus corresponds to the intrinsic KN population, whereas it is known that GW observatories predominately select merging compact objects with inclination angles near $\approx 30^{\circ}$ (see *Finn and Chernoff* (1993); *Nissanke et al.* (2010); *Schutz* (2011)). The observed KN population from GW event follow up will mostly be from the first peak of Setzer et al. While a KN sample with $M \approx -12$ would be challenging even for a 4m telescope, the first peak $M \approx -15$ is inside our model ranges.

We take our priors from *Kilpatrick et al.* (2017) because we wish to emphasize the uncertainties in the models in this study. The uncertainties in the models reported by *Villar et al.* (2017), for example, are much smaller. For observations in O4, the models and uncertainties in *Coughlin et al.* (2018) are likely better. We suggest using the 2-component lightcurve red and blue models as the counterparts to our *bright & blue* and *red & faint* models, interpreted as the low and large inclination angle models and to use the 1-component model with 10σ as the counterpart to our

reddish & slow, interpreted as a maximally uncertain KN population model.

5.3.3 Strategies and KN models

We begin our study of the strategies. As the community routinely uses the probability of detecting a KN once, calling this discovery, we will be showing $P_d \equiv P_{d,1}$ in most of the succeeding plots. Note that the strategies are all optimized on P_c.

Reducing our GW population statistics to only distance, we can describe the NS-NS merger population as having a median d_L of 150 Mpc, a 75%-tile of 225 Mpc, and having only 1% at $d_L > 300$ Mpc. We take 200 Mpc as a characteristic distance.

We show in Figure 5.3 the *low-TT* strategy discovery probability as a function of distance and compare it to the reference strategy. Starting with the easy case model, *bright & blue*, we see that the *low-TT* detection probability has a ceiling at $\approx 90\%$. The reference strategy P_d falls after 200 Mpc, whereas the *low-TT* P_d remains high out to 330 Mpc. The *red & faint* model is difficult for the reference strategy after about 100 Mpc, whereas the *low-TT* has $P_d > 50\%$ out to 330 Mpc. The *reddish & slow* model is intermediate and the *low-TT* performs well. The luminosity distance vs area distribution shows the probability weighted histograms on the margins. Not surprisingly, small spatial localizations are both are easiest to make identifications for, but less obvious is that the most likely distribution of distances for detection is flat between 125 Mpc and 175 Mpc.

The exposure time must be balanced by the sky area to be covered: in our maximum 8 hours per night, DECam using 1 hour exposures can survey 24 square

degrees per night.

Turning to the distribution of telescope time required per event in Figure 5.3, we will explore the motivation and design of the *low-TT* strategy. For the by construction best in P_c strategy *Top* the mode of the time required is $\approx 13 - 15$ hours for *reddish & slow* & *red & faint*, but saturates at $3 - 5$ hours for *bright & blue*. The *Top* strategy likes to use all the time available over two nights to maximize detection. The *low-TT* strategy is the lowest telescope time within 10% of *Top*'s P_c, but clearly one can tune how much loss in P_c one is willing to accept. We have compared choosing 5%, 10% and 15% (see Table 5.5) and not surprisingly the best choice depends on the KN model chosen. For the *bright & blue* model, a threshold of 5% gives a strategy that outperforms the Reference strategy in P_d while using less telescope time. For the *reddish & slow* and *red & faint* models, we prefer to set the threshold at 10%. This produces in the *reddish & slow* case a strategy that uses a factor of 3 less telescope time than *Top*, and the *red & faint* case a factor of 2 less, for a loss in $P_c < 10\%$. The gain in P_d over the reference strategy is particularly dramatic for *red & faint* at higher distances.

The plots in Figure 5.4 show how the *low-TT* strategy selects its optimized choice as compared to *Top*. All 4800 $P_{d,1}$ for the parameter combinations in Table 5.3 for a single event simulation are shown, color coded by the required telescope time. The highest $P_{d,1}$ tends to use the highest telescope times, but there are many high $P_{d,1}$ parameter combinations Θ_i that use much less telescope time. The lower plot has the *Top* and *low-TT* strategies marked. Generically, our strategies prefer balanced $P_{d,1}$ and $P_{d,2}$ to maximize P_c.

Table 5.5 Average telescope time per event in hours required for two detections, discovery and confirmation. The events used were all that had 90% probability area < 300 sq-deg. From 860 events, 611 are retained after this cut. The 50%, 90% or 100% columns give average times for events ordered by the statistics of the size of the 90% localization area, low to high.

Strategy	Telescope time (hours)		
bright & blue	50%	90%	100%
Reference	0.4	1.1	1.6
Top	2.3	3.0	3.2
low-TT (5%)	0.4	0.9	1.3
low-TT (10%)	0.4	0.9	1.2
low-TT (15%)	0.2	0.7	0.9
wide prior, reddish & slow			
Reference	0.4	1.1	1.5
Top	10.5	12.1	12.2
low-TT (5%)	5.2	6.8	7.0
low-TT (10%)	3.2	4.3	4.5
low-TT (15%)	2.2	3.0	3.2
red & faint			
Reference	0.4	1.1	1.6
Top	10.4	12.3	12.6
low-TT (5%)	7.4	9.1	9.2
low-TT (10%)	5.4	6.3	6.4
low-TT (15%)	4.1	4.8	4.8

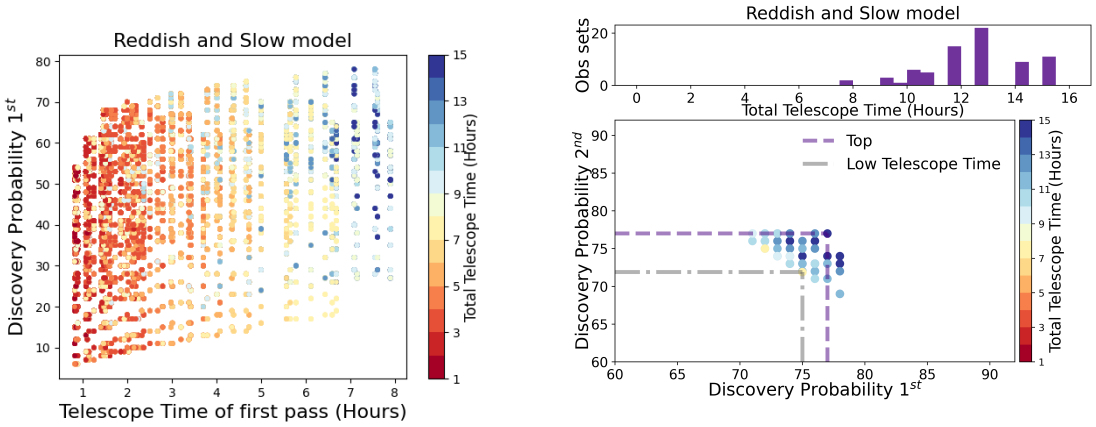

Figure 5.4 Left: Discovery probability vs time to completion of first pass for a single event at 160 Mpc with sky area of 168 sq-degrees. Total telescope time in hours is denoted for each Θ_i. Right: The best 10% of Θ_i from the upper plot, displayed in a $P_{d,1}$ vs $P_{d,2}$ plot with total telescope time color coded. The Θ_i corresponding to *Top* and *low-TT* strategies are marked. The histogram gives the distribution of telescope times for the Θ_i in the lower plot.

There is the question of "when is it good enough?", of diminishing returns. We can adopt the *reddish & slow* model compared to the reference strategy, for example, and work with the best 90% of events. Then the *low-TT* at a cost of $\times 4$ more telescope time detects 20% more KN and Top t the cost of $\sim 12\times$ more telescope time detects only $\sim 30\%$ more KN. Whether one is willing to accept the cost depends on the science case. For the standard siren cosmology case which wants to maximize the number of KN detected, one would prefer the maximum return of *Top*, but might be willing to accept the rate of *low-TT*. For the science case of studying the astrophysics of KN, where one wants to select good objects for detailed astrophysical study, gathering the next 10 expected in O4 might well be worth expending what *Top* requires for the right events.

Returning to the performance of the strategies, we delve deeper in Figure 5.5 for

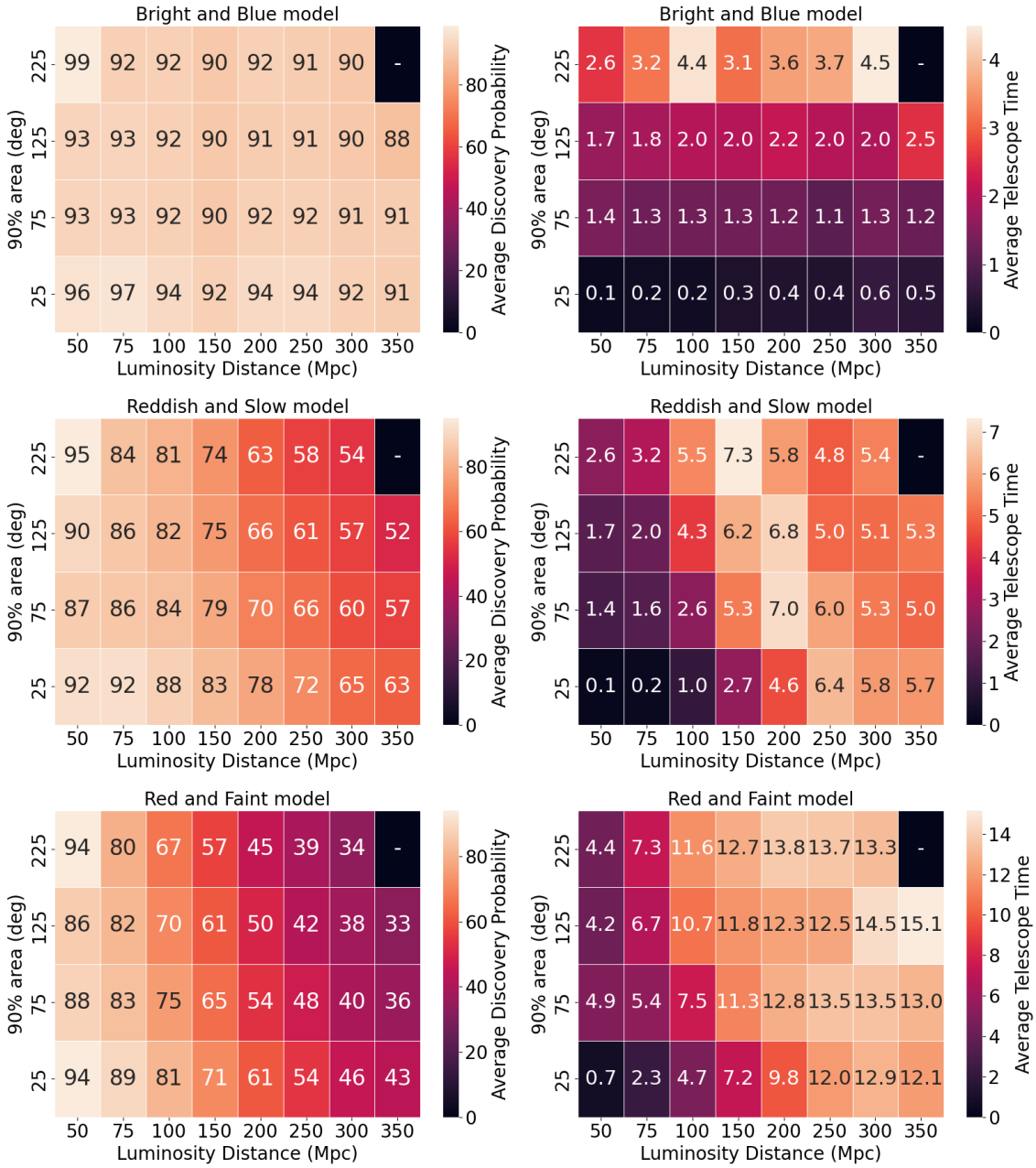

Figure 5.5 Using the *low-TT* model, *Left column*: Detection probability for a given luminosity distance and sky area for *reddish & slow*, *red & faint*, *bright & blue* in (top), (middle), and (bottom), respectively. *Right column:* Average required telescope time per event area as a function of luminosity distance, ordered the same as in the left column.

the *low-TT* strategy. In this plot, we present detection probability as a function of sky area. Here the distance weight in equation 5.3 becomes important. In each event, the detection probability calculated for each voxel in the skymap is weighted by the distance to that voxel to form a distance weighted detection probability for the whole event. This accurately weights the probability for the often smaller distances in the lower probability areas of the sky map (see, e.g., *Singer et al.* (2016b)). Thus the detection probability for *bright & blue* at $d_L = 50$ Mpc can be 99% when we only cover the 90% sky probability region.

The easiest way to understand Figure 5.5 is to start with the right column and especially the *bright & blue* model. We have seen from Figure 5.3 that *low-TT* is very effective at discovery for this model and the two dimensional projection shown in Figure 5.5 shows little variation about that high efficiency. What variation is present is the expected loss of efficiency with increasing distance and area. In the right column for the *bright & blue* case, it is clear that the telescope time required increases with increasing distance and area. The increase with area is very nearly the ratio of the sky areas.

The *red & faint* model efficiency plot shows that the dominant variation is a decrease in efficiency with increasing distance as the faint objects fall below the limiting magnitude for the maximum exposure time. Table 5.3 shows a maximum exposure of 1 hour so in our 8 hour maximum night, DECam can cover 24 sq-degrees. The variation in sky area is not as dramatic as with distance and shows the success of the inner/outer split in Scenario 2 when deep exposures over the high probability area are combined with shallower exposures over the lower probability area. (Note

that eq 5.2 was evaluated separately in each area.) The corresponding telescope time plot behaves as expected with increasing telescope time with increasing distance and area.

The intermediate *reddish & slow* model behaves as expected in efficiency. It is more $m_{\rm lim}$ dominated than *bright & blue* and doesn't require $m_{\rm lim}$ as deep as *red & faint*. The smallest area bin is likely using 1 hour to maximize area coverage. The corresponding telescope time plot cell shows 5.7 hours for the average event, likely less than 8 hours because of the events with less than 24 sq-degree sky area. The telescope time plot as a whole shows a surprise. There is a peak in the time at intermediate distances and areas, and then the time falls with further distance. One can see that some of the same behavior in the top row of the *red & faint* model telescope time plot. The explanation is that there are strategies (here meaning Θ_i) that use high telescope time to maximize $P_{d,1}$ but these take so long to cover the area that $P_{d,2}$ is compromised by the fading of the KN, and thus P_c is lowered. A higher P_c is obtained by using a shorter time to cover the area to cover the area before the object fades, thus maximizing the product of $P_{d,1} \cdot P_{d,2}$.

5.4 Exploring the Parameter Space

We have constructed 4800 parameter-set evaluations of DECam kilonova magnitudes produced by SNANA for 860 Bayestar simulation-detected O4 binary neutron star merger events. We have developed a methodology that uses discovery and confirmation probabilities and a set of optimization rules to produce strategies optimized for the discovery of KN under certain constraints. We have discussed maximized dis-

covery (*Top*) and minimal telescope time (*low-TT*) already, and will discuss several more strategies in 5.4.2. Here we will show detailed behavior of the strategies.

We use the *reddish & slow* (GW1701817-blue, $10 \times \sigma$) KN model for the results in this section unless otherwise stated. Likewise, we will use the *low-TT* strategy for the results in this section unless otherwise noted. To recap this strategy, we go through all combinations of inner & outer region sizes and exposure times as listed in Table 5.3 and present the combinations that give the lowest telescope time within 10% of the highest confirmation probability strategy.

5.4.1 Exposure times

One of the dominant features of the observing parameters described in Table 5.3 is the splitting of Scenario 1 and Scenario 2. In Scenario 1, the sky is covered with uniform exposure times. In Scenario 2, we allow the splitting of the sky localization area into an outer region and a longer exposure inner region. Scenario 2 is best thought of as a homogeneous pass with a deeper exposure in the high probability region. Putting aside the distance weighting, covering a sky localization area sets a ceiling on the discovery probability to the probability contained in that area, and thereafter it is maximizing the limiting magnitude in the sky area. Our optimal selections almost always prefer Scenario 2 over Scenario 1 as implicitly or explicitly the total telescope time is constrained.

Figure 5.6 shows the percentage of simulations that preferred each exposure time broken into inner and outer areas. The mode of the 2-d distribution for the inner region is 20 minute exposures, with 31% of events using that exposure time and 84%

of events using 20 minutes or less. For the outer region, the mode is 5 minutes, with 33% of events using that exposure time and 74% of events using 5 minutes or less. This is model dependent. The *bright & blue* model uses 90 seconds 99% of the time in the inner region and 60 seconds 99% of the time in the outer region. Most often, 87% of the time, this is a very small inner region of 0.3, and in 93% of the simulations chose the 0.9 outer probability area. This is the lowest exposure time combination for Scenario 2 in Table 5.3, and it is likely that the strategies would have used a shorter exposure time if available, although it is notable that the strategy did not prefer the available 60 sec homogeneous pass in Scenario 1. The *red & faint* model has a more complicated exposure time pattern for the inner area. In order of use, 2400, 600, 3600, 1200 second exposures are used in 26%, 18%, 16%, & 15% of the simulations, respectively. The outer area exposure time has a mode at 1200 seconds of 25%, with 13% and 14% for 2400 and 600 seconds respectively, and 17% of simulations use 300 seconds.

For distances out to 125 Mpc, the difference between Scenario 1 and Scenario 2 is minimal, but at around 300 Mpc using scenario 2 gains $\sim$ 5%-10% in discovery probability. In other words, the slope in probability vs distance is shallower for the two-zone scenario than it is for the one-zone scenario. Therefore, we believe that using the deeper in the center approach will in general be more successful the more distant the event.

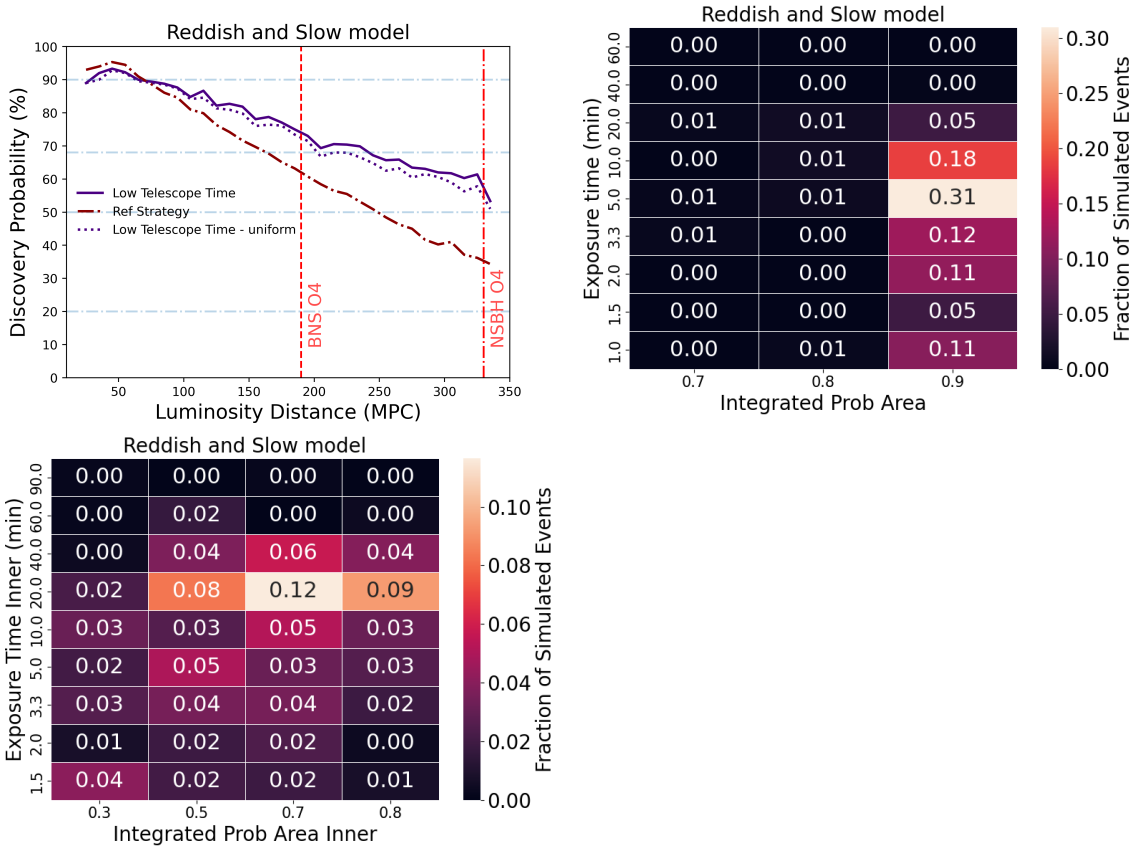

Figure 5.6 Upper left: discovery probability vs distance for *low-TT* comparing Scenario 1 and Scenario 2, as well as *Reference*, which only uses Scenario 1. The upper right and bottom plots show the exposure times that were most common when using Scenario 2, which breaks up the area into a shallower outer region and a deeper inner region of the spatial sky area.

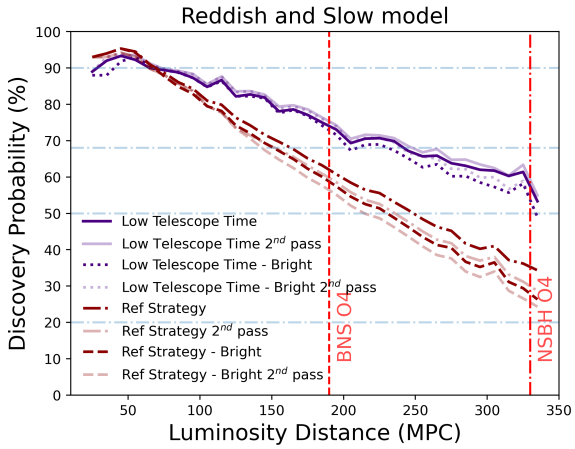

Figure 5.7 Discovery probability for the different strategies adopted in bright and dark time.

5.4.2 Filter Choice and bright/dark nights

In following up an LVK event, there is an equal chance of observing in dark conditions as in bright conditions. In Figure 5.7 we show the effect of dark versus bright time. The bright/dark distinction is handled in our methodology via a change in $t_{\rm eff}$ as seen in Table 5.1. Bright time lowers discovery probability by $5-10\%$, with the loss being mitigated by filter choice and exposure times. The filters used in the two passes are, in dark time, $rr(33\%), zz(50\%), ii+iz(17\%)$. In bright time the filters are $zz(71\%), ii+iz(25\%)$. The filter choices are strategy dependent, and, for comparison, the *Top* strategy used in dark time $rr(12\%), ri(7\%), rz(27\%), iz(29\%)$, and $zz(17\%)$ and in bright time $iz(45\%)$ and $zz(41\%)$. The filter choices are also model dependent, driven by the color evolution of the *reddish & slow* model as seen in Figure 5.2. The g filter is never going to be favored in this model, i will be picked the first night, z on the second, except that it is easier to go deeper in r than in i.

We can predict that the filter selection for *red & faint* model will be nearly the same but that the *bright & blue* model would predominately use g, r. Notably, it is not straightforward for us to say which filters we use in our best strategy.

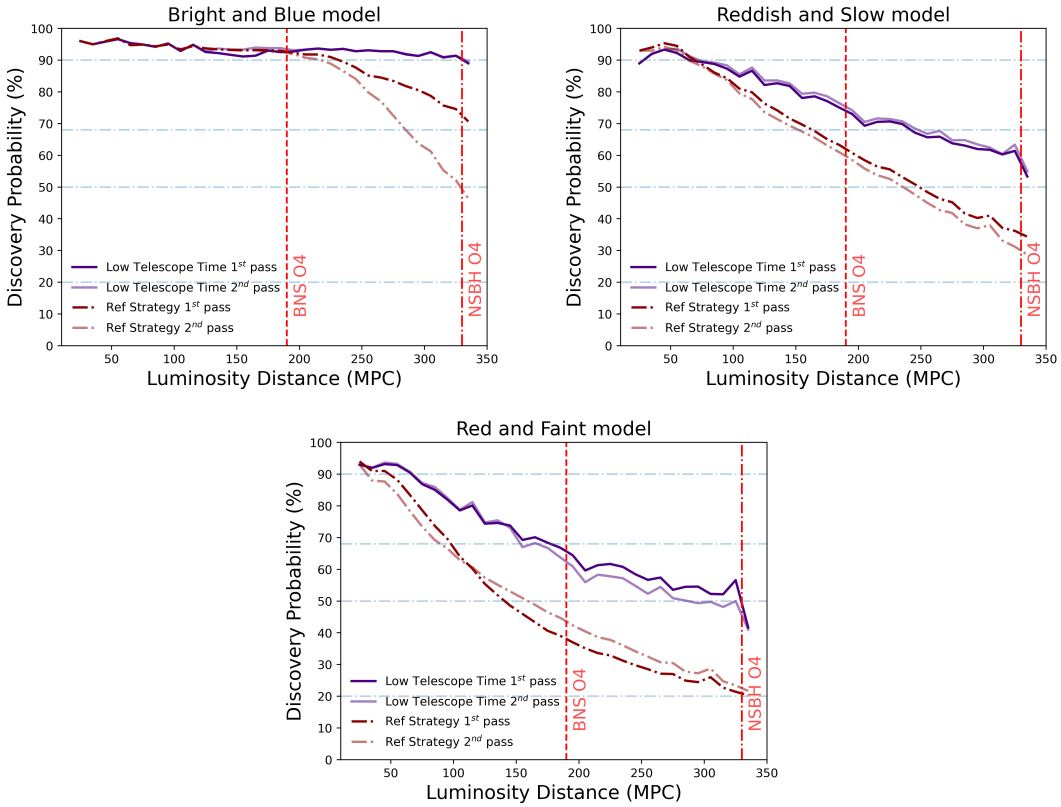

Figure 5.8 Discovery probability vs distance to event for the *low-TT* observing strategy in the first and second passes compared to the reference strategy for KN described by model with wide priors *bright & blue* (*upper left*), *reddish & slow* (*upper right*), and *red & faint*(*lower*).

5.4.3 Impact of the two-detection requirement

Detecting a counterpart twice in DECam images is an important step in our experience, as it allows one to distinguish extragalactic transients from asteroids or other objects within a short period of time. This requirement is common, for example *Zhu et al.* (2021), *Sagués Carracedo et al.* (2021), and *Petrov et al.* (2022) all demand two detections for a confirmation of a kilonova transient. Also important is covering the sky area with multiple filters to distinguish the KN from other transients.

The DECam search does not happen in isolation, and we do emphasize the importance of the broader GW community during these times. While our programs' main line is to proceed to confirmation via a second image, smaller telescopes may choose to follow up preliminary candidates in order to efficiently reduce the candidate list that will be sent to expensive spectroscopic efforts. There are reasons to be interested in both P_d and P_c.

In Figure 5.8, we show P(discovery) in the first detection, $P_{d,1}$, compared to the second detection, $P_{d,2}$. In the *low-TT* strategy the detection probability remains nearly constant between pass 1 and pass 2. This is not the case for the reference strategy. For the *reddish & slow* model there is a nearly constant offset between $P_{d,1}$ and $P_{d,2}$, where as for the *red & faint* model the $P_{d,1}$ is higher at $d < 100$ Mpc, and $P_{d,2}$ is higher at $d > 100$ Mpc. For the *bright & blue* model, we see the reference strategy become less efficient than the *low-TT* strategy at $d > 220$ Mpc, as both $P_{d,1}$ and $P_{d,2}$ drop with increasing distance. We infer that the *low-TT* strategy strongly prefers to balance $P_{d,1}$ and $P_{d,2}$.

5.4.4 Other Strategy options

Our choice of optimization has flexibility. We might place a high priority on the earliest possible discovery, or we may have lost several nights due to weather conditions and need to find an optimal approach for the first clear night several days after trigger. Let us, therefore, explore three other optimizations:

1. *Early Discovery (ED)* is the Θ_i that produces the earliest confirmation limited by the P_c from *low-TT*(5%) for each S_i.

2. *Late Discovery (LD)* is the Θ_i that produces the latest confirmation limited by the P_c from *low-TT*(5%) for each S_i. This family is intended to find a competitive strategy when one cannot observe during some early/intermediate nights or in case the event was not confirmed in the first days.

3. *Half Nights (HN)*. This family is intended to find a competitive strategy when one cannot observe half the night- if the object rises or sets for example, or the telescope is only allocated for half nights. Thus, from the subset limited by the P_c from *low-TT*(5%) for each S_i configurations we constrained the strategy to have both passes in less than 4 hours if they are in the same night or each of the passes takes 4 hours individually if they are in different nights.

All those configurations are restricted in telescope time. In Figure 5.9 we show the distributions of the time of second pass completion relative to the merger. It is in the second pass that we achieve a confirmation. The *ED* scenario not surprisingly has earlier times than *Top*, and, by design, earlier times than *LD*. The late discovery strategy has a different optimization and thus a different use. If the first night

or two are not useful for observations, then the *LD* strategy is useful for pursuing the discovery at late times. It peaks around 2.5 days after the merger. Note that this strategy is optimized on P_c, so does not describe the case where the event is unobservable due to clouds for a night or two, but rather is working the scenario where the object is detected but cannot be confirmed for several days. Figure 5.9 suggests that since P_d is on the first night, the most likely night to capture the confirmation pass is the third night. *LD* is representative of the kinds of strategies that would be necessary to deal with weather. The *Half Night* strategy enforces a limitation to the amount of time spent in pass 1, and the resulting performance is similar to *low-TT* in terms of both P_c and telescope time expenditures, although without the guarantee of being within 10% of the best strategy, *Top*.

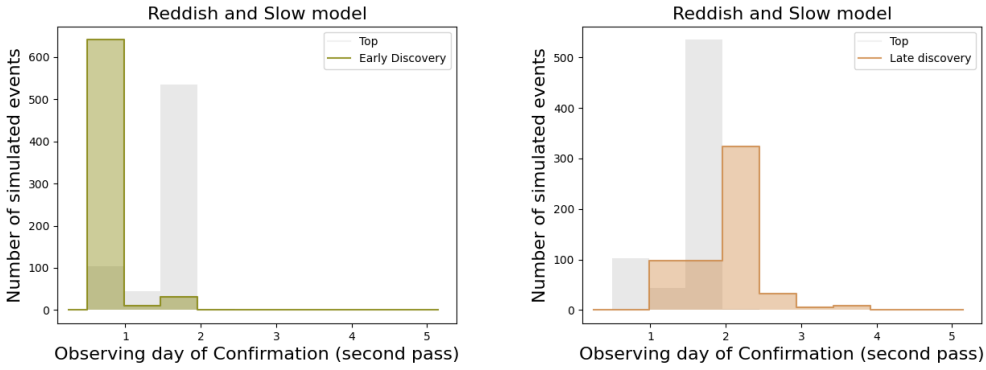

Figure 5.9 Distribution of confirmation day using the *reddish & slow* model. The left panel depicts the time of confirmation probability (i.e. how many days it took to observe the area twice) for our *ED* strategy and the right panel depicts the *LD* strategy. Most simulated events are confirmed by the first day. For reference, we also show the distribution using the *Top* strategy, which has no restrictions on when to perform the follow up.

Figure 5.10 shows the discovery probability versus distance for the strategies

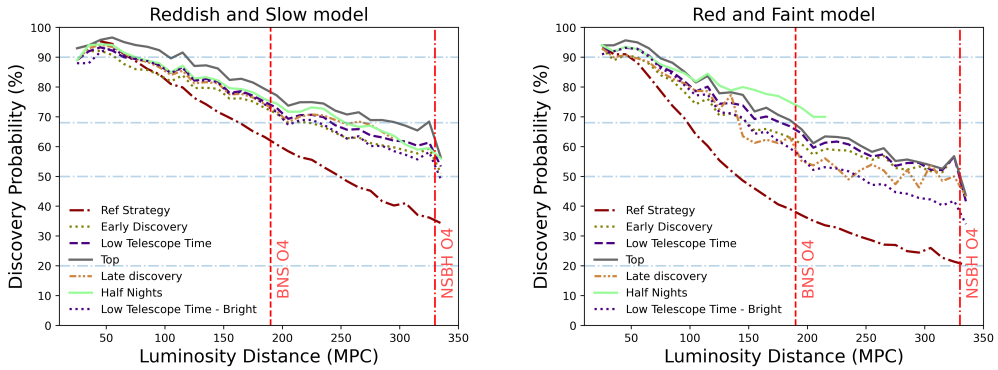

Figure 5.10 To illustrate the flexibility of the strategy families; we present the curves constrained with 5% of *Top* strategy, e.g. *low-TT* (5%) and derived strategies. Left: *reddish & slow*. Right: *red & faint*. Half Nights are not always available. For *reddish & slow* 395 half nights strategies produced detections, while for *red & faint* 137 half nights strategies produced detections. As the exposure times skew deep, the success rate is likely anti-correlated with sky area.

discussed here. For the *reddish & slow* model, all of our strategies have roughly equal performance (but see the *Top* outperforming *low-TT* by the amount it is allowed to) although with different telescope time cost. This is true to $d = 180$ Mpc, but after that, the *LD* strategy becomes less efficient. For the *red & faint* model, we see, interestingly, that the *low-TT* and *Top* strategies have equal performance. Finally, the *Half Night* strategy performs very well until $d = 180$ Mpc then becomes infeasible.

For the *reddish & slow* model, the *ED* strategy for exposure time distribution is more or less equally split among the possible outer/inner exposure time pairs in Table 5.3 up to the outer region exposure time of 600 secs, with the most likely outer exposure time of 300 seconds. There are no outer exposure time greater than 600 seconds nor inner exposure times greater than 2400 seconds. The *LD* strategy's most likely exposure time is 1200 seconds, and the strategy tries to cover the largest

inner region possible. The outer region has the most likely exposure time of 300 seconds and is never longer than 600 seconds. The strategy is to cover the largest inner region possible with relatively shallow outer region exposures. The second pass exposure time is weighted deeper than the first pass but the most likely exposure time remains 1200 seconds. The *Half Night* strategy for exposure time distribution is 31% of simulations using 1200 seconds, and 17% using 2400, most often in an 0.7 inner core region. The outer region uses 300 and 600 second exposures over half the time.

For the *red & faint* model, the *ED* strategy for exposure time distribution is deeper than for the same in *reddish & slow*, preferring 600, 1200, 2400 seconds instead of 600 and 1200, never using 90 second exposure times for the inner core like 15% of the *reddish & slow* simulations do. The *LD* strategy simulations 57% of the time use 600, 1200, or 2400 second exposures but uses a wide range of inner areas. The outer region uses all exposure times from 60 to 2400 seconds but is most heavily weighted towards 300, 600, and especially 1200 seconds. The *Half Night* strategy exposure time distribution is complicated, using a wide variety of inner areas and exposure times skewing deep at 1200 and 2400 second exposures. The outer region is similar, although here, as most often throughout the strategies, the outer region coverage of 0.9 is preferred.

5.5 Real observations

We have presented a variety of strategies optimized for a variety of purposes. Here we describe how to use them when an observing team receives an LVK alert.

We can compute P(confirmed) for the grid of Θ in Table 5.3 (both scenarios) using estimations of $t_{\rm eff}$ for the upcoming night. Given the Θ_i, we can choose a strategy to follow, placing the *Top*, *low-TT*, *ED*, or *Half Night* optimizations on as appropriate for the event. The optimization gives us the single Θ_i for each of the strategy families.

The strategy computation takes about 30 minutes on a single core. This includes the four strategy families (*Top*, *low-TT*, *ED*, *Half Night*), as well as considerations about bright/dark time. The time to complete the computation can be brought down to < 1 second by using the simulations as an approximation for the real event. Here our approach would be to choose a Θ_i by nearest neighbor search or to build a simple neural net on the simulation parameters and P(confirmed) to choose Θ_i.

The choice of the KN model is important. For example, if we are very early on-sky, with great observational conditions for just a couple of hours, or some limitation in telescope access is imposed upon us, we might also consider a fast detection of a blue flash (*bright & blue* model). This strategy could be interesting in particular for *low-TT* due to the cost of deep exposures over a wide area.

There is also a flow of decision making external to what we have described. Whether or not there is a short GRB, we choose distinct approaches. In the case that there is, we are likely looking for a GW170817-like event (*bright & blue*). If not, then a conservative model is indicated (*reddish & slow*), as we might not be looking for an event with a high inclination angle. If the alert indicates it is a NSBH merger, then the KN is likely more consistent with the *red & faint* model. After this, if there is a possible half night strategy, they are low budget and high performing

by definition. It also gives time for us to use spectroscopy to confirm quickly. In an observing run where we expect 1 BNS merger every month, we could plan on allocating telescope time through the run considering the amount of telescope time remaining versus where the particular event lies in an SNR distribution *Chen and Holz* (2014) or among a population of simulated events. This would lead to spending more toward the end of the run if considerable time was left, or spending more if it was a particularly good event compared to the simulations.

5.6 Discussion

In this chapter our science goal is to maximize the number of KN with GW measured d_L and securely identified redshifts. We put high weight on completeness of detection of the KN, given the considerable uncertainty in the KN population. Our strategies go deep. We reach $m_{\rm lim}(10\sigma)$ of $r \geq 24.4$ and $z \geq 22.9$ for the ≥ 1200 second exposures (see Table 5.2) for the inner regions of 47% simulations, regardless of distance (see Figure 5.6).

We can gain insight into our results by comparing how the literature handles a set of 3 questions:

1. the modeling of GW merger event distance and sky area distribution,
2. the range of KN model physical parameters, including inclination angle
3. the telescope, search and cadence, detectability versus distance and $m_{\rm lim}$.

The GW event properties: We simulate a merging NS-NS population expected in O4 given the expected LIGO sensitivities, drawing from the NS population, simulat-

ing the GW waveform and projecting onto a GW observatory network, and converting the GW observations to skymaps. Our draw, simulate, project, and form skymaps approach has been performed before (*Petrov et al.* (2022); *Chen et al.* (2021)), though it sometimes is done without skymaps (*Zhu et al.*, 2021). There are simplified approaches. One can just assume a KN population to observe (*Sagués Carracedo et al.*, 2021; *Setzer et al.*, 2022; *Chase et al.*, 2022). Or one can use toy GW models, such as a low-significance event skymap at 200 Mpc (*Coughlin et al.*, 2020). All of these approaches assume the KN properties are independent of the GW event properties, other than distance. *Colombo et al.* (2022) performs the more sophisticated analysis of connecting the KN properties to the GW event properties by going through the chirp mass and mass ratio, which informs $M_{\rm ej}$ and $v_{\rm ej}$. Of the analyses that go through the draw, simulate, and project methodology, all assume the SN > 8 or network SN> 12 in selection except for *Petrov et al.* (2022) which derive the effective SN threshold from the published GWTC events. They find that there will likely be more events with 90% credible sky areas > 300 sq-degrees than we simulate, but do not include in our follow up identification analysis. For the analyses that extend to jet production (e.g., *Zhu et al.* (2021); *Colombo et al.* (2022)) about 10% of events are sufficiently pole on to for jets to be observed.

Kilonova physical properties and inclination angles: We have only one well studied KN in the literature, so there is considerable uncertainty in the KN population. The literature has three ways of modeling KN- using model atmospheres as building blocks (e.g. *Kasen et al.* (2017)), full physical models of KN atmospheres (e.g. *Bulla* (2019); *Wollaeger et al.* (2021)), and using scaling relations and fitting functions

from relativistic numerical simulations (e.g., *Dietrich and Ujevic* (2017); *Coughlin et al.* (2019)). The first two approaches are parameterized by at least three variables (for us, $M_{\rm ej}, v_{\rm ej}, \log X_{\rm lan}$). The Bulla models, which include inclination angle explicitly, are widely used in the relevant literature (e.g., *Coughlin et al.* (2020); *Sagués Carracedo et al.* (2021); *Zhu et al.* (2021); *Petrov et al.* (2022)). Often, analyses in the literature will set up a grid of KN parameters and inclination angles and proceed to simulate detection of each entry in the grid, either for a fixed distance or for NS merger population. Typically the fraction of models detected is termed the detection efficiency. This makes the detection efficiency depend on the model space in unfortunate ways. Consider the case of inclination angle dependent KN properties. One can set up a grid of inclination angles. Better would be to use the probability distribution function of inclination angles for a random isotropic inclination sample, $PDF(i) \propto \sin(i)$. This weights edge on, i.e. red and faint, KN more than a grid is likely to. The inclination angle sample selected by a GW detector network search isn't isotropic. The amplitude of the strain detected is generically described by $PDF(i) = 0.076076(1 + 6\,cos^2(i) + cos^4(i))^{3/2} \sin(i)$, that is, GW observatories prefer inclination angles near 30° (*Schutz*, 2011). For the Bulla models, this could be accounted for by using Bayesian priors on the models. It would be interesting to have a version of the *Setzer et al.* (2022) KN population absolute magnitude distribution weighted by the expected GW network inclination angle distribution. In our work, we use Bayesian model averaging on our calculated detection probabilities. We do not model polar vs equatorial directly, but one could map the appropriate blue and red Bayesian model average into those. Our *red & faint* average absolute magnitude

is about 0.4 mags fainter than the brighter peak of *Setzer et al.* (2022).

Detection efficiency: Our study is for DECam on the Blanco 4m with its 3 sq-degree field of view, covering the 90% credible sky area using real cadences in 2 passes to ensure a confirmation. The simulated search and discovery over LVK skymaps is relatively rare in the literature, but has been done by *Coughlin et al.* (2020) and *Petrov et al.* (2022). As the 1m class telescopes have very large fields of view, up to the ZTF 47 sq-degrees, much more common in the literature is to assume a KN model, usually a GW170817 analog, and ask what exposure time or limiting magnitude is necessary to detect it. If instead of Bayesian model averaging of the detection probability we had used Bayesian model average absolute magnitudes, our study would be very different. The average absolute magnitudes for our *bright & blue*, *reddish & slow*, and *red & faint* models for r-band are $-16.3, -15.2, -14.2$ respectively. In 100 seconds, DECam reaches $r = 23.0$, sufficient to detect $M_r = -15.2$ to 500 Mpc. In 1200 seconds, DECam reaches $r = 24.4$, sufficient to detect $M_r = -14.2$ to 500 Mpc, and GW170817's $M_r = -15.5$ to 1 Gpc. Why then do events at $d_L = 200$ Mpc, have in our study detection probabilities P_d of 90%, 73%, & 60% for the *bright & blue*, *reddish & slow*, and *red & faint* models, respectively, using the *low-TT* strategy, and routinely require 60-90 second exposures for *bright & blue*and 300-1200 second exposures for the last two models? The effect of using eq 5.2 is to extend the search to lower $M_$ej and $\log X_{\rm lan}$ and thus lower luminosities. Our method of accounting for uncertainty in the KN population is driving our results. If we adopt the *Coughlin et al.* (2018) model parameters and uncertainties, as we are likely to do for O4 observations, our detection efficiencies will increase and exposure

times decrease. Using the GW170817 absolute magnitude for detection is likely over-optimistic, as suggested by *Colombo et al.* (2022) placing GW170817 at the 75^{th} percentile bright, and *Setzer et al.* (2022) placing it at 95^{th} percentile bright. The studies using 1m class telescopes are most likely to assume GW170817 analogs, though *Petrov et al.* (2022) uses both that and a lower luminosity, red model, and *Sagués Carracedo et al.* (2021) does a careful analysis of viewing angle dependent models. The studies assuming the Rubin Observatory (*Cowperthwaite et al.*, 2019; *Chen et al.*, 2021), or a variety/network of telescopes (*Coughlin et al.*, 2020; *Chase et al.*, 2022) tend to analyze detection probabilities for lower luminosity events. In summary, one will have to be careful comparing our detection probabilities with others in the literature, which often use a single luminous model or evaluate and average detection efficiencies over a grid of models using a uniform prior. In our language, "chance of finding it" in Fig 5.3 is to be interpreted as "fraction of models detected given our priors on the space of models".

5.6.1 Applicability to NSBH and mass gap events

For standard siren studies, NSBH mergers are just as valuable as BNS mergers, as long as they produce electromagnetic counterparts. NSBH merger events have higher distances for similar SNR than BNS mergers, as can be seen in Table 5.6,

The dominant factor for their use in standard siren cosmology is the probability of a KN given a NS-BH merger. No counterpart to a NSBH merger has been detected (e.g. *Morgan et al.* (2020); *Anand et al.* (2020); *Kawaguchi et al.* (2020b)). *Zhu et al.* (2021) argue that no detectable KN counterpart was expected for NSBH mergers in

Table 5.6. LVC GWTC events (O1-O3) containing neutron stars and with $M_2 < 5M\odot$ and SNR$>$ 8.

id	M_1 ($M_\odot$)	M_2 ($M_\odot$)	distance (Mpc)	SNR	class
GW170817	1.5	1.3	40	33	BNS
GW190425	2.0	1.4	160	13	BNS
–					
GW190814	23.2	2.6	240	22	BH-NS
GW200105_162426*	9.0	1.9	270	14	BH-NS
GW200115_042309	5.9	1.4	290	11	BH-NS
GW190426_152155	5.7	1.5	370	10	BH-NS
GW191219_163120	31.1	1.2	550	9	BH-NS
GW190917_114630	9.3	2.1	720	10	BH-NS
GW200210_092254	24.1	2.8	940	8	BH-NS

Note. — SNR is the matched filter SNR. GW200105_162426* has $p_{\rm astro} = 0.3$ is thus considered a marginal candidate. Only 2 events have a 90% confidence sky area of $<$ 30 sq-deg, 2 at $<$ 300 sq-deg, and 3 at $<$ 400 sq-deg. The median sky area is 1700 sq-deg. Data from `https://www.gw-openscience.org/eventapi/html/allevents/`

O3. *Kawaguchi et al.* (2020a) and *Darbha et al.* (2021) study the brightness of KN from NSBH mergers, and *Drozda et al.* (2020) does the same for mass-gap objects. The summary is that only a fraction of NSBH events will produce KN, primarily those mergers with low mass ratios and high spin.

The *Kawaguchi et al.* (2020a) models have absolute magnitudes that peak for r, i at -14.5, -15.0 respectively. There is a spread of about 1 magnitude fainter in the i-band absolute magnitude, going fainter as the binary mass ratio increases and the effective spin gets smaller. Our *red & faint* model has an i-band absolute magnitude of -14.5, midway through the range of *Kawaguchi et al.* (2020a). *Petrov et al.* (2022) adopt the *Bulla* (2019) models, broken into BNS and NSBH models both optimistic ($M_{\rm ej} = 0.05, 0.08$) and conservative ($M_{\rm ej} = 0.01, 0.01$). The optimistic BNS model has an absolute magnitude in the r-band of -16.0, the conservative NSBH model of -14.8; these correspond well to our *bright & blue* and *red & faint* models, respectively. Taking our *red & faint* model as appropriate for dynamical ejecta dominated NSBH mergers, our *low-TT* strategy has 50% detection probability out to 330 Mpc (see Figure 5.3). Our strategies are sufficient to obtain the majority of NSBH events that have EM counterparts if they are at distances $\leq$ 330 Mpc.

5.6.2 Blanco/DECam and Rubin LSST

It is of interest to compare the strategies defined here with the program outlined in *Chen et al.* (2021). They assume inclination independence and a GW170817-like KN and argue for two filter observations. The program conservatively assumes 30% of A+ events by dedicating 7 hours of Rubin Observatory time in 30s exposures,

capturing 12/year. Our expectation is that the Rubin ToO program will use 3% of the available LSST time, so on the order of 100 hours which can pursue all BNS events in LVK O4 assuming 1/month and 8 hours per event, so pursuing light curves. Alternatively and more likely, Rubin will choose to observe the 50% best events by sky area in both the BNS and the NSBH categories. In this scenario, a good use of DECam/Blanco would be to follow-up the others that have sky area < 300 sq-degrees. Table 5.5 suggests this would be viable.

In fact, if the results of *Petrov et al.* (2022) hold, then there will be many merger events containing NS that have sky areas greater than 300 sq-degrees; our simulations would have to be extended by another ~ 360 events all with sky area > 300 sq-degrees to match their statistics. For the bright siren cosmology, every NS event is important. We demonstrate here that the Blanco/DECam especially in combination with the Zwicky observatory and its counterparts PS1, OAJ, LS4, are capable of following up the sources with sky area < 300 sq-degrees. The optimal use of the Vera C. Rubin Observatory, with its immense etendue, is to follow up the LVK sources with > 300 sq-degrees. The combination of sky coverage and depth is unmatched. *Petrov et al.* (2022) predicts the median sky coverage for BNS events in O4 is 1820^{+190}_{-170} sq-degrees and the median luminosity distance is 352 ± 10 sq-degrees, and the NSBH median distance further away. For the Rubin FoV of 9.6 sq-degrees, the number of exposures to cover the sky area once is ≈ 200, which at 100 second exposures can be done in less than 6 hours, assuming a *reddish & slow* model and 1.2 mags deeper m_0 for Eq. 5.1. Likely one could build a two-visit strategy that would take 10 hours per event, allowing Rubin to follow up 10 additional events per year without light curves. The

Rubin time-domain ecosystem of data, brokers, and routine spectroscopic follow-up is likely to minimize positives, though perhaps not until after O4.

As discussed in *Morgan et al.* (2020); *Garcia et al.* (2020); *Tucker et al.* (2022), the need for coordination with spectroscopic telescopes is vital in identifying the true counterpart. Given there has only been one confirmed optical counterpart, there is uncertainty in the expected light curve from photometric data.

5.7 Conclusion

In this chapter, we create families of observing strategies that optimize the probability of detecting a KN within DECam's images. We examine various filter choices, depths, area coverage, and cadence of observations in order to ensure optimal chance of detection. Given the expanded range of sensitivity in future LVK observing runs, deeper exposures will be necessary in order to be sensitive to the quickly fading counterpart. As we do not have unlimited time for such follow ups, we examine how we can optimize our chance of detection while taking into account real world constraints.

We chose to optimize our strategies based on the probability of detecting the KN within two images that are at least 30 min apart. This constraint is put in place in order to help eliminate asteroids and other sources of noise. We explore two different types of observing scenarios. The first is a homogeneous covering of the sky area with a single exposure time, and the second uses deeper exposures in the higher probability sky areas and shallower exposures on the rest of the area. We then categorize our strategies by observational constraint, where each family of

strategies is taken from the top 10% or 5% of *Top* strategies. The *Top* strategies use all available resources and are useful as a benchmark for the full detection capability of the DECam.

Examining each of the realistic observing scenarios, we find we can achieve $\sim$ 75% to 80% probability of detection out to 190 Mpc (the nominal limit of LVK BNS range) for a wide range of KN parameters (*reddish & slow*), $\sim$ 65% for a fainter and redder KN (*red & faint*) and over 90% for a *bright & blue* model along the full range of distances limited to 330Mpc. Additionally, we provide the mean detection probability and total telescope time required for detection and confirmation in each KN model for a given range of GW event area and distance in figure 5.5. In particular, this plot might be used as a guide on how likely it is to succeed in KN detection of specific future events considering a trade-off between time budget and optimal chances.

While DECam will continue to be the optimal camera in the southern hemisphere during the next observing run, the efforts to detect the next KN optical counterpart will be greatly aided by other telescopes that are planned to be online during this time. For example, the expected addition of the Simonyi Telescope at the Vera Rubin Observatory.

CHAPTER VI

Conclusion

DES is one of the first collaborations to contribute to the new field of gravitational wave multi-messenger astrophysics. After the success of being one of the first teams to discover the kilonova associated with BNS gravitational wave event, GW170817, the DESGW search and discovery team worked to improve the program used for the LVC's third observing run. This thesis describes those improvements and some of the results enabled by them. This conclusion chapter summarizes the core results of the thesis and its implications. Because this work is part of a collaborative project, I also include a description of my specific contributions to each of the main chapters.

To prepare for O3, I primarily lead the efforts to update the observing strategy and the image processing pipeline, and trained a team of observers to help perform follow up campaigns, as discussed in Chapter II. More specifically, I implemented updates to the pipeline that enabled it to run image processing on a CCD by CCD basis in parallel, as opposed to completing each step per image before moving on to the next. This was crucial to reduce the time required to produce our lists of EM

candidates. After image processing has been completed, the images go through post-processing, in which the sources found in each CCD are evaluated based on a machine learning score and matched with the nearest potential host galaxy. This process is the beginning of candidate reduction. I additionally integrated the use of web pages displaying the observational information about each candidate. These changes were critical for the by eye examinations of the final candidates before publishing them to the GCN.

Throughout O3, the DESGW team used this pipeline to follow up 4 candidate GW events. Of those events, two were of particular significance. The first such candidate was S190510g. This event was initially classified as likely to originate from a BNS merger with a 50% confidence sky area of only 31 $\deg^2$. For this reason, a follow up campaign was initiated. After a full night of imaging, LVC published an update indicating the event was likely to be terrestrial in nature. Despite this, we continued with our analysis of the data, as discussed in Chapter III. I led a first-of-its-kind study of the efficiency of detecting a KN within DECam images. Within this analysis, we simulated KN lightcurves taking into account the actual sky conditions on the night of observations. Using the physical parameters of GW170817 for the KN model, we found that if a KN were present in our observations, we would have had a 99% chance of being able to detect the counterpart in our images. We also showed that this efficiency is not uniform across all KN models.

The same principles were applied to the analysis of event GW190814 (Chapter IV). This event was the first high confidence event likely to be a black hole neutron star merger. In this follow-up campaign, we took images for 6 nights over the first

16 nights following the merger. All candidates produced by the DESGW search and discovery pipeline were eventually excluded based on light curve properties, photometric redshifts of the host galaxies, or machine learning classification. Similar to the search efficiency analysis performed for S190510g, here we took the analysis one step further to put the first observational limits on a BHNS optical counterpart. The non-detection of an optical transient implies that a potential counterpart will have ejecta mass $< 0.07\ M_{\odot}$, ejecta velocity <0.18c or >0.21c, and lanthanide fraction $> 10^{-8.56}$ at the 2σ confidence level. In this analysis, I ran the follow up campaign for the event (16 nights, including day-time planning, night-time observations, image processing and post-processing) and applied the analysis techniques used in Chapter III. Additionally, I collaborated closely with R. Morgan in the design and implementation of our refined candidate selection process.

Each of these analyses enabled us to characterize the typical light curves of kilonovae that would appear in our observations and forecast the sensitivity of follow-ups going forward. Using this information, we once again updated our methodology for determining the observing plans for future searches. With the new method, described in Chapter V, we created families of observing strategies that optimize the probability of detecting a KN within DECam observations. We also explored the benefits of taking deeper observations versus ensuring we cover the full sky localization area, the impact of using various filters, and the impact of using varying exposure times when covering the sky area. Using realistic observing scenarios, we found that we have up to 80% probability of detecting a wide range of potential KN light curves out to the nominal limit of the LVK BNS range of 190Mpc. This is an improve-

ment of about a factor of 2 over the O3 strategy performance and bodes well for new multi-messenger discoveries that will enable competitive measurements of the Hubble constant in the future. For this analysis, my contribution was primarily in the design and specification of the various observing strategies, based on my detailed experience in O3. I additionally took this project as an opportunity to train new members of the DESGW team, including C. De Bom, on the details of the search strategy decision workflow. This training is crucial for the success of the team in O4 and beyond.

The results of this thesis have multiple implications for future work in astrophysics and cosmology. For example, examining how the combination of GW data with existing DES cosmological probes affects various cosmological parameters will be an interesting future study. Outside of cosmology, detected EM counterparts of neutron stars can shed light on the question of the neutron star equation of state by measuring the amount of ejected matter and combining that information with the mass ratio and total mass of the merger (*Pérez-García et al.*, 2022; *Bauswein et al.*, 2013). The supernova community is also likely to benefit from this work. As mentioned throughout this thesis, the primary background for our searches are supernovae. There is, thus, a serendipitous relationship between kilonova searches and supernova discovery programs as mining of our background data could lead to the discovery of many supernovae.

In sum, this thesis is a novel contribution to the emerging field of multi-messenger cosmology. It propels the field forward by tackling the observational challenges of making new discoveries of faint and short-lived EM counterparts to GW events within

large localization areas. We took the previously established program and made it more sensitive and rigorous. We optimized the search strategy and image processing pipeline. We also improved the analysis framework, publishing the first limits on the physical properties of a merging compact binary system based on a comprehensive analysis of candidates in our search data. As a result, future searches will likely yield many more discoveries to fully realize the potential of gravitational waves for cosmology.

Bibliography

Aasi, J., et al. (2015), Advanced LIGO, *Classical and Quantum Gravity*, *32*(7), 074,001, doi:10.1088/0264-9381/32/7/074001.

Abbott, B. P., et al. (2016), Observation of Gravitational Waves from a Binary Black Hole Merger, *Phys. Rev. Lett.*, *116*(6), 061102, doi:10.1103/PhysRevLett.116.061102.

Abbott, B. P., et al. (2017), A gravitational-wave standard siren measurement of the Hubble constant, *Nature*, *551*(7678), 85–88, doi:10.1038/nature24471.

Abbott, B. P., et al. (2017a), Gw170817: observation of gravitational waves from a binary neutron star inspiral, *Physical review letters*, *119*(16), 161,101.

Abbott, B. P., et al. (2017b), Multi-messenger observations of a binary neutron star merger, *Astrophys. J. Lett*, *848*(2), L12.

Abbott, B. P., et al. (2018), Prospects for observing and localizing gravitational-wave transients with advanced ligo, advanced virgo and kagra, *Living Reviews in Relativity*, *21*(1), 3.

Abbott, B. P., et al. (2019), GWTC-1: A Gravitational-Wave Transient Catalog of Compact Binary Mergers Observed by LIGO and Virgo during the First and Second Observing Runs, *Physical Review X*, *9*(3), 031040, doi:10.1103/PhysRevX.9.031040.

Abbott, B. P., et al. (2020a), Prospects for observing and localizing gravitational-wave transients with advanced LIGO, advanced virgo and KAGRA, *Living Reviews in Relativity*, *23*(1), doi:10.1007/s41114-020-00026-9.

Abbott, R., et al. (2020b), GW190814: Gravitational waves from the coalescence of a 23 solar mass black hole with a 2.6 solar mass compact object, *The Astrophysical Journal*, *896*(2), L44, doi:10.3847/2041-8213/ab960f.

Abbott, R., et al. (2021), Observation of Gravitational Waves from Two Neutron Star-Black Hole Coalescences, *ApJ*, *915*(1), L5, doi:10.3847/2041-8213/ac082e.

Abbott, R., et al. (2021), Population of merging compact binaries inferred using gravitational waves through GWTC-3, *Phys. Rev. X*.

Abbott, T. M. C., et al. (2018), The Dark Energy Survey: Data Release 1, *ApJS*, *239*(2), 18, doi:10.3847/1538-4365/aae9f0.

Abbott, T. M. C., et al. (2021), The Dark Energy Survey Data Release 2, *ApJS*, *255*(2), 20, doi:10.3847/1538-4365/ac00b3.

Abbott, T. M. C., et al. (2022), Dark Energy Survey Year 3 results: Cosmological constraints from galaxy clustering and weak lensing, *Phys. Rev. D*, *105*(2), 023520, doi:10.1103/PhysRevD.105.023520.

Abdalla, E., et al. (2022), Cosmology intertwined: A review of the particle physics, astrophysics, and cosmology associated with the cosmological tensions and anomalies, *Journal of High Energy Astrophysics*, *34*, 49–211, doi:10.1016/j.jheap.2022.04.002.

Ackley, K., et al. (2020).

Aiola, S., et al. (2020), The Atacama Cosmology Telescope: DR4 maps and cosmological parameters, , *2020*(12), 047, doi:10.1088/1475-7516/2020/12/047.

Akutsu, T., et al. (2021), Overview of KAGRA: Detector design and construction history, *Progress of Theoretical and Experimental Physics*, *2021*(5), 05A101, doi:10.1093/ptep/ptaa125.

Albareti, F. D., et al. (2017), The 13th Data Release of the Sloan Digital Sky Survey: First Spectroscopic Data from the SDSS-IV Survey Mapping Nearby Galaxies at Apache Point Observatory, *ApJS*, *233*(2), 25, doi:10.3847/1538-4365/aa8992.

Anand, S., et al. (2020), Optical follow-up of the neutron star–black hole mergers s200105ae and s200115j, *Nature Astronomy*, *5*(1), 46–53, doi:10.1038/s41550-020-1183-3.

Andreoni, I., et al. (2017), Follow up of gw170817 and its electromagnetic counterpart by australian-led observing programmes, *Publications of the Astronomical Society of Australia*, *34*.

Andreoni, I., et al. (2019), LIGO/Virgo S190510g: Optical Counterpart Candidates from DECam-GROWTH., *GRB Coordinates Network*, *24467*, 1.

Andreoni, I., et al. (2019a), Growth on s190510g: Decam observation planning and follow-up of a distant binary neutron star merger candidate, *The Astrophysical Journal*, *881*(1), L16, doi:10.3847/2041-8213/ab3399.

Andreoni, I., et al. (2019b), Growth on s190814bv: Deep synoptic limits on the optical/near-infrared counterpart to a neutron star-black hole merger, *arXiv preprint arXiv:1910.13409*.

Andreoni, I., et al. (2019), GROWTH on S190510g: DECam Observation Planning and Follow-up of a Distant Binary Neutron Star Merger Candidate, *ApJ*, *881*(1), L16, doi:10.3847/2041-8213/ab3399.

Andreoni, I., et al. (2020), GROWTH on s190814bv: Deep synoptic limits on the optical/near-infrared counterpart to a neutron star–black hole merger, *The Astrophysical Journal*, *890*(2), 131, doi:10.3847/1538-4357/ab6a1b.

Annis, J., and M. Soares-Santos (2016), Experimentally, How Dark Are Black Hole Mergers?, *arXiv e-prints*, arXiv:1609.09517, doi:10.48550/arXiv.1609.09517.

Annis, J., K. Herner, and M. Soares-Santos (2019), *GCN Circ. 25458*.

Barbieri, Salafia, O. S., Perego, A., Colpi, M., and Ghirlanda, G. (2019), Light-curve models of black hole - neutron star mergers: steps towards a multi-messenger parameter estimation, *A&A*, *625*, A152, doi:10.1051/0004-6361/201935443.

Barnes, J., and D. Kasen (2013), Effect of a High Opacity on the Light Curves of Radioactively Powered Transients from Compact Object Mergers, *ApJ*, *775*(1), 18, doi:10.1088/0004-637X/775/1/18.

Bauswein, A., S. Goriely, and H. T. Janka (2013), Systematics of Dynamical Mass Ejection, Nucleosynthesis, and Radioactively Powered Electromagnetic Signals from Neutron-star Mergers, *ApJ*, *773*(1), 78, doi:10.1088/0004-637X/773/1/78.

Bauswein, A., S. Goriely, and H.-T. Janka (2013), Systematics of dynamical mass ejection, nucleosynthesis, and radioactively powered electromagnetic signals from neutron-star mergers, *The Astrophysical Journal*, *773*(1), 78, doi: 10.1088/0004-637x/773/1/78.

Becker, A. (2015), HOTPANTS: High Order Transform of PSF ANd Template Subtraction, Astrophysics Source Code Library, record ascl:1504.004.

Bernstein, G., et al. (2017), Instrumental response model and detrending for the dark energy camera, *Publications of the Astronomical Society of the Pacific*, *129*(981), 114,502.

Bernstein, G. M., et al. (2018), Photometric Characterization of the Dark Energy Camera, *Publications of the Astronomical Society of the Pacific*, *130*, 054,501, doi:10.1088/1538-3873/aaa753.

Bertin, E. (2006), *Automatic Astrometric and Photometric Calibration with SCAMP*, *Astron. Soc. Pac. Conf. Ser.*, vol. 351, p. 112.

Bertin, E. (2011), Automated Morphometry with SExtractor and PSFEx, in *Astronomical Data Analysis Software and Systems XX*, *Astronomical Society of the Pacific Conference Series*, vol. 442, edited by I. N. Evans, A. Accomazzi, D. J. Mink, and A. H. Rots, p. 435.

Bilicki, M., T. H. Jarrett, J. A. Peacock, et al. (2014), Two Micron All Sky Survey Photometric Redshift Catalog: A Comprehensive Three-dimensional Census of the Whole Sky, *ApJS*, *210*(1), 9, doi:10.1088/0067-0049/210/1/9.

Bloom, J. S., et al. (2006), Closing in on a short-hard burst progenitor: Constraints from early-time optical imaging and spectroscopy of a possible host galaxy of GRB 050509b, *The Astrophysical Journal*, *638*(1), 354–368, doi:10.1086/498107.

Bom, C. R., et al. (2023), Designing an Optimal Kilonova Search using DECam for Gravitational Wave Events, *arXiv e-prints*, arXiv:2302.04878, doi:10.48550/arXiv.2302.04878.

Breiman, L. (2001), Random forests, *Machine Learning*, *45*(1), 5–32, doi:10.1023/A:1010933404324.

Bulla, M. (2019), POSSIS: predicting spectra, light curves, and polarization for multidimensional models of supernovae and kilonovae, *MNRAS*, *489*(4), 5037–5045, doi:10.1093/mnras/stz2495.

Bulla, M. (2019), possis: predicting spectra, light curves, and polarization for multidimensional models of supernovae and kilonovae, *Monthly Notices of the Royal Astronomical Society*, *489*(4), 5037–5045, doi:10.1093/mnras/stz2495.

Buonanno, A., B. R. Iyer, E. Ochsner, Y. Pan, and B. S. Sathyaprakash (2009), Comparison of post-newtonian templates for compact binary inspiral signals in gravitational-wave detectors, *Physical Review D*, *80*(8), doi:10.1103/physrevd.80.084043.

Capano, C. D., I. Tews, S. M. Brown, B. Margalit, S. De, S. Kumar, D. A. Brown, B. Krishnan, and S. Reddy (2020), Stringent constraints on neutron-star radii from

multimessenger observations and nuclear theory, *Nature Astronomy*, doi:10.1038/s41550-020-1014-6.

Cardelli, J. A., G. C. Clayton, and J. S. Mathis (1989), The Relationship between Infrared, Optical, and Ultraviolet Extinction, *ApJ*, *345*, 245, doi:10.1086/167900.

Caron, B., et al. (1999), The virgo interferometer, *Classical and Quantum Gravity*, *14*, 1461, doi:10.1088/0264-9381/14/6/011.

Cartier, R., et al. (2019), *GCN Circ. 25784*.

Chase, E. A., et al. (2022), Kilonova Detectability with Wide-field Instruments, *ApJ*, *927*(2), 163, doi:10.3847/1538-4357/ac3d25.

Chen, H.-Y., and D. E. Holz (2014), The Loudest Gravitational Wave Events, *arXiv e-prints*.

Chen, H.-Y., M. Fishbach, and D. E. Holz (2018), A two per cent Hubble constant measurement from standard sirens within five years, *Nature*, *562*(7728), 545–547, doi:10.1038/s41586-018-0606-0.

Chen, H.-Y., P. S. Cowperthwaite, B. D. Metzger, and E. Berger (2021), A Program for Multimessenger Standard Siren Cosmology in the Era of LIGO A+, Rubin Observatory, and Beyond, *ApJ*, *908*(1), L4, doi:10.3847/2041-8213/abdab0.

Colombo, A., O. S. Salafia, F. Gabrielli, G. Ghirlanda, B. Giacomazzo, A. Perego, and M. Colpi (2022), Multi-messenger Observations of Binary Neutron Star Mergers in the O4 Run, *ApJ*, *937*(2), 79, doi:10.3847/1538-4357/ac8d00.

Coughlin, M. W. (2020), Lessons from counterpart searches in ligo and virgo's third observing campaign, *Nature Astronomy*, *4*(6), 550–552, doi:10.1038/s41550-020-1130-3.

Coughlin, M. W., T. Dietrich, S. Antier, M. Bulla, F. Foucart, K. Hotokezaka, G. Raaijmakers, T. Hinderer, and S. Nissanke (2019), Implications of the search for optical counterparts during the first six months of the Advanced LIGO's and Advanced Virgo's third observing run: possible limits on the ejecta mass and binary properties, *Monthly Notices of the Royal Astronomical Society*, *492*(1), 863–876, doi:10.1093/mnras/stz3457.

Coughlin, M. W., T. Dietrich, B. Margalit, and B. D. Metzger (2019), Multimessenger Bayesian parameter inference of a binary neutron star merger, *MNRAS*, *489*(1), L91–L96, doi:10.1093/mnrasl/slz133.

Coughlin, M. W., et al. (2018), Constraints on the neutron star equation of state from AT2017gfo using radiative transfer simulations, *MNRAS*, *480*(3), 3871–3878, doi:10.1093/mnras/sty2174.

Coughlin, M. W., et al. (2020), Implications of the search for optical counterparts during the second part of the Advanced LIGO's and Advanced Virgo's third observing run: lessons learned for future follow-up observations, *MNRAS*, *497*(1), 1181–1196, doi:10.1093/mnras/staa1925.

Coulter, D., et al. (2017), Swope supernova survey 2017a (sss17a), the optical counterpart to a gravitational wave source, *Science*, *358*(6370), 1556–1558.

Cowperthwaite, P., et al. (2017), The electromagnetic counterpart of the binary neutron star merger ligo/virgo gw170817. ii. uv, optical, and near-infrared light curves and comparison to kilonova models, *The Astrophysical Journal Letters*, *848*(2), L17.

Cowperthwaite, P. S., and E. Berger (2015), A Comprehensive Study of Detectability and Contamination in Deep Rapid Optical Searches for Gravitational Wave Counterparts, *ApJ*, *814*(1), 25, doi:10.1088/0004-637X/814/1/25.

Cowperthwaite, P. S., V. A. Villar, D. M. Scolnic, and E. Berger (2019), LSST Target-of-opportunity Observations of Gravitational-wave Events: Essential and Efficient, *ApJ*, *874*(1), 88, doi:10.3847/1538-4357/ab07b6.

Cowperthwaite, P. S., et al. (2017), The Electromagnetic Counterpart of the Binary Neutron Star Merger LIGO/Virgo GW170817. II. UV, Optical, and Near-infrared Light Curves and Comparison to Kilonova Models, *ApJ*, *848*(2), L17, doi:10.3847/2041-8213/aa8fc7.

Darbha, S., and D. Kasen (2020), Inclination Dependence of Kilonova Light Curves from Globally Aspherical Geometries, *ApJ*, *897*(2), 150, doi:10.3847/1538-4357/ab9a34.

Darbha, S., D. Kasen, F. Foucart, and D. J. Price (2021), Electromagnetic Signatures from the Tidal Tail of a Black Hole-Neutron Star Merger, *ApJ*, *915*(1), 69, doi:10.3847/1538-4357/abff5d.

Dark Energy Survey Collaboration, et al. (2016), The Dark Energy Survey: more

than dark energy - an overview, *MNRAS*, *460*(2), 1270–1299, doi:10.1093/mnras/stw641.

De, K., et al. (2020), The zwicky transient facility census of the local universe i: Systematic search for calcium rich gap transients reveal three related spectroscopic sub-classes.

De Vicente, J., E. Sánchez, and I. Sevilla-Noarbe (2016), DNF - Galaxy photometric redshift by Directional Neighbourhood Fitting, *MNRAS*, *459*, 3078–3088, doi:10.1093/mnras/stw857.

DES Collaboration (2018), First Cosmology Results using Type Ia Supernovae from the Dark Energy Survey: Constraints on Cosmological Parameters, *ApJ*, *872*(2), L30, doi:10.3847/2041-8213/ab04fa.

Dhawan, S., M. Bulla, A. Goobar, A. Sagués Carracedo, and C. N. Setzer (2020), Constraining the observer angle of the kilonova at2017gfo associated with gw170817: Implications for the hubble constant, *The Astrophysical Journal*, *888*(2), 67, doi:10.3847/1538-4357/ab5799.

Dietrich, T., and M. Ujevic (2017), Modeling dynamical ejecta from binary neutron star mergers and implications for electromagnetic counterparts, *Classical and Quantum Gravity*, *34*(10), 105014, doi:10.1088/1361-6382/aa6bb0.

Dietrich, T., M. W. Coughlin, P. T. H. Pang, M. Bulla, J. Heinzel, L. Issa, I. Tews, and S. Antier (2020), New constraints on the supranuclear equation of state and the hubble constant from nuclear physics – multi-messenger astronomy.

Dilday, B., et al. (2008), A measurement of the rate of type ia supernovae at redshiftz≈ 0.1 from the first season of the SDSS-II supernova survey, *The Astrophysical Journal*, *682*(1), 262–282, doi:10.1086/587733.

Doctor, Z., et al. (2017), A search for kilonovae in the dark energy survey, *The Astrophysical Journal*, *837*(1), 57, doi:10.3847/1538-4357/aa5d09.

Drout, M. R., et al. (2017), Light curves of the neutron star merger gw170817/sss17a: Implications for r-process nucleosynthesis, *Science*, *358*(6370), 1570–1574, doi:10.1126/science.aaq0049.

Drozda, P., K. Belczynski, R. O'Shaughnessy, T. Bulik, and C. L. Fryer (2020), Black hole - neutron star mergers: the first mass gap and kilonovae, *arXiv e-prints*.

Dutcher, D., et al. (2021), Measurements of the E -mode polarization and temperature-E -mode correlation of the CMB from SPT-3G 2018 data, *Phys. Rev. D*, *104*(2), 022003, doi:10.1103/PhysRevD.104.022003.

Eddington, A. S. (1917), The pulsation theory of Cepheid variables, *The Observatory*, *40*, 290–293.

Eichler, D., M. Livio, T. Piran, and D. N. Schramm (1989), Nucleosynthesis, neutrino bursts and γ-rays from coalescing neutron stars, *Nature*, *340*(6229), 126–128, doi:10.1038/340126a0.

Einstein, A. (1916), Die Grundlage der allgemeinen Relativitätstheorie, *Annalen der Physik*, *354*(7), 769–822, doi:10.1002/andp.19163540702.

Evans, P., et al. (2017), Swift and nustar observations of gw170817: detection of a blue kilonova, *Science*, *358*(6370), 1565–1570.

Evans, P. A., et al. (2019), LIGO/Virgo S190510g: Swift-XRT observations and results., *GRB Coordinates Network*, *24541*, 1.

Feindt, U., J. Nordin, M. Rigault, V. Brinnel, S. Dhawan, A. Goobar, and M. Kowalski (2019), simsurvey: estimating transient discovery rates for the zwicky transient facility, *Journal of Cosmology and Astroparticle Physics*, *2019*(10), 005–005, doi: 10.1088/1475-7516/2019/10/005.

Finn, L. S., and D. F. Chernoff (1993), Observing binary inspiral in gravitational radiation: One interferometer, *Phys. Rev. D*, *47*(6), 2198–2219, doi: 10.1103/PhysRevD.47.2198.

Flaugher, B., et al. (2015), The Dark Energy Camera, *AJ*, *150*(5), 150, doi:10.1088/0004-6256/150/5/150.

Foucart, F., T. Hinderer, and S. Nissanke (2018), Remnant baryon mass in neutron star-black hole mergers: Predictions for binary neutron star mimickers and rapidly spinning black holes, *Phys. Rev. D*, *98*, 081,501, doi:10.1103/PhysRevD.98.081501.

Foucart, F., M. D. Duez, L. E. Kidder, S. M. Nissanke, H. P. Pfeiffer, and M. A. Scheel (2019), Numerical simulations of neutron star-black hole binaries in the near-equal-mass regime, *Phys. Rev. D*, *99*, 103,025, doi:10.1103/PhysRevD.99.103025.

Gaia Collaboration, et al. (2018), Gaia Data Release 2. Summary of the contents and survey properties, *A&A*, *616*, A1, doi:10.1051/0004-6361/201833051.

Garcia, A., et al. (2020), A DESGW Search for the Electromagnetic Counterpart to the LIGO/Virgo Gravitational-wave Binary Neutron Star Merger Candidate S190510g, *ApJ*, *903*(1), 75, doi:10.3847/1538-4357/abb823.

Garcia, A., et al. (2020), A desgw search for the electromagnetic counterpart to the ligo/virgo gravitational wave binary neutron star merger candidate s190510g.

Gillanders, J. H., S. J. Smartt, S. A. Sim, A. Bauswein, and S. Goriely (2022), Modelling the spectra of the kilonova AT2017gfo – I: The photospheric epochs, *arXiv e-prints*.

Goldstein, D. A., et al. (2015), Automated Transient Identification in the Dark Energy Survey, *AJ*, *150*(3), 82, doi:10.1088/0004-6256/150/3/82.

Goldstein, D. A., et al. (2019), Growth on s190426c: Real-time search for a counterpart to the probable neutron star–black hole merger using an automated difference imaging pipeline for decam, *The Astrophysical Journal*, *881*(1), L7, doi:10.3847/2041-8213/ab3046.

Gomez, S., et al. (2019), LIGO/Virgo S190510g: Spectroscopic Classification of DECam-GROWTH and DES-GW Candidate DG19fqqk/desgw-190510c with Magellan., *GRB Coordinates Network*, *24511*, 1.

Gomez, S., et al. (2019), A galaxy-targeted search for the optical counterpart of the candidate NS–BH merger s190814bv with magellan, *The Astrophysical Journal*, *884*(2), L55, doi:10.3847/2041-8213/ab4ad5.

Górski, K. M., E. Hivon, A. J. Banday, B. D. Wandelt, F. K. Hansen, M. Reinecke, and M. Bartelmann (2005), HEALPix: A Framework for High-Resolution Discretization and Fast Analysis of Data Distributed on the Sphere, *ApJ*, *622*(2), 759–771, doi:10.1086/427976.

Graham, M. J., et al. (2020), Candidate Electromagnetic Counterpart to the Binary Black Hole Merger Gravitational-Wave Event S190521g*, *Phys. Rev. Lett.*, *124*(25), 251102, doi:10.1103/PhysRevLett.124.251102.

Greisen, E. W., and M. R. Calabretta (2002), Representations of world coordinates in FITS, *A&A*, *395*, 1061–1075, doi:10.1051/0004-6361:20021326.

Grossman, D., O. Korobkin, S. Rosswog, and T. Piran (2014), The long-term evolution of neutron star merger remnants - II. Radioactively powered transients, *MNRAS*, *439*, 757–770, doi:10.1093/mnras/stt2503.

Guy, et al. (2010), The supernova legacy survey 3-year sample: Type ia supernovae photometric distances and cosmological constraints, *A&A*, *523*, A7.

Heaviside, O. (1893), A gravitational and electromagnetic analogy, *The Electrician*.

Herner, K., M. Soares-Santos, J. Annis, and A. Palmese (2019a), *GCN Circ. 25495*.

Herner, K., et al. (2019b), *GCN Circ. 25373*.

Herner, K., et al. (2019c), *GCN Circ. 25398*.

Herner, K., et al. (2020a), Optical follow-up of gravitational wave triggers with DECam during the first two LIGO/VIRGO observing runs, *Astronomy and Computing*, *33*, 100425, doi:10.1016/j.ascom.2020.100425.

Herner, K., et al. (2020b), The updated DESGW processing pipeline for the third LIGO/VIRGO observing run, in *European Physical Journal Web of Conferences*, *European Physical Journal Web of Conferences*, vol. 245, p. 01008, doi:10.1051/epjconf/202024501008.

Hillebrandt, W., and J. C. Niemeyer (2000), Type ia supernova explosion models, *Annual Review of Astronomy and Astrophysics*, *38*(1), 191–230, doi:10.1146/annurev.astro.38.1.191.

Holz, D. E., and S. A. Hughes (2005), Using Gravitational-Wave Standard Sirens, *ApJ*, *629*(1), 15–22, doi:10.1086/431341.

Hotokezaka, K., and E. Nakar (2020), Radioactive Heating Rate of r-process Elements and Macronova Light Curve, *ApJ*, *891*(2), 152, doi:10.3847/1538-4357/ab6a98.

Hu, J.-P., and F.-Y. Wang (2023), Hubble tension: The evidence of new physics, *Universe*, *9*(2), 94.

Hu, L., et al. (2017), Optical observations of ligo source gw 170817 by the antarctic survey telescopes at dome a, antarctica, *Science bulletin*, *62*(21), 1433–1438.

Im, M., et al. (2019a), LIGO/Virgo S190510g: KMTNet observation of DECam-GROWTH and DESGW candidates., *GRB Coordinates Network*, *24493*, 1.

Im, M., et al. (2019b), LIGO/Virgo S190510g: Further KMTNet observation of DECam-GROWTH and DESGW candidates., *GRB Coordinates Network*, *24529*, 1.

Jones, D. O., et al. (2018), Measuring dark energy properties with photometrically classified pan-starrs supernovae. ii. cosmological parameters, *The Astrophysical Journal*, *857*(1), 51, doi:10.3847/1538-4357/aab6b1.

Kasen, D., R. Fernández, and B. D. Metzger (2015), Kilonova light curves from the disc wind outflows of compact object mergers, *MNRAS*, *450*(2), 1777–1786, doi:10.1093/mnras/stv721.

Kasen, D., B. Metzger, J. Barnes, E. Quataert, and E. Ramirez-Ruiz (2017), Origin of the heavy elements in binary neutron-star mergers from a gravitational-wave event, *Nature*, *551*(7678), 80–84, doi:10.1038/nature24453.

Kasliwal, M., et al. (2017), Illuminating gravitational waves: A concordant picture of photons from a neutron star merger, *Science*, *358*(6370), 1559–1565.

Kasliwal, M. M., et al. (2020), Kilonova luminosity function constraints based on zwicky transient facility searches for 13 neutron star mergers.

Kawaguchi, K., M. Shibata, and M. Tanaka (2020a), Diversity of Kilonova Light Curves, *ApJ*, *889*(2), 171, doi:10.3847/1538-4357/ab61f6.

Kawaguchi, K., M. Shibata, and M. Tanaka (2020b), Constraint on the Ejecta Mass for Black Hole-Neutron Star Merger Event Candidate S190814bv, *ApJ*, *893*(2), 153, doi:10.3847/1538-4357/ab8309.

Kessler, R., J. Marriner, M. Childress, et al. (2015), The Difference Imaging Pipeline for the Transient Search in the Dark Energy Survey, *AJ*, *150*, 172, doi:10.1088/0004-6256/150/6/172.

Kessler, R., et al. (2009), SNANA: A Public Software Package for Supernova Analysis, *PASP*, *121*(883), 1028, doi:10.1086/605984.

Kessler, R., et al. (2010), Results from the supernova photometric classification challenge, *Publications of the Astronomical Society of the Pacific*, *122*(898), 1415–1431.

Kessler, R., et al. (2015), The difference imaging pipeline for the transient search in the dark energy survey, *The Astronomical Journal*, *150*(6), 172, doi:10.1088/0004-6256/150/6/172.

Kessler, R., et al. (2019a), First cosmology results using Type Ia supernova from the Dark Energy Survey: simulations to correct supernova distance biases, *MNRAS*, *485*(1), 1171–1187, doi:10.1093/mnras/stz463.

Kessler, R., et al. (2019b), Models and Simulations for the Photometric LSST Astronomical Time Series Classification Challenge (PLAsTiCC), *PASP*, *131*(1003), 094,501, doi:10.1088/1538-3873/ab26f1.

Kessler, R., et al. (2019), Models and simulations for the photometric LSST astronomical time series classification challenge (PLAsTiCC), *Publications of the Astronomical Society of the Pacific*, *131*(1003), 094,501, doi:10.1088/1538-3873/ab26f1.

Kilpatrick, C. D., et al. (2017), Electromagnetic evidence that SSS17a is the result of

a binary neutron star merger, *Science*, *358*(6370), 1583–1587, doi:10.1126/science.aaq0073.

Kilpatrick, C. D., et al. (2021), The gravity collective: A search for the electromagnetic counterpart to the neutron star–black hole merger GW190814, *The Astrophysical Journal*, *923*(2), 258, doi:10.3847/1538-4357/ac23c6.

Korobkin, O., et al. (2020), Axisymmetric radiative transfer models of kilonovae.

Lattimer, J. M. (2019), The Properties of a Black Hole-Neutron Star Merger Candidate, *arXiv:1908.03622 [astro-ph, physics:gr-qc]*, arXiv: 1908.03622.

Lattimer, J. M., and D. N. Schramm (1974), Black-Hole-Neutron-Star Collisions, *ApJ*, *192*, L145, doi:10.1086/181612.

Leavitt, H. S., and E. C. Pickering (1912), Periods of 25 Variable Stars in the Small Magellanic Cloud., *Harvard College Observatory Circular*, *173*, 1–3.

Li, L.-X., and B. Paczyński (1998), Transient Events from Neutron Star Mergers, *ApJ*, *507*(1), L59–L62, doi:10.1086/311680.

Li, W., R. Chornock, J. Leaman, A. V. Filippenko, D. Poznanski, X. Wang, M. Ganeshalingam, and F. Mannucci (2011), Nearby supernova rates from the Lick Observatory Supernova Search – III. The rate–size relation, and the rates as a function of galaxy Hubble type and colour, *Monthly Notices of the Royal Astronomical Society*, *412*(3), 1473–1507, doi:10.1111/j.1365-2966.2011.18162.x.

LIGO Scientific Collaboration (2018), LIGO Algorithm Library - LALSuite, free software (GPL), doi:10.7935/GT1W-FZ16.

LIGO Scientific Collaboration, and VIRGO Collaboration (2019a), LIGO/Virgo S190510g: Identification of a GW compact binary merger candidate., *GRB Coordinates Network*, *24442*, 1.

LIGO Scientific Collaboration, and VIRGO Collaboration (2019b), LIGO/Virgo S190510g: Update on candidate significance., *GRB Coordinates Network*, *24489*, 1.

Lindegren, L., et al. (2018), Gaia Data Release 2. The astrometric solution, *A&A*, *616*, A2, doi:10.1051/0004-6361/201832727.

Littenberg, T. B., B. Farr, S. Coughlin, V. Kalogera, and D. E. Holz (2015), NEUTRON STARS VERSUS BLACK HOLES: PROBING THE MASS GAP WITH LIGO/VIRGO, *The Astrophysical Journal*, *807*(2), L24, doi:10.1088/2041-8205/807/2/l24.

LVC (2019), *GCN Circ. 25333*.

Maoz, D., F. Mannucci, and G. Nelemans (2014), Observational clues to the progenitors of type ia supernovae, *Annual Review of Astronomy and Astrophysics*, *52*(1), 107–170, doi:10.1146/annurev-astro-082812-141031.

McCully, C., et al. (2017), The rapid reddening and featureless optical spectra of the optical counterpart of gw170817, at 2017gfo, during the first four days, *The Astrophysical Journal Letters*, *848*(2), L32.

Metzger, B. D., and E. Berger (2012), What is the Most Promising Electromagnetic

Counterpart of a Neutron Star Binary Merger?, *ApJ*, *746*(1), 48, doi:10.1088/0004-637X/746/1/48.

Metzger, B. D., et al. (2010), Electromagnetic counterparts of compact object mergers powered by the radioactive decay of r-process nuclei, *MNRAS*, *406*(4), 2650–2662, doi:10.1111/j.1365-2966.2010.16864.x.

Morgan, R., et al. (2019), A DECam Search for Explosive Optical Transients Associated with IceCube Neutrino Alerts, *ApJ*, *883*(2), 125, doi:10.3847/1538-4357/ab3a45.

Morgan, R., et al. (2019), A DECam search for explosive optical transients associated with IceCube neutrino alerts, *The Astrophysical Journal*, *883*(2), 125, doi:10.3847/1538-4357/ab3a45.

Morgan, R., et al. (2020), Constraints on the Physical Properties of GW190814 through Simulations Based on DECam Follow-up Observations by the Dark Energy Survey, *ApJ*, *901*(1), 83, doi:10.3847/1538-4357/abafaa.

Morganson, E., et al. (2018), The Dark Energy Survey Image Processing Pipeline, *PASP*, *130*(989), 074,501, doi:10.1088/1538-3873/aab4ef.

Neilsen, E., G. Bernstein, R. Gruendl, and S. Kent (2016), Limiting magnitude, τ, $t_{\rm eff}$, and image quality in des year 1, *Fermilab Technical Notes*, doi:10.2172/1250877.

Nissanke, S., D. E. Holz, S. A. Hughes, N. Dalal, and J. L. Sievers (2010), Exploring

Short Gamma-ray Bursts as Gravitational-wave Standard Sirens, *ApJ*, *725*(1), 496–514, doi:10.1088/0004-637X/725/1/496.

Oates, S. R., et al. (2021), iswift/i/UVOT follow-up of gravitational wave alerts in the o3 era, *Monthly Notices of the Royal Astronomical Society*, *507*(1), 1296–1317, doi:10.1093/mnras/stab2189.

O'Donnell, J. E. (1994), R v-dependent Optical and Near-Ultraviolet Extinction, *ApJ*, *422*, 158, doi:10.1086/173713.

Palmese, A., J. Annis, and M. Soares-Santos (2019), *GCN Circ. 25468*.

Palmese, A., M. Fishbach, C. J. Burke, J. Annis, and X. Liu (2021), Do ligo/virgo black hole mergers produce agn flares? the case of gw190521 and prospects for reaching a confident association, *The Astrophysical Journal Letters*, *914*(2), L34, doi:10.3847/2041-8213/ac0883.

Palmese, A., et al. (2019), Gravitational wave cosmology and astrophysics with large spectroscopic galaxy surveys, *BAAS*, *51*(3), 310.

Palmese, A., et al. (2019), *GCN Circ. 25360*.

Palmese, A., et al. (2020), Stellar mass as a galaxy cluster mass proxy: application to the dark energy survey redmapper clusters, *Monthly Notices of the Royal Astronomical Society*, *493*(4), 4591–4606, doi:10.1093/mnras/staa526.

Pan, Y. C., et al. (2017), DES15E2mlf: a spectroscopically confirmed superluminous supernova that exploded 3.5 Gyr after the big bang, *MNRAS*, *470*(4), 4241–4250, doi:10.1093/mnras/stx1467.

Pannarale, F., and F. Ohme (2014), PROSPECTS FOR JOINT GRAVITATIONAL-WAVE AND ELECTROMAGNETIC OBSERVATIONS OF NEUTRON-STAR-BLACK-HOLE COALESCING BINARIES, *The Astrophysical Journal*, *791*(1), L7, doi:10.1088/2041-8205/791/1/l7.

Pérez-García, M. A., et al. (2022), Hubble constant and nuclear equation of state from kilonova spectro-photometric light curves, *A&A*, *666*, A67, doi:10.1051/0004-6361/202243749.

Petrov, P., et al. (2022), Data-driven Expectations for Electromagnetic Counterpart Searches Based on LIGO/Virgo Public Alerts, *ApJ*, *924*(2), 54, doi:10.3847/1538-4357/ac366d.

Piran, T. (2004), The physics of gamma-ray bursts, *Reviews of Modern Physics*, *76*(4), 1143–1210, doi:10.1103/RevModPhys.76.1143.

Planck Collaboration, et al. (2014), Planck 2013 results. XVI. Cosmological parameters, *A&A*, *571*, A16, doi:10.1051/0004-6361/201321591.

Planck Collaboration, et al. (2020), Planck 2018 results. VI. Cosmological parameters, *A&A*, *641*, A6, doi:10.1051/0004-6361/201833910.

Pordes, R., D. Petravick, B. Kramer, et al. (2007), The open science grid, *J. Phys.: Conf. Ser.*, *78*, 012,057, doi:10.1088/1742-6596/78/1/012057.

Prochaska, J. X., et al. (2006), The galaxy hosts and large-scale environments of short-hard gamma-ray bursts, *The Astrophysical Journal*, *642*(2), 989–994, doi:10.1086/501160.

Pursiainen, M., et al. (2018), Rapidly evolving transients in the Dark Energy Survey, *MNRAS*, *481*(1), 894–917, doi:10.1093/mnras/sty2309.

Radice, D., S. Bernuzzi, W. D. Pozzo, L. F. Roberts, and C. D. Ott (2017), Probing extreme-density matter with gravitational-wave observations of binary neutron star merger remnants, *The Astrophysical Journal*, *842*(2), L10, doi: 10.3847/2041-8213/aa775f.

Radice, D., A. Perego, K. Hotokezaka, S. A. Fromm, S. Bernuzzi, and L. F. Roberts (2018), Binary neutron star mergers: Mass ejection, electromagnetic counterparts, and nucleosynthesis, *The Astrophysical Journal*, *869*(2), 130, doi: 10.3847/1538-4357/aaf054.

Riess, A. G., S. Casertano, W. Yuan, L. M. Macri, and D. Scolnic (2019), Large Magellanic Cloud Cepheid Standards Provide a 1% Foundation for the Determination of the Hubble Constant and Stronger Evidence for Physics beyond ΛCDM, *ApJ*, *876*(1), 85, doi:10.3847/1538-4357/ab1422.

Riess, A. G., et al. (2009), A Redetermination of the Hubble Constant with the Hubble Space Telescope from a Differential Distance Ladder, *ApJ*, *699*(1), 539–563, doi:10.1088/0004-637X/699/1/539.

Riess, A. G., et al. (2022), A Comprehensive Measurement of the Local Value of the Hubble Constant with 1 km s^{-1} Mpc^{-1} Uncertainty from the Hubble Space Telescope and the SH0ES Team, *ApJ*, *934*(1), L7, doi:10.3847/2041-8213/ac5c5b.

Rodriguez, O., et al. (2019), *GCN Circ. 25423*.

Rosswog, S. (2013), The dynamic ejecta of compact object mergers and eccentric collisions, *Philosophical Transactions of the Royal Society A: Mathematical, Physical and Engineering Sciences*, *371*(1992), 20120,272, doi:10.1098/rsta.2012.0272.

Sagués Carracedo, A., M. Bulla, U. Feindt, and A. Goobar (2021), Detectability of kilonovae in optical surveys: post-mortem examination of the LVC O3 run follow-up, *MNRAS*, *504*(1), 1294–1303, doi:10.1093/mnras/stab872.

Sako, M., et al. (2011), Photometric type ia supernova candidates from the three-year sdss-ii sn survey data, *The Astrophysical Journal*, *738*(2), 162, doi:10.1088/0004-637x/738/2/162.

Schutz, B. F. (1986), Determining the Hubble constant from gravitational wave observations, *Nature*, *323*(6086), 310–311, doi:10.1038/323310a0.

Schutz, B. F. (2011), Networks of gravitational wave detectors and three figures of merit, *Classical and Quantum Gravity*, *28*(12), 125023, doi:10.1088/0264-9381/28/12/125023.

Scolnic, D., et al. (2014), Systematic Uncertainties Associated with the Cosmological Analysis of the First Pan-STARRS1 Type Ia Supernova Sample, *ApJ*, *795*(1), 45, doi:10.1088/0004-637X/795/1/45.

Sebring, T. A., V. L. Krabbendam, and S. R. Heathcote (2003), Southern Astrophysical Research (SOAR) Telescope: steps on the route to success, in *Large Ground-based Telescopes*, vol. 4837, edited by J. M. Oschmann and L. M. Stepp, pp. 71 – 81, International Society for Optics and Photonics, SPIE, doi:10.1117/12.456692.

Setzer, C. N., H. V. Peiris, O. Korobkin, and S. Rosswog (2022), Modelling Populations of Kilonovae, *arXiv e-prints*.

Shandonay, A., et al. (2022), Expediting DECam multimessenger counterpart searches with convolutional neural networks, *The Astrophysical Journal*, *925*(1), 44, doi:10.3847/1538-4357/ac3760.

Shappee, B., et al. (2017), Early spectra of the gravitational wave source gw170817: Evolution of a neutron star merger, *Science*, *358*(6370), 1574–1578.

Singer, L. P., and L. R. Price (2016), Rapid bayesian position reconstruction for gravitational-wave transients, *Phys. Rev. D*, *93*, 024,013, doi:10.1103/PhysRevD.93.024013.

Singer, L. P., et al. (2016a), Going the Distance: Mapping Host Galaxies of LIGO and Virgo Sources in Three Dimensions Using Local Cosmography and Targeted Follow-up, *ApJ*, *829*(1), L15, doi:10.3847/2041-8205/829/1/L15.

Singer, L. P., et al. (2016b), Supplement: "Going the Distance: Mapping Host Galaxies of LIGO and Virgo Sources in Three Dimensions Using Local Cosmography and Targeted Follow-up" (2016, ApJL, 829, L15), *ApJS*, *226*(1), 10, doi:10.3847/0067-0049/226/1/10.

Singer, L. P., et al. (2016c), Going the Distance: Mapping Host Galaxies of LIGO and Virgo Sources in Three Dimensions Using Local Cosmography and Targeted Follow-up, *ApJ*, *829*(1), L15, doi:10.3847/2041-8205/829/1/L15.

Skrutskie, M. F., et al. (2006), The Two Micron All Sky Survey (2MASS), *AJ*, *131*(2), 1163–1183, doi:10.1086/498708.

Soares-Santos, M. (2019), LIGO/Virgo S190510g: DESGW counterpart candidates over 80% of the GW localization area., *GRB Coordinates Network*, *24480*, 1.

Soares-Santos, M., et al. (2017), The electromagnetic counterpart of the binary neutron star merger ligo/virgo gw170817. i. discovery of the optical counterpart using the dark energy camera, *The Astrophysical Journal Letters*, *848*(2), L16.

Soares-Santos, M., et al. (2019a), *GCN Circ. 25336*.

Soares-Santos, M., et al. (2019b), *GCN Circ. 25486*.

Soares-Santos, M., et al. (2019c), *GCN Circ. 25425*.

Soares-Santos, M., et al. (2019d), *GCN Circ. 25438*.

Soares-Santos, M., et al. (2019e), First measurement of the hubble constant from a dark standard siren using the dark energy survey galaxies and the LIGO/virgo binary–black-hole merger GW170814, *The Astrophysical Journal*, *876*(1), L7, doi:10.3847/2041-8213/ab14f1.

Stairs, I. H., S. E. Thorsett, R. J. Dewey, M. Kramer, and C. A. McPhee (2006), The formation of the double pulsar PSR J0737–3039A/B, *Monthly Notices of the Royal Astronomical Society: Letters*, *373*(1), L50–L54, doi:10.1111/j.1745-3933.2006.00241.x.

Stewart, A. R., L.-T. Lo, O. Korobkin, I. Sagert, J. Loiseau, H. Lim, M. A. Kaltenborn, C. M. Mauney, and J. Maxwell Miller (2022), Realistic Kilonova Up Close, *arXiv e-prints*.

Tanaka, M., and K. Hotokezaka (2013), Radiative Transfer Simulations of Neutron Star Merger Ejecta, *ApJ*, *775*(2), 113, doi:10.1088/0004-637X/775/2/113.

The Dark Energy Survey Collaboration (2005), The Dark Energy Survey, *arXiv e-prints*, astro-ph/0510346, doi:10.48550/arXiv.astro-ph/0510346.

The LIGO Scientific Collaboration, the Virgo Collaboration, the KAGRA Collaboration, R. Abbott, T. D. Abbott, and J. Zweizig (2021), GWTC-3: Compact Binary Coalescences Observed by LIGO and Virgo During the Second Part of the Third Observing Run, *arXiv e-prints*.

The PLAsTiCC team, et al. (2018), The Photometric LSST Astronomical Time-series Classification Challenge (PLAsTiCC): Data set, *arXiv e-prints*, arXiv:1810.00001, doi:10.48550/arXiv.1810.00001.

Tucker, D., et al. (2019a), *GCN Circ. 25484*.

Tucker, D., et al. (2019b), *GCN Circ. 25379*.

Tucker, D. L., et al. (2022), SOAR/Goodman Spectroscopic Assessment of Candidate Counterparts of the LIGO/Virgo Event GW190814, *ApJ*, *929*(2), 115, doi:10.3847/1538-4357/ac5b60.

Utsumi, Y., et al. (2017), J-gem observations of an electromagnetic counterpart to the neutron star merger gw170817, *Publications of the Astronomical Society of Japan*, *69*(6), 101.

Valenti, S., et al. (2017), The discovery of the electromagnetic counterpart of gw170817: kilonova at 2017gfo/dlt17ck, *The Astrophysical Journal Letters*, *848*(2), L24.

Veitch, J., et al. (2015), Parameter estimation for compact binaries with ground-based gravitational-wave observations using the lalinference software library, *Phys. Rev. D*, *91*, 042,003, doi:10.1103/PhysRevD.91.042003.

Vieira, N., et al. (2020).

Villar, V. A., et al. (2017), The Combined Ultraviolet, Optical, and Near-infrared Light Curves of the Kilonova Associated with the Binary Neutron Star Merger GW170817: Unified Data Set, Analytic Models, and Physical Implications, *ApJ*, *851*(1), L21, doi:10.3847/2041-8213/aa9c84.

Watson, A. M., et al. (2020), Limits on the electromagnetic counterpart to S190814bv, *Monthly Notices of the Royal Astronomical Society*, *492*(4), 5916–5921, doi:10.1093/mnras/staa161.

Wiesner, M., et al. (2019a), *GCN Circ. 25540.*

Wiesner, M., et al. (2019b), *GCN Circ. 25596.*

Wollaeger, R. T., C. L. Fryer, E. A. Chase, C. J. Fontes, M. Ristic, A. L. Hungerford, O. Korobkin, R. O'Shaughnessy, and A. M. Herring (2021), A Broad Grid of 2D Kilonova Emission Models, *ApJ*, *918*(1), 10, doi:10.3847/1538-4357/ac0d03.

Woosley, S. E., and T. A. Weaver (1986), The physics of supernova explosions, *Annual Review of Astronomy and Astrophysics*, *24*(1), 205–253, doi:10.1146/annurev.aa.24.090186.001225.

Zhu, J.-P., S. Wu, Y.-P. Yang, B. Zhang, Y.-W. Yu, H. Gao, Z. Cao, and L.-D. Liu (2021), No Detectable Kilonova Counterpart is Expected for O3 Neutron Star-Black Hole Candidates, *ApJ*, *921*(2), 156, doi:10.3847/1538-4357/ac19a7.

Zhu, J.-P., et al. (2023), Kilonovae and Optical Afterglows from Binary Neutron Star Mergers. II. Optimal Search Strategy for Serendipitous Observations and Target-of-opportunity Observations of Gravitational Wave Triggers, *ApJ*, *942*(2), 88, doi:10.3847/1538-4357/aca527.